



HAL
open science

Conducting ceramics based on ZnO co-doped by (Al, Ti, Mg) : microstructure, electronic active defects and electrical properties

Qianying Sun

► **To cite this version:**

Qianying Sun. Conducting ceramics based on ZnO co-doped by (Al, Ti, Mg) : microstructure, electronic active defects and electrical properties. Materials. Le Mans Université; Institute of ceramics (Shanghai, Chine), 2020. English. NNT : 2020LEMA1014 . tel-02930311

HAL Id: tel-02930311

<https://theses.hal.science/tel-02930311>

Submitted on 4 Sep 2020

HAL is a multi-disciplinary open access archive for the deposit and dissemination of scientific research documents, whether they are published or not. The documents may come from teaching and research institutions in France or abroad, or from public or private research centers.

L'archive ouverte pluridisciplinaire **HAL**, est destinée au dépôt et à la diffusion de documents scientifiques de niveau recherche, publiés ou non, émanant des établissements d'enseignement et de recherche français ou étrangers, des laboratoires publics ou privés.

THÈSE DE DOCTORAT EN COTUTELLE

LE MANS UNIVERSITÉ

COMUE UNIVERSITÉ BRETAGNE LOIRE

ÉCOLE DOCTORALE N° 596

Matière, Molécules, Matériaux

Spécialité : « *Physique* »

Qianying SUN

« **Conducting ceramics based on ZnO co-doped by (Al, Ti, Mg):
Microstructure, electronic active defects and electrical properties** »

Thèse présentée et soutenue à : Institut de Céramiques de Shanghai, Académie des Sciences de Chine

Et en Visio Conférence : Institut des Molécules et Matériaux du Mans , Le Mans Université

Date : **27 May 2020**

Thèse N° : 2020LEMA1014

Rapporteurs avant soutenance :

Malgorzata MAKOWSKA-JANUSIK, Professeure, Institut de Physique, Université Jan Dlugosz à Czesochowa, Pologne

Ning DAI, Professeur, Institut de physique technique de Shanghai, Académie chinoise des sciences, Chine

Zhitang SONG, Professeur, Institut des microsystèmes Shanghai, Académie chinoise des sciences, Chine

Composition du Jury :

Président : **Ning DAI**, Professeur, Institut de physique technique de Shanghai, Académie des sciences, Chine

Examineurs : **Malgorzata MAKOWSKA-JANUSIK**, Professeure, Université Jan Dlugosz à Czesochowa, Pologne

Zhitang SONG, Professeur, Institut des microsystèmes de Shanghai, Académie des sciences, Chine

Liaoying ZHENG, Professeur, Institut de céramique de Shanghai, Académie des sciences, Chine

Co-encadrante : **Maud BARRE**, MCF, Institut des Molécules et Matériaux du Mans, Le Mans Université, France

Co-Dir. de thèse : **Guorong LI**, Professeur, Institut de céramique de Shanghai, Académie des sciences, Chine

Dir. de thèse : **Abdel Hadi KASSIBA**, Professeur, Institut des Molécules et Matériaux du Mans, Le Mans Université, France

Titre : Céramiques conducteurs à base de ZnO co-dopés (Al,Ti, Mg) : Structure, défauts électroniques actifs et propriétés électriques

Mots clés : Céramiques ZnO, Co-Dopage, Défauts électroniques, Conductivité électrique, Résonance magnétique

Les céramiques conductrices à base de ZnO suscitent un important intérêt pour leurs applications comme varistances, capteurs de gaz, électrodes transparentes, dispositifs piézoélectriques, électro-optiques ou thermoélectriques. Le dopage de ZnO confère aux céramiques formées des propriétés électriques et optiques remarquables caractérisées par une transparence optique modulée, des énergies de liaison élevées pour les excitons, et des conductivités électriques atteignant $0.1 \text{ MS}\cdot\text{m}^{-1}$. La grande conductivité de ZnO est intimement liée aux éléments dopants, à la microstructure des céramiques et aux conditions de synthèse et traitements. Les joints de grains, la structure cristalline, le désordre structural et les défauts électroniques contribuent au comportement électrique des matériaux. Le présent travail de thèse

s'inscrit dans ce contexte et porte sur la mise en œuvre de méthodes de fabrication de céramiques à base de ZnO co-dopées par des éléments (Al, Ti, Mg) et l'étude de leurs caractéristiques physiques incluant la structure cristalline, la microstructure et le comportement électrique. Ainsi, des études exhaustives ont été menées par des méthodes structurales (RX, Raman), microscopies (MET, MEB) et de résonance magnétique (RPE, RMN) sensible à l'ordre local et aux défauts électroniques actifs. La conductivité est ajustée par la nature des éléments dopants, l'atmosphère de frittage et les méthodes de fabrication par solutions solides ou par frittage flash (SPS). La corrélation "Préparation - Structure - Conductivité" a été établie pour la réalisation de céramiques à base de ZnO avec de fortes conductivités ouvrant la voie à des applications technologiques potentielles.

Title : Conducting ceramics based on ZnO co-doped by (Al, Ti, Mg): Microstructure, electronic active defects and electrical properties

Keywords : ZnO ceramics, Co-doping, Electronic defects, Electrical conductivity, Magnetic resonance

ZnO based ceramics with appropriate doping elements show excellent electrical and optical properties such as high exciton binding energies, a modulated optical transparency and high electrical conductivities. Therefore, ZnO based conducting ceramics have been extensively investigated in the aim of their application as resistors, visitors, gas sensors, transparent electrodes, solar cell windows, piezoelectric, electro-optical and thermoelectric devices. The high conductivity of ZnO ceramics up to $0.1 \text{ MS}\cdot\text{m}^{-1}$ is closely related to the doping elements along with the ceramic microstructure and the processing conditions with particular effects of grain boundaries, crystalline structure and structural disorder within the ceramics. Thus, the present thesis is devoted to the fabrication by sintering under

defined conditions (sintering atmospheres, preparation processes) of ZnO based ceramics co-doped by (Al, Ti, Mg), the investigations and deep analysis of their related properties including crystalline structure, micro-structure and the electrical behaviors. Exhaustive studies were developed on the doped ZnO ceramics by using structural methods (XRD, Raman), microscopy (TEM, SEM) and magnetic resonance (EPR, NMR) probing the local order and electronic active defects. The conductivity is adjusted by the nature of the structure influenced by the doping elements, the sintering atmospheres, and the sintering methods. The correlation about "Preparation - Structure - Conductivity" has been established to pave the way for the potential technological applications of highly conducting ZnO-based ceramics.

Acknowledgement

Time flies, and the doctoral career that is about to end has left me with a lot of valuable wealth, and I am full of hope and motivation to greet the next life. On the completion of this thesis full of scientific research results during the doctorate period, reviewing the good times of these years, at this moment, I would like to thank all the teachers, classmates, friends and families who have given me guidance, training, care, encouragement and help!

First and foremost, I am very grateful to my supervisors - Professor Li Guorong and Professor Abdel Hadi Kassiba. Professor Li's rigorous and pragmatic work attitude, tireless teaching method, gentle and jade-like personality, constantly inspires me to work hard and live seriously; Professor Kassiba has an optimistic and cheerful, humorous and calm life attitude, and a patient and meticulous, conscientious and responsible working methods, which encourages me a lot during my life. It's my great honor to be their student. With the help of these two highly respected, knowledgeable and dedicated professors, my doctoral career can be perfectly ended, and I have gained the academic knowledge and way of doing things that will be useful for my lifetime.

I am deeply grateful to my Co-supervisor - Maud Barre for the kind help on ceramic preparation, sample testing and thesis modification. Her friendly care and warm communication were also strong support and companion for me when I studied in Le Mans University.

I am particularly grateful for the patient guidance and assistance given by Zheng Liaoying, Zeng Jiangtao, Zeng Huarong, Man Zhenyong, Zhao Kunyu, Tian Tian, Ruan Xuezheng, etc. from the Functional Ceramic Materials and Devices Research Group of SICCAS. And I sincerely thank to the meticulous and enthusiastic guidance in experimental operation and result analysis provided by Jens Dittmer, Alain Bulou, Anthony Rousseau, Francois Goutenoire, Nourdin Yaakoubi and other scholars from Le Mans University in France.

Thanks to Professor Malgorzata Makowska-Janusik, Karolina Ordon, Bartłomiej Kowalik of Jan Dlugosz University in Czestochowa for their academic guidance and life assistance

during my studies in Poland.

Thanks to Zhou Zhiwei, Lu Caifei, Zhao Xueying, Lu Xinhong and Zhang Peishuai from the Graduate Department of SICCAS for their care and help in studying and living. Thanks to Geoffroy Martin, Annie Rutter, Fanny Laude-molina and other Le Mans University staff for their help in course study and life trivia.

Sincere thanks also go to my colleagues and friends: Peng Jianguili, Shang Jing, Huang Xiang, Luo Xiao, Zou Jian, Wang Tiantian, Su Rigü, Saïda Ménard, Michèle Houdusse, Manel Missaoui, Zhu Yueying, Long Yuzhu, Annette Parker and others for their spiritual companionship, constant support, warm assistance, and productive discussions. The time spent with each other is short, but I am always grateful and cherished.

I gratefully acknowledge the financial support that enabled me to finish smoothly my Ph.D. study. I was funded by the French Excellence grant program **EIFFEL** and the Polish National Agency program named **PROM**. My work was also partially supported by the Functional Ceramic Materials and Device Physics Research Group of SICCAS, and the Ecole Doctorale 3M at Le Mans University, and the Institut des molécules et matériaux du Mans (IMMM).

Last but not the least, I would like to take this opportunity to express my deepest appreciation to my precious families: thankful to my parents for the continuous support and love over the years, thankful to my sister Sun Liying for the understanding and companionship, thankful to my husband Jiang Yiguang for the faithful love, constant encouragement and unconditional care.

List of publications

[1] Qianying Sun, Tian Tian, Laoying Zheng, Zhenyong Man, Guorong Li, Maud Barré, Jens Dittmer, Alain Bulou, Abdel Hadi Kassiba. Electronic active defects and local order in doped ZnO ceramics inferred from EPR and ^{27}Al NMR investigations. **Journal of the European Ceramic Society**, 2019, 39: 3070-3076.

[2] Qianying Sun, Guorong Li, Tian Tian, Zhenyong Man, Liaoying Zheng, Maud Barré, Jens Dittmer, François Goutenoire, Abdel Hadi Kassiba. Controllable microstructure tailoring for regulating conductivity in Al doped ZnO ceramics. **Journal of the European Ceramic Society**, 2020, 40: 349-354.

[3] Qianying Sun, Guorong Li, Tian Tian, Jiangtao Zeng, Kunyu Zhao, Liaoying Zheng, Maud Barré, Jens Dittmer, François Goutenoire, Anthony Rousseau, Abdel Hadi Kassiba. Co-doping effects of (Al, Ti, Mg) on the microstructure and electrical behavior of ZnO based ceramics. **Journal of the American Ceramic Society**, 2020, 103:3194-3204.

[4] Qianying Sun, Guorong Li, Zhenyong Man, Liaoying Zheng, Maud Barré, Jens Dittmer, Sandy Auguste, Anthony Rousseau, Abdel Hadi Kassiba. Microstructure on the local order and electronic defects in (Al, Ti, Mg) oxide co-doped ZnO conductive ceramics. **Journal of the European Ceramic Society** (Minor Revision)

[5] Haoxian Chen, Qianying Sun, Jiangtao Zeng, Liaoying Zheng, Guorong Li, Abdel Hadi Kassib. The exploration of the microstructure of Al-doped ZnO ceramics with high electrical conductivity obtained via spark plasma sintering. **Journal of the European Ceramic Society** (Major Revision)

Participation in the conferences

Oral communications:

Investigation of electrical behavior and microstructure in doped-ZnO ceramics. 2019 International Symposium of Research and Application of Functional Oxide Electronic Ceramics, Shanghai, China. 2019. 6. 11-13

Posters:

The preparation and performance of TiO₂, Al₂O₃ and MgO doped-ZnO conductive ceramics. Le Mans university JED conference, Le Mans, France. 2018.6.6

Abstract

ZnO based ceramics with appropriate doping elements show excellent electrical and optical properties such as high exciton binding energies, a modulated optical transparency and electrical conductivities. Therefore, ZnO based conducting ceramics have been extensively investigated in the aim of their application in the fields of resistor, varistors, gas sensors, conductive film target, transparent electrodes, solar cells, liquid crystal displays, piezoelectric, electro-optical and thermoelectric devices. The high conductivity of ZnO ceramics is closely related to the doping elements along with the ceramic microstructure and the processing conditions. Thus, grain boundaries, crystalline structure, and structural disorder within a polycrystalline ZnO ceramic depend critically on the doping elements, sintering method, and sintering atmosphere during the preparation process. The involved conductivity in doped ZnO ceramics is highly dependent on the above mentioned parameters. Thus, the present thesis is devoted to the investigations and the analysis of related properties of ZnO-based ceramics co-doped by Al₂O₃, TiO₂, and MgO. The conductivity is adjusted by the nature of the structure influenced by the doping elements, the sintering atmosphere, and the sintering method. The correlation "Preparation - Structure - Conductivity" has been established to pave the way for highly conducting ZnO-based ceramics. The main developed research tasks, their results and achievements are hereafter outlined:

1. The reducing nature of the sintering atmosphere is an important parameter affecting the structure and performance of doped ZnO ceramics. The conductivity increases up to $\sigma = 1.5 \times 10^5 \text{ S} \cdot \text{m}^{-1}$ by sintering under CO + N₂ atmosphere and the positive temperature coefficient is reaching 749 ppm/°C. The improvement by the reducing atmosphere is caused by the low oxygen partial pressure which increase the solubility of Al and Ti in ZnO, thereby increasing donor defects and then the charge carrier concentration. Meanwhile, the process reduces the acceptor defects at the grain boundaries enhancing the carrier mobility. In addition, the Al_{Zn}-Zn_i complex has been identified as the main shallow donor defect that enhances the conductivity of ZnO ceramics. A consistent analysis has been carried out based on

experimental investigations by Raman, EPR, and NMR techniques.

2. As Al doping improves highly the electrical conductivity of ZnO-based ceramics, the role of Al₂O₃ doping ratios has been investigated within the range of 0.1-0.55 mol.% and for a processing technique with CO + N₂ as reducing atmosphere. Structural and electronic active defects analysis by XRD, SEM, Raman, EPR and NMR methods, shows that the Al₂O₃ content modulates the shallow donor Al_{Zn}-Zn_i complexes, grain boundaries and the fraction of the secondary ZnAl₂O₄ spinel phase in ZnO ceramics and thereby altering the electrical conductivity.
3. The effect of the spark plasma sintering (SPS) method on the structure and electrical properties of ZnO ceramics doped with 0.25 mol% Al₂O₃ has been studied. This method improves the solubility of Al in ZnO, reduces the spinel phase content, and limits the grain size growth. The comprehensive analysis of Raman spectra, UV-visible absorption spectra and photoluminescence spectra show the role of the SPS method to increase the structural disorder and the concentration of shallow donor Al_{Zn}-Zn_i complexes enhancing the electrical conductivity of ZnO ceramics.
4. Although the combined process of co-doping ZnO ceramics leads to high conductivities, the role of each doping element such as Al, Ti and Mg must be clarified on how it may affect the key features of the host ceramics. Different doping combinations with different contents of Al, Ti and Mg ions have been realized and altered differently the phase composition, microstructure and defects in ZnO-based ceramics, and then affect the conductivity. The similar characteristics (valence, size) of Mg ions and Zn ions essentially contribute to the formation of defects. Doping by Ti ions, leads to deep donors (Ti³⁺) and induces a secondary insulating spinel phase which limits the conductivity. As for doping with Al ions, it has a significant effect on the conductivity owing to the shallow Al_{Zn}-Zn_i donor defects, which contribute to a high concentration of charge carriers.
5. Studies have been devoted to the role of microstructure and grain morphology on the conductive properties of ZnO-doped ceramics. Thus, the electrical behavior was compared between particles with large dimensions (20 μm) as in massive ceramics and particles of smaller sizes (<100 μm). The correlation between the

microstructure and the electrical properties of doped ceramics was established by analyzing the coordination of doping ions Al in ZnO, the nature of electronic defects and the local disorder of ZnO materials.

Keywords: ZnO ceramics, Co-doping, Electronic defects, Electrical conductivity, Magnetic resonance

摘 要

ZnO 导电陶瓷的原料丰度高、成本低廉、无毒无害、制备工艺简单，并且具有大的禁带宽度、高的激子束缚能、高的透明度和强的导电能力等优异的电学、光学性质，因此在传导电阻、导电薄膜靶材、电极材料、热电器件等领域具有广泛的研究价值和应用前景。ZnO 陶瓷的高导电能力与其结构密切相关。作为多晶结构的陶瓷材料，烧结获得的 ZnO 陶瓷内部的施主浓度、晶界结构、物相种类、结构无序程度等结构特征受到制备过程中的掺杂元素种类及含量、烧结方式、烧结气氛等参数的调控，并且这些结构特征共同协调影响着 ZnO 陶瓷的导电能力。因此，本论文主要研究了 Al₂O₃、TiO₂ 和 MgO 掺杂的 ZnO 基陶瓷，通过改变掺杂剂的种类及含量、烧结气氛、烧结方式来调节电导率的变化，并从 ZnO 基陶瓷的物相结构、显微形貌、局部结构无序度、缺陷类型及分布的角度，分析调控 ZnO 陶瓷的结构及电导率的因素，从而建立起“制备-结构-性能”间的联系，指导 ZnO 基导电陶瓷的研发以及应用。

本论文中涉及到的主要创新工作及结果概述如下：

1. 烧结气氛是影响 ZnO 陶瓷的结构和性能的一个重要参数，分别在空气、氮气(N₂)、一氧化碳和氮气混合气体(CO+N₂)的气氛中烧结制备了 Al₂O₃、TiO₂ 和 MgO 共掺杂的 ZnO 基导电陶瓷，电导率按此顺序递增，且在 CO+N₂ 还原气氛中制备的 ZnO 陶瓷具有最高的电导率 $\sigma=1.5\times 10^5\text{ S}\cdot\text{m}^{-1}$ 以及正的阻温系数 749 ppm/°C。低氧分压的还原气氛能够提高 Al、Ti 在 ZnO 中的固溶度，进而提升施主缺陷含量，增加载流子的浓度；同时具有降低晶界受主缺陷、增加载流子迁移率的作用。此外，拉曼光谱、EPR 和 NMR 的综合分析共同确定了 Al_{Zn}-Zn_i 复合体缺陷为增强 ZnO 基陶瓷的导电能力的主要浅施主缺陷，且该缺陷的含量在还原气氛下烧结制备的陶瓷中达到最大，解释了高导电的原因。
2. 掺杂 Al 元素具有显著提高 ZnO 基陶瓷电导率的作用，因此需要分析 Al 元素对 ZnO 陶瓷微观结构和导电能力的作用。在 CO+N₂ 还原气氛下烧结制备了 Al₂O₃ 的掺杂量分别为 0.1 mol%、0.25 mol%、0.4 mol% 和 0.55 mol% 的 ZnO 基导电陶瓷，探究了不同掺杂含量的 Al₂O₃ 对 ZnO 陶瓷的结构和电学性能的

影响。不同含量的 Al_2O_3 能够调节 ZnO 陶瓷内的浅施主 $\text{Al}_{\text{Zn}}\text{-Zn}_i$ 复合体缺陷的浓度、晶界的数量和 ZnAl_2O_4 尖晶石的含量, 通过调控 ZnO 陶瓷的结构实现电导率的变化, 且在 Al_2O_3 的最佳掺杂量 0.25 mol% 时实现了陶瓷内最佳的载流子的浓度和迁移率, 进而获得到了最高的电导率 $1.52 \times 10^5 \text{ S} \cdot \text{m}^{-1}$ 。

3. 研究了放电等离子体烧结 (SPS) 方式对掺杂 0.25 mol% Al_2O_3 的 ZnO 陶瓷的结构和电性能的作用, SPS 方式能够增加 Al 在 ZnO 中的固溶度、减少尖晶石的含量, 同时具有降低晶粒尺寸、增加晶界数量的作用。通过拉曼光谱、紫外可见吸收光谱、光致发光光谱的综合分析表明 SPS 方式能够增加结构无序度和浅施主 $\text{Al}_{\text{Zn}}\text{-Zn}_i$ 复合体含量, 从而提高了 ZnO 陶瓷的电导率。
4. 通过改变 Al、Ti 和 Mg 离子的掺杂含量制备了具有不同组分的 ZnO 基陶瓷, 用于探究 Al、Ti 和 Mg 掺杂元素对 ZnO 陶瓷的作用。不同的掺杂组合会很大程度地改变 ZnO 基陶瓷中的物相组成、显微结构和缺陷种类, 进而影响着电导率的高低。Mg 离子与 Zn 离子的相似性, 使得掺杂后 ZnO 陶瓷的结构和电性能无明显变化; 掺杂 Ti 离子后产生深施主 Ti^{3+} 及过量的尖晶石, 导致 ZnO 陶瓷的导电能力有所降低; 基于浅施主 $\text{Al}_{\text{Zn}}\text{-Zn}_i$ 复合体缺陷能够增加传导电子的数量, 掺杂 Al 离子的 ZnO 基陶瓷的导电性能大幅度提高。
5. 上述研究表明了掺杂 Al 的 ZnO 陶瓷中形成的浅施主 $\text{Al}_{\text{Zn}}\text{-Zn}_i$ 复合体缺陷是提高电导率的最主要因素。将 ZnO 导电陶瓷片加工成具有不同导电能力和不同颗粒尺寸的 ZnO 粉体, 研究了与 $\text{Al}_{\text{Zn}}\text{-Zn}_i$ 复合体有关的奈特位移效应以及电荷离域程度和导电能力的关系。结果表明具有高导电能力的大尺寸 ZnO 陶瓷颗粒构成的粉体中 $\text{Al}_{\text{Zn}}\text{-Zn}_i$ 复合体的浓度更高, 离域电荷分布范围更广, 从而间接地说明了 ZnO 陶瓷具有高电导率的原因。通过对 Al 元素的配位环境和电子缺陷结构及 ZnO 材料的局部无序度的分析, 建立了 Al 掺杂 ZnO 的微观结构与电性能之间的相关性。

关键词: ZnO 陶瓷, 施主掺杂, 电导率, $\text{Al}_{\text{Zn}}\text{-Zn}_i$ 复合体, 磁共振技术

Résumé

Les céramiques conductrices à base de ZnO suscitent un important intérêt pour leurs applications comme varistances, capteurs de gaz, électrodes transparentes, dispositifs piézoélectriques, électro-optiques ou thermoélectriques. Le dopage de ZnO par des éléments (Al, Ti, Mg) confèrent aux céramiques formées des propriétés électriques et optiques remarquables caractérisées par une transparence optique modulée, des énergies de liaison élevées pour les excitons, et des conductivités électriques atteignant $10^5 \text{ S}\cdot\text{cm}^{-1}$. Le présent travail de thèse est consacré à l'étude et à l'analyse des effets de dopage et des conditions de fabrication des céramiques à base de ZnO. La conductivité est ajustée par la nature des éléments dopants, l'atmosphère de frittage et les méthodes de fabrication par solutions solides ou par frittage flash (SPS). La corrélation "Préparation - Structure - Conductivité" a été établie pour ouvrir la voie à la réalisation de céramiques à base de ZnO avec de fortes conductivités. Les principales contributions et les résultats marquants sont décrits ci-dessous:

1. L'atmosphère de frittage est un paramètre important affectant la structure et les performances des céramiques ZnO. Différentes compositions de ZnO co-dopées par (Al, Ti, Mg) ont été préparées par frittage sous air, azote (N_2) ou un mélange $\text{CO} + \text{N}_2$. La conductivité augmente avec la nature réductrice de l'atmosphère utilisée. En particulier, les céramiques ZnO préparées dans un $\text{CO} + \text{N}_2$ ont la conductivité la plus élevée $\sigma = 1,5 \times 10^5 \text{ S}\cdot\text{m}^{-1}$ et un coefficient de température positif (PTC) de 749 ppm/°C. L'atmosphère réductrice augmente la solubilité de Al et Ti dans ZnO, favorisant ainsi les défauts donneurs et améliorant la concentration des porteurs. En parallèle, il peut réduire les défauts d'accepteur aux joints de grains et contribuer à augmenter la mobilité des porteurs. En outre, des défauts électroniques sous la forme d'associations $\text{Al}_{\text{Zn}}\text{-Zn}_i$ ont été identifiés par Raman, RMN et RPE, comme les principaux défauts donneurs qui améliorent la conductivité des céramiques ZnO co-dopées et frittées sous une atmosphère réductrice.

2. Le dopage par Al_2O_3 améliore considérablement la conductivité électrique des céramiques à base de ZnO . Il est donc judicieux d'analyser l'effet de la teneur en éléments dopants (Al) sur la microstructure et la conductivité électrique. Ainsi, des céramiques conductrices à base de ZnO dopées avec 0,1, 0,25, 0,4 et 0,55 mol.%, de Al_2O_3 ont été préparées dans une atmosphère réductrice de ($\text{CO} + \text{N}_2$). Le taux de dopage optimal en Al contribue à la formation des défauts donneurs peu profonds de type $\text{Al}_{\text{Zn}}\text{-Zn}_i$ qui induisent une conductivité de l'ordre de $1.25 \times 10^5 \text{ S} \cdot \text{m}^{-1}$. Par contre, pour des taux élevés de dopage, la formation de joints de grains et la phase secondaire spinelle ZnAl_2O_4 contribuent à dégrader la conductivité électrique des céramiques dopées.
3. L'effet de la méthode de frittage flash (SPS) sur la structure et les propriétés électriques des céramiques ZnO dopées avec 0,25% molaire de l'oxyde Al_2O_3 a été étudié. La méthode SPS contribue à augmenter la solubilité d'Al dans ZnO , réduit la teneur en phase spinelle, et limite la croissance des grains, augmentant de fait le nombre de joints de grains. L'analyse complète des spectres Raman, d'absorption UV-visible et des spectres de photoluminescence montre que la méthode SPS favorise le désordre structural et la formation des complexes donneurs peu profonds $\text{Al}_{\text{Zn}}\text{-Zn}_i$, améliorant ainsi la conductivité électrique des céramiques ZnO .
4. Une étude systématique des effets des éléments dopants sur les propriétés des matrices hôtes a été menée sur différentes compositions de céramiques avec différentes teneurs en ions Al, Ti et Mg. Les caractéristiques similaires (valence, taille) des ions Mg et des ions Zn contribue essentiellement à la formation de défauts. Pour le dopage avec des ions Ti, des donneurs profonds (Ti^{3+}) sont formés ainsi qu'une phase secondaire isolante de type spinelle qui limite la conductivité. Quant au dopage aux ions Al, il présente un effet conséquent sur l'ampleur de la conductivité grâce aux défauts donneurs peu profonds $\text{Al}_{\text{Zn}}\text{-Zn}_i$, qui contribuent à une forte concentration de porteurs de charges.

5. Des études ont été consacrées au rôle de la microstructure et la morphologie des grains sur les propriétés de conduction des céramiques dopées ZnO. Ainsi, le comportement électrique a été comparé entre des particules à grandes dimensions (20 μm) comme dans les céramiques massives et des particules de plus petites tailles (<100 μm). La corrélation entre la microstructure et les propriétés électriques des céramiques dopées a été établie en analysant la coordination des ions dopants Al dans ZnO, la nature des défauts électroniques et le désordre local des matériaux ZnO.

Mots clés: Céramiques ZnO, Co-Dopage, Défauts électroniques, Conductivité électrique, Résonance magnétique

Contents

Acknowledgement.....	I
List of publications.....	III
Participation in the conferences.....	IV
Abstract.....	V
摘 要.....	VIII
Contents.....	XIII
General Introduction.....	1
Chapter 1 Introduction.....	4
1.1 Structure of ZnO conductive ceramics.....	4
1.1.1 Crystal structure and basic properties of ZnO.....	4
1.1.2 Structure of ZnO conductive ceramic.....	6
1.2. Electrical properties of ZnO conductive ceramics.....	11
1.2.1 Electrical Conductivity.....	11
1.2.2 Temperature coefficient of resistance (TCR).....	13
1.2.3 Nonlinear coefficient.....	14
1.2.4 Energy Density.....	16
1.2 Defect features and doping effects in ZnO.....	16
1.2.1 Intrinsic defects.....	17
1.2.2 Extrinsic defects.....	18

1.2.3 Experimental methods for defect studies.....	20
1.3 Applications, recent advances and trends in ZnO based materials	22
1.3.1 Application of ZnO-based semiconductor.....	22
1.3.2 Advantages of ZnO conductive ceramics.....	24
1.3.3 Contributions to improve the electrical conductivity.....	25
Chapter 2 Experimental procedures and Instrumentation.....	42
2.1 Processing of doped ZnO based materials.....	42
2.1.1 Experimental flow.....	42
2.1.2 Preparation process.....	43
2.2 Characterization techniques.....	45
2.2.1 Electrical measurements (Four-point method).....	45
2.2.2 Physical Property Measurement System (PPMS).....	47
2.2.3 Electron Microscopy (SEM and TEM).....	49
2.2.4 X-ray Diffraction.....	53
2.2.5 Raman Spectroscopy.....	54
2.2.6 Electron Paramagnetic Resonance.....	57
2.2.7 Nuclear Magnetic Resonance.....	59
Chapter 3 Role of the reducing sintering atmosphere on the electrical properties and microstructure of (Al, Ti, Mg) oxide co-doped ZnO ceramics.....	62
3.1 Introduction.....	62
3.2 Sample preparation and characterization.....	65

3.3 Structural and morphology studies.....	65
3.4 Conduction features in ZnO ceramics.....	69
3.5 Vibrational signatures of doped ZnO based ceramics.....	70
3.6 Electronic active defects probed by EPR.....	73
3.7 Local order probing of Al doping ions.....	76
3.8 Conclusion.....	79
3.9 References.....	80
Chapter 4 Effects of Al doping concentration and sintering methods on ZnO based ceramics.....	86
4.1 Introduction.....	86
4.2 Sample preparation and characterization.....	88
4.3 Conduction features in ZnO ceramics.....	89
4.4 Structural and morphology studies.....	91
4.4.1 Phase structure analysis.....	91
4.4.2 Morphology studies.....	93
4.5 Vibrational signatures of doped ZnO based ceramics.....	95
4.6 Local order probing of Al doping ions.....	97
4.7 Spark Plasma Sintering of Al doped ZnO.....	100
4.7.1 Structural and morphology studies.....	100
4.7.2 Conduction features.....	101
4.7.3 Raman spectra studies.....	102

4.7.4 UV-Vis Absorption spectra and Photoluminescence studies.....	103
4.8 Conclusion.....	107
4.9 Reference.....	108
Chapter 5 Effects of selective doping or co-doping on (Al, Ti, Mg) oxide on ZnO based ceramics.....	113
5.1 Introduction.....	113
5.2 Sample preparation and characterization.....	114
5.3 Structural studies.....	115
5.4 Morphology studies.....	118
5.5 Conduction features in ZnO ceramics.....	120
5.6 Vibrational signatures of doped ZnO based ceramics.....	121
5.7 Electronic active defects probed by EPR.....	124
5.8 Local order probing of Al and Zn ions.....	127
5.9 Conclusion.....	129
5.10 Reference.....	130
Chapter 6 Investigation of the local order and Al_{Zn}-Zn_i defect complexes on the high conductivity in (Al, Ti, Mg) oxide co-doped ZnO ceramics.....	134
6.1 Introduction.....	134
6.2 Sample preparation and characterization.....	136
6.3 Morphology and size analysis of particles.....	136

6.4 Structural studies.....	139
6.5 Electronic active defects probed by EPR.....	140
6.6 Local environment probing of Al ions.....	142
6.7 Conclusion.....	144
6.8 Reference.....	145
Chapter 7 General Conclusions and Perspectives.....	148
7.1 General Conclusions.....	148
7.2 Perspectives.....	152
List of Figures.....	154
List of Tables.....	159

General Introduction

1. Research Significance

As a resistance component, ZnO-based conductive ceramics have the advantages of easy conductivity adjustment, small and positive temperature coefficient of resistance, high linearity of volt-ampere characteristics, high energy density, strong reliability, and stable performance. Therefore, it has great application prospects in the fields of power equipments and electronic systems. Pure ZnO-based ceramic has very poor electrical conductivity, which is much smaller than metal and carbon resistors, far from the meeting requirements for conductive devices in transmission circuits. Thus, it is important to improve the conductivity of ZnO-based ceramics. In addition, ZnO ceramics with high electrical conductivity can also be used in conductive thin film targets, electrode materials, thermoelectric devices, etc. Therefore, the research theme of this thesis is the preparation and analysis of highly conductive ZnO ceramics.

Due to a few donor defects, pure ZnO is an intrinsic N-type semiconductor, thus donor doping is the most effective way to improve the conductivity of ZnO ceramics. Al in IIIA group is the most common and efficient donor dopant. It is necessary to explore the effect of Al content on the microstructure and defect types of ZnO-based ceramics, and then analyze the mechanism of its roles on electrical conductivity. Except donor doping, reducing atmosphere sintering and spark plasma sintering can improve the conductivity of ZnO ceramics. It can be speculated that the preparation of Al-doped ZnO conductive ceramics by these two methods may achieve further improved electrical conductivity. Therefore, it is significant to study the effects of reducing atmosphere sintering and spark plasma sintering on Al-doped ZnO conductive ceramics, so as to obtain ZnO ceramics with high conductivity. In addition, in order to obtain a ZnO-based conductive ceramic with excellent comprehensive properties such as compact structure, good temperature resistance, and stable

voltammetric characteristics, dopants such as Ti and Mg other than Al need to be added. Exploring the effect of reducing sintering atmosphere on the structure, defects and conductivity of these three elements doped ZnO ceramics can explain the effects of sintering atmosphere on multi-doped ZnO ceramics. This is more conducive to the research and application of multi-elements co-doped ZnO-based ceramics.

2. Research content

The purposes of this thesis are to prepare ZnO-based ceramics with high conductivity and to analyze the mechanism of enhancing the conductivity. The effects of sintering atmosphere, Al₂O₃ doping ratio, SPS sintering method, and dopants Al₂O₃, TiO₂ and MgO on the crystalline phases, microstructure, local disorder, and defects of ZnO-based ceramics have been mainly studied to analyze their roles on electrical properties such as temperature coefficient of resistance, linearity, energy density, especially the electrical conductivity. The mechanism of regulating conductivity has been illustrated in detail. In addition, through the research of particles with different sizes processed from ZnO-based ceramics, the reason why the defect Al_{Zn}-Zn_i complex can significantly improve the conductivity of ZnO ceramics has been explained.

1. The ZnO-based conductive ceramics have been prepared using the sintering atmosphere of air, N₂, CO+N₂, and the ceramics sintered under the CO+N₂ reducing atmosphere have greatly improved electrical conductivity ($1.52 \times 10^5 \text{ S} \cdot \text{m}^{-1}$).
2. Under the CO+N₂ reducing sintering atmosphere, ZnO ceramics doped with different Al₂O₃ ratio have been synthesized, and the adjustment effect of the dopant Al₂O₃ on the phase composition, grain boundaries, and donor defects of ZnO ceramics are comprehensively studied to analyze the conductivity mechanism.

3. In addition, the spark plasma sintering also has the effect of improving the electrical conductivity of Al_2O_3 doped ZnO ceramics by increase donor defects .
4. By selectively doping Al_2O_3 , TiO_2 and MgO in ZnO ceramics, the effect of single or co-doped Al, Ti or Mg on the phase structure, microstructure and electrical properties of ZnO ceramics has been investigated.
5. The $\text{Al}_{\text{Zn}}\text{-Zn}_i$ complex produced by doping with Al element is closely related to the high electrical conductivity, and the generated conduction electrons can be detected and analyzed by the Knight shift effect on the NMR spectra and the specific relaxation mechanism of the EPR spectra, thereby $\text{Al}_{\text{Zn}}\text{-Zn}_i$ complex is determined to be an important shallow donor defect to improve conductivity.

Chapter 1

Introduction

1.1 Structure of ZnO conductive ceramics

1.1.1 Crystal structure and basic properties of ZnO

The crystal structure of zinc oxide (ZnO) includes cubic rock salt, cubic sphalerite and hexagonal wurtzite, of which only hexagonal wurtzite is a thermodynamically stable structure under normal temperature and pressure^[1], which is also the main ZnO conductive ceramic Physical composition. The crystal structure of the hexagonal wurtzite structure of ZnO^[2] is shown in Figure 1.1 (a). The basic ZnO cell is composed of four atoms of two Zn and two O in Figure 1.1 (b). The wurtzite ZnO structure belongs to the 6mm (or C_{6v}) point group and the $P6_3mc$ (or C_{6v}^4) space group. The lattice parameters are: $a = 3.2498 \text{ \AA}$, $b = 3.2498 \text{ \AA}$, $c = 5.2066 \text{ \AA}$ (JCPDS card No. 36-1451)^[3], where the value of c/a is about 1.60, which is close to the ideal axial ratio of close-packed hexagonal structure $c/a = 1.633$ ^[4]. Zn and O are arranged along the c -axis direction according to the ABAB hexagonal close-packed structure, and then the two hexagonal close-packed structures are translated along the c -axis direction by a length of $5/8 \times c$ to form a hexagonal wurtzite ZnO structure. The structure can also be regarded as being composed of multiple alternating planes composed of O and Zn of tetrahedral coordination alternately stacked along the c -axis. A zinc atom in the hexagonal wurtzite structure is surrounded by four oxygen atoms in a tetrahedron. The zinc atoms are located in the tetrahedral sites composed of four adjacent oxygen atoms, and occupy only half of the oxygen tetrahedral sites, and vice versa, oxygen atoms occupy half of the tetrahedral sites composed of zinc atoms, forming a loose structure easily doped with other elements.

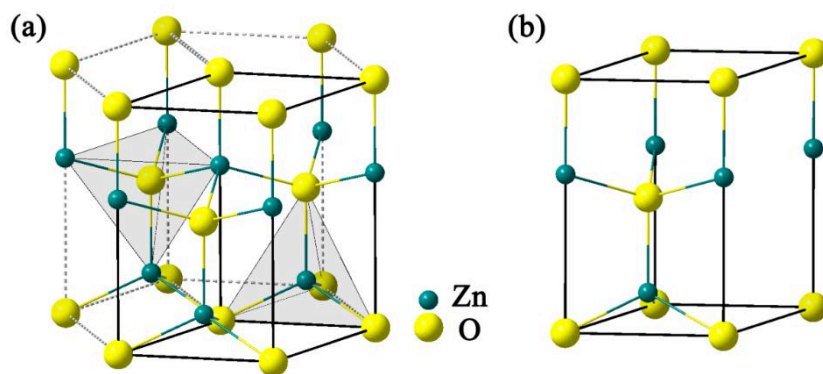


Figure 1.1 (a) The wurtzite ZnO structure, (b) The wurtzite ZnO unit cell

ZnO is a semiconductor belonging to group II-VI, and its properties are between ionic semiconductors and covalent semiconductors with a covalent chemical bond of sp^3 hybrid orbital. The large electronegativity difference between Zn and O atoms makes it have partial ionic bond characteristics. Based on the first-principles calculation of density functional theory, the conduction band of pure ZnO is mainly composed of 4s state of Zn and 2s state of O, and the valence band is mainly composed of 3d state of Zn and 2p state of O. The lowest unoccupied molecular orbital (LUMO) and the highest occupied molecular orbital (HOMO) of ZnO nanograins are determined by the 4s state of Zn and the 2p state of O[5], respectively, as shown in Figure 1.2, indicating that ZnO is a direct wide bandgap semiconductor with a band gap of 3.37eV at room temperature. By adjusting the ZnO material doping process, preparation conditions and other parameters can change the ZnO state density distribution, and then adjust the performance of ZnO material.

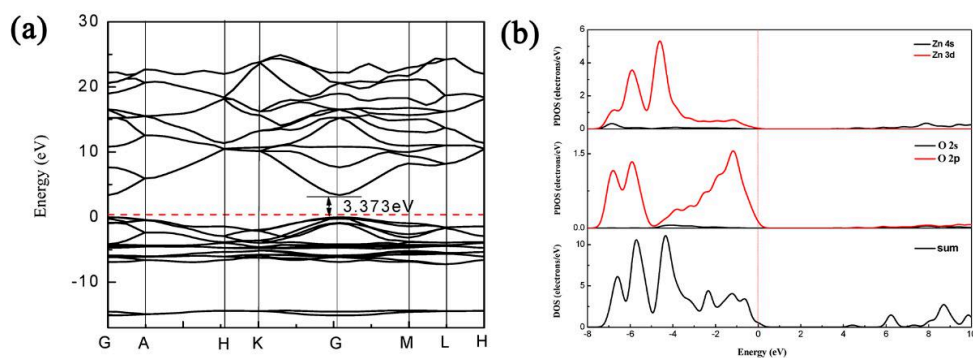


Figure 1.2 (a) Band structure and (b) Partial density of states (PDOS) for ZnO

Table 1.1 summarizes the parameters of the basic structure, physical and chemical properties of wurtzite ZnO^[6, 7], which shows that it has excellent and stable properties. At the same time, ZnO has the characteristics of high output, low price and non-toxic and harmless, resulting in ZnO being widely used in rubber, coatings, ceramics, electronics, medicine, glass and chemical industry.

Table 1.1 Basic properties of wurtzite ZnO

Parameters	Value
Space group	P6 ₃ mc or C _{6v} ⁴
Lattice constant	a=b=3.2498 Å, c=5.2066 Å
Density	5.606 g/cm ³
Melting point	1975 °C
Thermal conductivity	0.6 W/cm·K(axis a), 1.2 W/cm·K(axis c)
Thermal expansion coefficient	a ₀ =6.5×10 ⁻⁶ , c ₀ =3.0×10 ⁻⁶
Refractive index	2.008(axis a), 2.029(axis c)
Exciton binding energy at room temperature	60 meV
Static permittivity	8.656
Band gap at room temperature	3.37eV
Intrinsic carrier concentration	<10 ⁶ cm ⁻³
Electronic quality	0.24m ₀
Hole effective mass	0.59m ₀
Electron Hall mobility at room	200 cm ² /V·s
Hole mobility at room temperature	5~50 cm ² /V·s
Intrinsic resistance	9.94×10 ³ Ω·cm

1.1.2 Structure of ZnO conductive ceramic

The phase structure of ZnO conductive ceramics is mainly ZnO grains with hexagonal wurtzite, and also contains a few spinel grains related to doping elements and grain boundaries distributed between ZnO grains, the corresponding microstructure schematic diagram is shown in Figure 1.3.

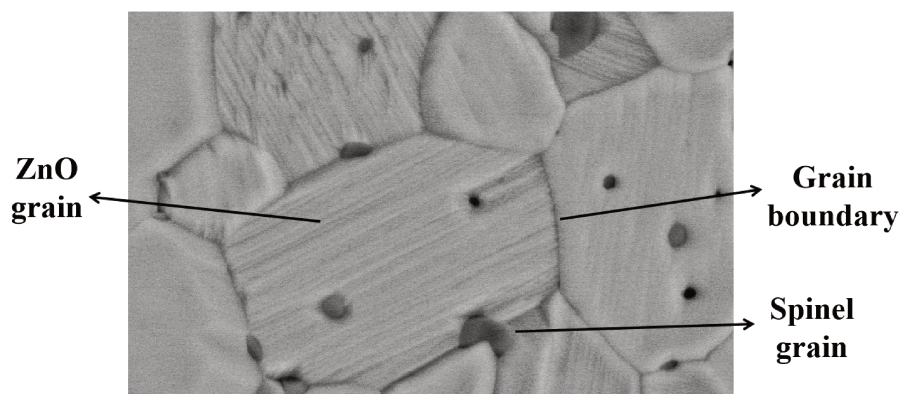


Figure 1.3 Schematic diagram of the microstructure of ZnO conductive ceramics

1.1.2.1 ZnO grain

There are a large number of ZnO grains with different shapes and different orientations in ZnO ceramics, which are generally isotropic. ZnO grains, occupying more than 90% of the volume of ceramics, is the main part that determines the performance of ceramics. The ZnO grain size has an important influence on the electrical properties of ZnO ceramics, for example: reducing the grain size of ZnO varistor can significantly improve the breakdown voltage and energy absorption density^[8], and increasing the grain size can reduce the room temperature conductivity of ZnO ceramics^[9]. In ZnO ceramics, the ZnO grain size is generally in the range of 2-20 μm , depending on the size of the raw material powder, the content of the second phase and the sintering preparation method^[10-12]. The free electron concentration in the ZnO grains is very low, thus the intrinsic resistivity is $9.94 \times 10^3 \Omega \cdot \text{cm}$, which is close to the insulator. The resistivity is very large compared to conductive metals (such as the resistivity of Cu is $1.75 \times 10^{-8} \Omega \cdot \text{cm}$), and is far from meeting the requirements of conductive resistors. Therefore, the most important way is to reduce the resistance value of ZnO grains to obtain ZnO conductive ceramics. Generally, donor or acceptor dopants are added during the preparation of ZnO ceramics to obtain an increased concentration of donor carriers or acceptor carriers in the ceramic to greatly enhance the electrical conductivity^[13]. Thus, the process of "semiconducting" of insulating ZnO grains is realized. In addition to improving electrical conductivity,

the introduction of doping elements will also affect the shape, size, growth rate of ZnO grains and the structure of ZnO ceramics. For example: Doping Sn can adjust the size and shape of ZnO grains^[14]; the inversion boundary generated after doping Sb will also affect the size and shape of grains^[15]; doping Ti can increase the density of ceramics^[16].

1.1.2.2 Grain boundary

The grain boundaries of ZnO conductive ceramic are clean interfaces that ZnO grains directly contact, which is very different from the amorphous grain boundary layer of ZnO varistor^[17], as shown in Figure 1.4. The interface between ZnO grains with different orientations and irregular atomic arrangement is the ZnO-ZnO grain boundary. Many defects such as vacancies, gaps, and dislocations exist in the grain boundary with relatively loose structure. Thus the grain boundary has great stress distortion and high energy, and the process of nucleation, growth and growth of the second phase is easy to occur. Therefore, most of the spinel grains in the ceramic are distributed in the grain boundary.

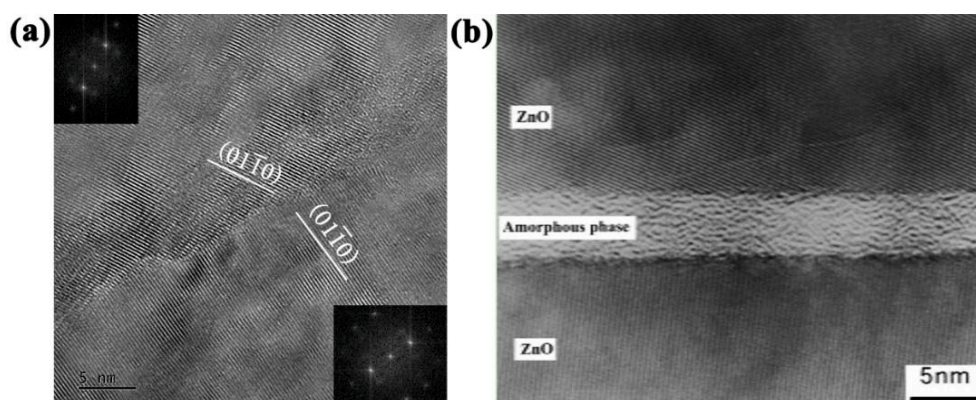


Figure 1.4 ZnO grain boundary structure: (a) Conductive ceramic, (b) Varistor

The special structure of the grain boundary is easy to cause the intrinsic acceptor defects V_{Zn} and O_i to gather^[9], which leads to the imbalance of the potential of the grain and the grain boundary. Generally, the Fermi energy level of crystal grains is higher than that of grain boundaries. Therefore, the conductive electrons near the grain boundary in the N-type ZnO grain are easily captured by the grain boundary,

and free electrons will enter the grain boundary with low Fermi level from the grain with high Fermi level. When the equilibrium is reached, a negatively charged enrichment layer is formed at the grain boundary and a depletion layer with a certain width composed of positively charged donor ions (D_{Zn}^{\bullet}), intrinsic oxygen holes (Vo^{\bullet} and $Vo^{\bullet\bullet}$) and intrinsic zinc interstitials (Zn_i^{\bullet} and $Zn_i^{\bullet\bullet}$) is formed outside the ZnO grains near the grain boundary, which deforms and bends the energy band, resulting in the Schottky barrier structure ^[18] shown in Figure 1.5. The Schottky barrier in ZnO ceramics hinders the transport of electrons within the grains, significantly reduces the carrier mobility, and is not conducive to improving the electrical conductivity. Meanwhile, the barrier causes the grain boundary and the grain to have different resistances, which causes the nonlinear volt-ampere characteristic curve of the ZnO resistor^[19].

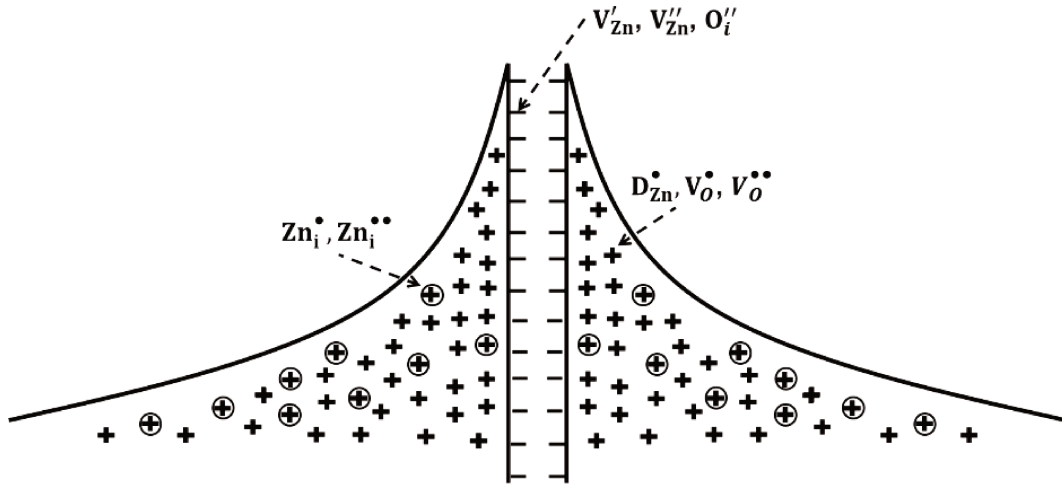


Figure 1.5 Schematic diagram of ZnO grain boundary barrier

According to the electrical neutrality condition and Poisson's equation, the relationship between the barrier height and the donor and acceptor concentrations in the ceramic is in accordance with equation (1.1)^[20],

$$\phi_B = \frac{e^2 N_S^2}{2\epsilon_0 \epsilon_r N_D} \quad (1.1)$$

Among them, ϕ_B is the barrier height, e is the electrons' concentration, ϵ_r is the relative dielectric constant, ϵ_0 is the vacuum dielectric constant, N_D is the donor

doping concentration, and N_S is the acceptor concentration.

Therefore, a conductive ZnO ceramics with excellent performance can be obtained by reducing or eliminating the barrier of ZnO ceramics. By doping donor elements such as Al into the grains to increase the electron concentration of ZnO grains^[21] or decreasing the acceptor concentration at the grain boundaries by reducing atmosphere sintering^[22], the Schottky barrier can be significantly reduced to improve electrical performance.

1.1.2.3 Spinel phase

The spinel grains depend on the type and content of the dopant. When the doping content exceeds the solid solubility of the corresponding element in ZnO, a second phase of spinel can be produced, such as $ZnAl_2O_4$, Zn_2TiO_4 , etc.^[23, 24]. The ratio of spinel phase in ZnO conductive ceramics is small, and the size is much smaller than that of ZnO grains. The spinel particles are embedded in the ceramic and distributed in the grain boundaries and inside the ZnO grain, which has an important influence on the properties of the ceramics. Spinel is a face-centered cubic structure with loose structure, which is easier to dissolve other doping elements to adjust their solid solubility in the ceramic, and then affect the overall electrical performance^[25]. Spinel can prevent the growth of ZnO grains through the pinning effect to reduce the size of ZnO grains and increase the number of grain boundaries^[26], as shown in Figure 1.6. The larger the size and content of the spinel grains, the greater the pinning force, and the stronger the effect on the ZnO grains and grain boundaries^[27]. In addition, spinel is an insulator, which limits the effective conductivity of ZnO ceramics by hindering and scattering electron transmission. Therefore, the content and distribution of spinel in ZnO conductive ceramics have the effect of adjusting its conductivity. In order to obtain high conductivity, the dopant content should be limited to the solid solubility^[28]. Besides, the solid solubility can be improved by suitable preparation methods (such as spark plasma sintering (SPS), atmosphere sintering and sintering temperature^[29, 30]), so that all the doping elements are present in ZnO, and the conductive ceramics

appear to contain only ZnO grains and grain boundaries.

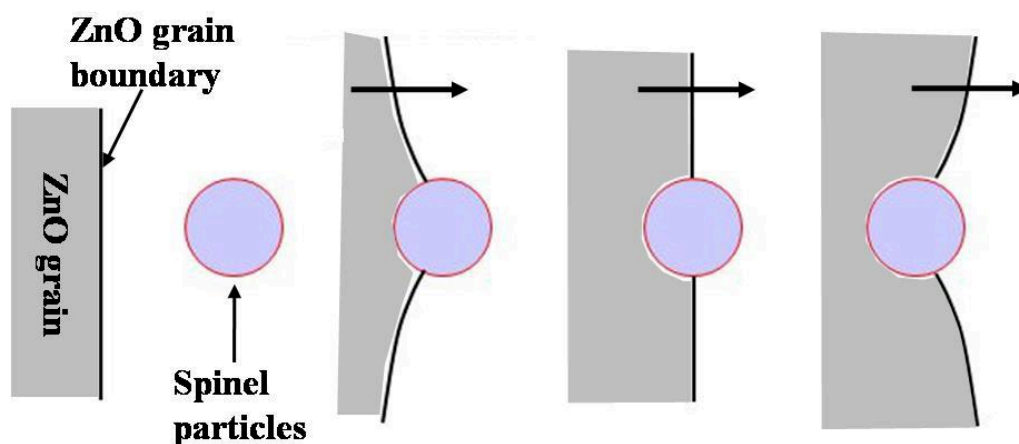


Figure 1.6 Schematic of the pinning effect of spinel on grain growth

ZnO conductive ceramic is composed of low-resistance ZnO grains, grain boundaries with barriers and insulated spinel grains. The conductive body is the conductive path formed by the interconnection of ZnO grains. The grain boundaries hinder the electron transmission between the ZnO grains, while the other spinel grains act as insulators to block or reduce the conductive path. Conductive ZnO grains, high-resistance grain boundaries and insulated spinel grains form a complex series and parallel structure, which together determine the electrical properties of ceramics.

1.2. Electrical properties of ZnO conductive ceramics

1.2.1 Electrical Conductivity

Resistivity, or electrical conductivity, is the most important electrical parameter of ZnO conductive ceramics. In ZnO-based conductive ceramics, conductive ZnO grains, high-resistance grain boundaries and spinel grains form a complex series and parallel structure to jointly affect the electrical conductivity of the material, which can be explained by the model of percolation conduction^[31] shown in Figure 1.7(a). Conductive ZnO grains with resistivity in the range of 1-10 $\Omega\cdot\text{cm}$ are connected to form a network structure, forming a continuous conductive path in the ceramic; The

barrier height of the grain boundary is a key factor. High conductivity requires a very low barrier height to form an ohmic contact; Spinel with high resistivity of generally above $10^8 \Omega \cdot \text{cm}$ ^[32], such as ZnAl_2O_4 , are distributed in ceramics and do not play a role in conductivity, but mainly play a role in regulating the conductive path. The equivalent circuit diagram of the ZnO conductive ceramics is shown in Figure 1.7(b). ρ_g , ρ_{gb} and ρ_i respectively represent the resistivity of ZnO grains, grain boundaries, and spinels, and C_{gb} represents the capacitance caused by the grain boundary barrier. By controlling the content of the dopant within the solid solubility of ZnO, almost no spinel is generated in the ceramic, and the regulating conductive path effect is almost negligible. In this case, the resistivity of the ceramic mainly depends on the resistivity of ZnO grains and grain boundaries. The resistivity of ZnO conductive ceramic refers to the following equation:

$$\rho = \rho_g + \rho_{gb} \times \frac{t}{d} \quad (1.2)$$

Among them, t is the grain boundary width, d is the ZnO grain size. In the ZnO conductive ceramic, ZnO grains can directly contact, thus t is much smaller than d .

Therefore, a highly conductive ZnO ceramic can be obtained by reducing the resistivity of ZnO grains and grain boundaries.

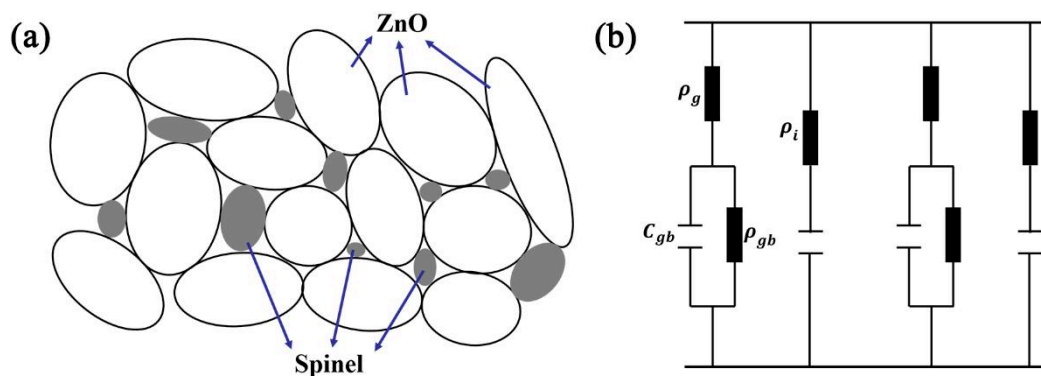


Figure 1.7 Schematic diagram of (a) Model of percolation conductivity, (b) Schematic of equivalent circuit of ZnO conductive ceramics

1.2.2 Temperature coefficient of resistance (TCR)

The resistance or resistivity of most conductive materials changes with changes in temperature. Defining the change rate of the resistance value at a temperature change of 1 °C is the temperature coefficient of resistance (TCR) in ppm / °C, which can be expressed by the following formula:

$$\text{TCR} = \frac{R_x - R_0}{R_0(T_x - T_0)} \quad (1.3)$$

Among them, R_0 is the resistance value at the reference temperature T_0 (usually 20 °C), R_x is the resistance value at the test temperature T_x .

Figure 1.8 intuitively shows the difference between typical metal and semiconductor resistivity changes with temperature. In metals, as the temperature increases, the random movement of free electrons and the vibration of atoms will increase, resulting in more collisions and hindering the movement of conducting electrons. Thus the resistance of the metal will increase with increasing temperature and exhibit a positive TCR. Semiconductors at high temperatures have enough energy to break more covalent bonds and can generate more free electrons, which means that a large number of electrons can pass the band gap when the temperature rises, thereby increasing the electrical conductivity by increasing the free electrons. Therefore, free electrons in semiconductors increase with increasing temperature, resulting in semiconductors that generally have a negative TCR, showing a decrease in resistance with increasing temperature.

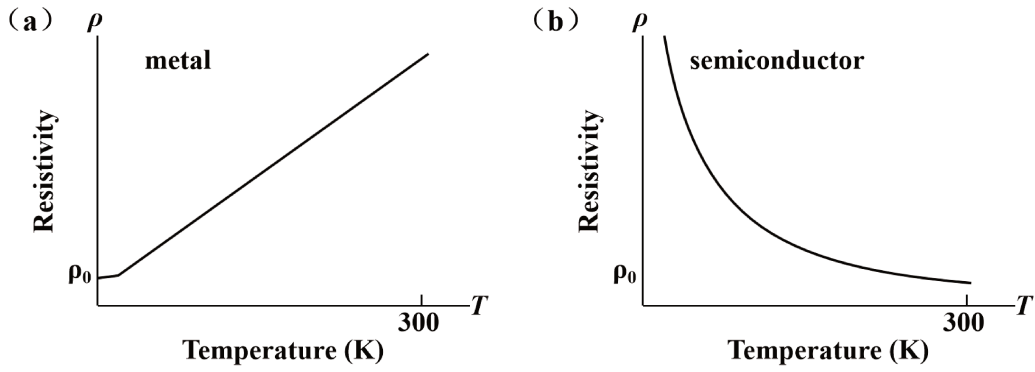


Figure 1.8 Resistivity versus temperature for typical metals-(a) and typical semiconductors-(b)

TCR is one of the main parameters characterizing the performance of the resistor. The negative TCR of the ZnO semiconductor ceramic causes the resistance to decrease when the temperature rises, so that when the operating voltage is constant, the current increases rapidly, and the ZnO ceramic resistor is easily broken down. Therefore, in order to ensure the stable operation of the ZnO ceramic resistor in the circuit system, the TCR of the ZnO ceramic resistor can be adjusted to a small positive value through doping and other processes^[49-51]. In this case, the resistance increases slightly with increasing temperature, and thermal breakdown does not occur.

1.2.3 Nonlinear coefficient

According to the volt-ampere characteristic curve of ZnO ceramics, the following expression is usually used to calculate the nonlinear coefficient α ^[33]:

$$\alpha = \lg \frac{I_2 / I_1}{V_2 / V_1} = \frac{\lg I_2 - \lg I_1}{\lg V_2 - \lg V_1} \quad (1.4)$$

In the formula, I_1 and I_2 are two different current values ($I_1 < I_2$), and V_1 and V_2 are the voltage values measured under the corresponding current values. For ZnO varistor ceramics, I_1 and I_2 are current values per unit area, and $I_1 = 1\text{mA/cm}^2$ and $I_2 = 10\text{mA/cm}^2$ are generally selected; For ZnO linear conductive ceramics, I_1 is generally room temperature current, I_2 is the upper limit current for measurement, and the

calculated α characterizes the volt-ampere characteristic of the measurement range.

ZnO varistor does not have a linear current-voltage curve, and generally has a α greater than 30. As shown in Figure 1.9, the resistance is determined by the grain boundaries and grains in ZnO ceramics under different currents^[34, 35]. ZnO varistors are often used to protect circuits, and are usually connected in parallel with the components that need to be protected. Under normal operating current, ZnO varistor has a large resistance, showing an open circuit state; When the current suddenly increases, the grain boundary resistance is broken down, and the ZnO varistor exhibits a small resistance dominated by ZnO grains. The suddenly increased current flows through the ZnO varistor, so that the protected components will not be damaged due to the ZnO varistor short circuit.

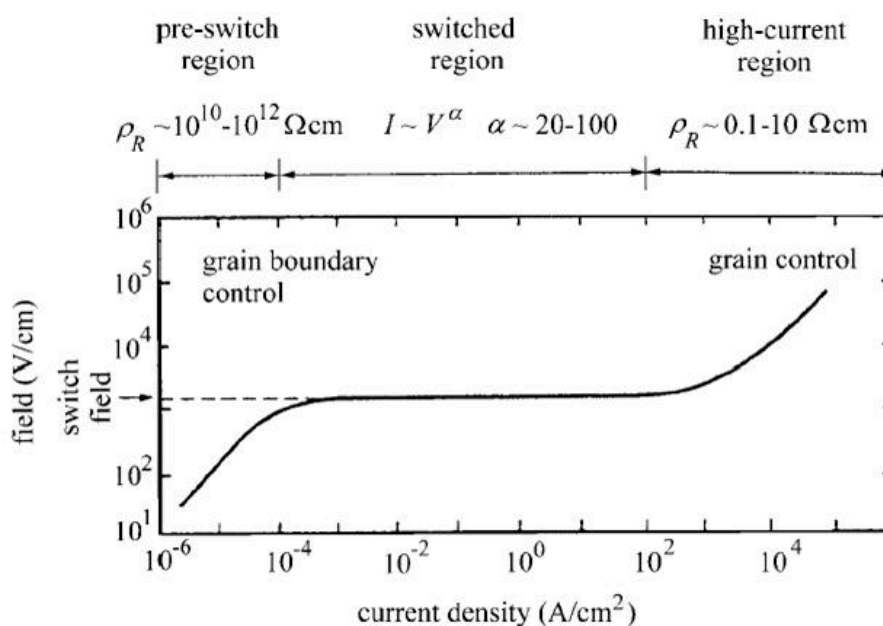


Figure 1.9 Current versus voltage curve of ZnO varistors

The α can also be used to characterize whether ZnO conductive ceramics have ideal ohmic characteristics, used to reflect its stability. For a resistive device, the optimal state is $\alpha = 1$. In this case, a constant resistance under different currents or voltages can ensure the stable operation of the resistive device in the working circuit. The α is mainly affected by the electron scattering generated by the disordered structure or the barrier at the grain boundary, and the higher the barrier, the greater the α ^[36]. Due to

various defects between ZnO grains and grain boundaries, a small potential barrier is produced, so ZnO linear conductive ceramics still have an α close to 1, generally between 1 and 1.2. The ZnO conductive ceramic with α as close to 1 as possible can be obtained by lowering barrier at the grain boundaries^[34].

1.2.4 Energy Density

The energy density of the ZnO ceramic resistor refers to the maximum dissipated heat energy per unit volume of the ceramic resistor, and also the maximum energy before thermal breakdown. Generally, the ZnO ceramic is impacted by a high-energy pulse current, and the applied current is gradually increased until the ceramic is broken down. According to the corresponding resistance and pulse width, the energy density (E) of the ZnO ceramic is calculated using the following expression in J/cm³.

$$E = \frac{I^2 R t}{V_0} \quad (1.5)$$

In the formula, I is the maximum impact current, t is the pulse width, R is the resistance, and V_0 is the volume of the ZnO ceramic.

Energy density can determine the service life of electronic components, and high energy density can ensure stable operation under high pressure. The uneven temperature distribution caused by the conversion of electrical energy into thermal energy will cause the ceramic to be destroyed after the thermal stress generated in the ceramic exceeds the tolerance limit^[37]. The energy density is mainly related to the density and structural uniformity of the material^[38], so it can be increased by increasing the density of the ceramic and controlling secondary phases, such as reducing the content of pores or texturing the structure^[39].

1.2 Defect features and doping effects in ZnO

The intrinsic defects existing in the ZnO lattice affect the basic properties of ZnO, and

various extrinsic defects generated by doping ZnO according to the application requirements affect the corresponding semiconductor properties.

1.2.1 Intrinsic defects

Due to the thermal migration of atoms and the external environment during the growth process, intrinsic point defects such as oxygen vacancies (V_O), interstitial zinc (Zn_i), zinc vacancies (V_{Zn}), interstitial oxygen (O_i) and zinc antisites (Zn_O), oxygen antisites (O_{Zn}) generally exist in ZnO crystals. ZnO of group II-VI is a typical N-type semiconductor material in which donor defects play a major role. Figure 1.10 depicts a schematic diagram of the main defect electronic energy levels involved in ZnO^[40].

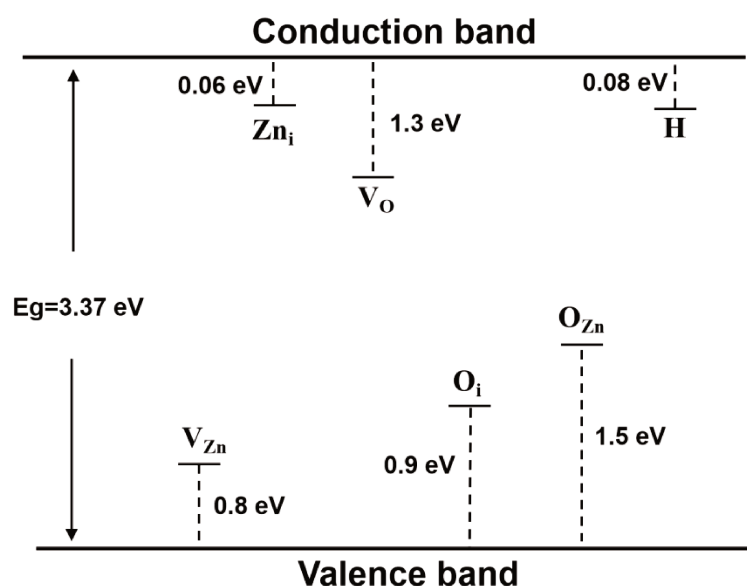


Figure 1.10 Schematic diagram of the electronic energy levels of main defects involved in ZnO

Donor intrinsic defects V_O and Zn_i are generally considered to cause N-type characteristics^[41, 42], and some researchers have suggested that the hydrogen ions (H^+) introduced during the preparation of ZnO have donor characteristics, which is the reason for N-type conduction^[43, 44]. M. D. McCluskey's first-principle calculations show that V_O in deep donor state is difficult to be ionized to increase the conductivity, thus denying the donor role of V_O ; at the same time, it proves the donor role of

hydrogen ions^[45, 46]. Lishu Liu believes that the theoretical calculations that negate the donor effect of V_O are not reliable, because the calculated formation energy and concentration range of V_O are very different from the actual experimental results, and there is a lack of discussion on the V_O valence. Through their study of oxygen diffusion in ZnO, they pointed out that the divalent V_O near the edge of the conduction band is the main donor point defect that leads to the non-stoichiometric and N-type conductivity of ZnO^[47]. K. Bandopadhyay proved by photoluminescence spectroscopy that the Zn_i - V_O complex with a lone pair of excitation energy close to the band gap can produce a strong violet blue light, which is the source of N-type conductivity^[48]. Infrared spectroscopy of O-H vibration shows that H occupies the reverse bond configuration, and needs to be recombined with V_{Zn} due to unstable O-H^[49]. Therefore, based on the current research results, we infer that although H has a weak donor effect, the source of intrinsic N-type conductivity in ZnO is still Zn_i and V_O defects with specific electronic configuration and coordination environment.

1.2.2 Extrinsic defects

Although pure ZnO ceramics have N-type conductive characteristics, but the intrinsic carrier concentration is very small (approximately 10^6 cm^{-3}), so the poor conductivity is far from the needs of conductive ceramics. The most effective way to improve the electrical conductivity of ZnO ceramics is to add suitable dopants and generate corresponding extrinsic defects to form impurity semiconductors with high conductivity^[50]. According to different types of dopants, ZnO semiconductors can be divided into N-type ZnO semiconductors dominated by electron carriers and P-type ZnO semiconductors dominated by hole carriers. Elements, such as Li, Na, Cu, and N, can be used as P-type acceptor centers for replacing cation Zn^{2+} or anion O^{2-} ^[51-53], which can increase the acceptor carrier concentration in order to increase the conductivity. Based on the weak N-type conductivity of ZnO, it is easier to obtain improved conductivity through N-type doping. The P-type doping has the characteristics of self-compensation and poor stability^[54], which makes it difficult to

increase the carrier concentration, and even converts from P-type to N-type semiconductor^[55, 56]. Therefore, the conductivity of ZnO ceramics is usually improved by N-type doping in the ZnO ceramics.

Generally, the cation or anion with more electrons in the outer shell is substituted for Zn or O to achieve N-type doping. The most common cations to replace Zn are the IIIA elements Al, Ga and In, which act as shallow donor doping elements^[3, 13, 57] to greatly increase the electron concentration in the doped ZnO ceramics. It has been reported that Al or Ga-doped ZnO can achieve a carrier concentration greater than 10^{20} cm^{-3} , and realize a degenerate electronic state in the conduction band, showing that the Fermi level has shifted to the conduction band^[58-60], making an easier electron transition in ZnO. In addition, Ti and Co can also be used as donor doping elements^[61, 62] to substitute and occupy a few of Zn sites to form N-type donor centers, which can increase the free electron concentration and then increase the conductivity of ZnO. Another way to form N-type ZnO semiconductor is to add Cl element of group VII to substitute the O anion site^[63, 64]. The ZnO ceramics sintered by the chemical vapor transmission of Cl gas can form a shallow donor Cl to reduce resistivity^[65]. So far, due to the complex preparation process of anion substitution and poor ability to improve the conductivity, anionic N-type doping in ZnO ceramics is not common. In these donor dopants, due to the similarity of the radius of Al and Zn and the high solid solubility, Al replaces Zn to form a shallow donor with a higher concentration of Al_{Zn} , which can greatly provide the N-type conductivity of ZnO. Therefore, Al is the best choice for preparing highly conductive ZnO-based ceramics due to its strong donor effect.

Higher solid solubility of Al in ZnO ceramics leads to produce the higher concentration of shallow donor Al_{Zn} , so the key to prepare highly conductive ZnO ceramics is to improve the solid solubility of Al in the ZnO lattice. Solid solubility is mainly affected by the preparation parameters of ZnO ceramics, such as preparation way, sintering atmosphere and sintering method. Sol-gel, solvothermal reaction and

other chemically synthesized preparation ways can improve the efficiency of Al replacing Zn to increase electrical conductivity^[66, 67]; low-oxygen partial pressure sintering environments, such as vacuum, nitrogen, reducing atmosphere can help Al to replace Zn in ZnO. The greatly increased concentration of Al_{Zn} and Zn_i can make its conductivity reach 10⁷ times than that of samples sintered in air^[30, 68]; spark plasma sintering, hot-press sintering, microwave sintering, etc. can enhance the density of the structure to achieve the solid solution of Al to enhance the conductivity of Al-doped ZnO materials^[29, 69-71].

1.2.3 Experimental methods for defect studies

The electrical properties of ZnO conductive ceramics have a strong correlation with defects, so it is necessary to find appropriate defect testing methods to characterize the type, concentration and distribution of defects in the ceramics to explain the mechanism problems related to the electrical properties. Commonly used defect test methods include infrared spectroscopy (IR), Raman spectroscopy, photoluminescence spectroscopy (PL), electron paramagnetic resonance spectroscopy (EPR) and nuclear magnetic resonance spectroscopy (NMR). IR is mainly used to detect H-related defects to explain its effect on conductivity, IR testing of hydrothermal grown ZnO and ZnO grown from the vapor phase showed that the presence of H-V_{Zn} complex and the characterized H at 3611.3 cm⁻¹ contributed to the N-type conductivity of ZnO^[72]. It is worth noting that, due to the high temperature and atmosphere sintering, the ZnO ceramics prepared by the solid phase reaction contain very few H defects, so H is not the main reason for the high conductivity. It is reported that IR can also use formaldehyde probe molecules to detect V_O defect sites on the surface^[73]. Raman spectroscopy can be used to analyze the defect structure caused by Zn_i, V_O and doping in ZnO according to the characteristic vibration frequency of different defects, and can explain the corresponding defect concentration and configuration^[74-77]. The absorption and emission of light can reflect the electronic transition and recombination behavior of the energy band structure, and then infer the type of

corresponding defects. The band gap can be calculated based on the position of the absorption peak in the UV absorption spectrum, and the blue shift in ZnO indicates an increase in the concentration of donor defects^[78]; the PL spectrum can detect excitation light with a specific wavelength or energy, and the types of structural defects causing energy level transitions can be derived from different spectral bands^[48], and then the defects that affect the performance of ZnO materials can be analyzed. In addition, X-ray photoelectron spectroscopy can be used to characterize the situation of O-related substances and to analyze the valence of O and V_O concentration^[79]. EPR and NMR are local probe techniques that can analyze the types of characteristic defects and the local environment. EPR can be used to detect paramagnetic defects in ZnO, mainly including V_O, Zn_i, V_{Zn}, and defects containing unpaired spin $S = 1/2$ introduced by doping, which is useful to understand the electrical behavior of ZnO materials. The EPR line of $g = 1.96$ indicates the characteristic shallow donor defects in ZnO. It is reported that it may originate from Zn_i intrinsic defects or shallow donor defects caused by dopants In, Ga, Al, H, etc.^[80-84], which needs to be analysed by the doping and the preparation process; the EPR lines with g factors around 1.99 and 2.00 characterize V_O and V_{Zn} respectively^[85, 86], and the distribution and content of corresponding defects in ZnO can be inferred from the line shape. NMR is a technique to detect the local environment around an atomic nucleus whose magnetic moment is not zero. Defects that affect electrical performance can be determined by detecting the atoms coordination. For Al-doped ZnO, the local environment of ²⁷Al and ⁶⁷Zn nuclei can be characterized by NMR^[87-89]. Despite the low resolution of ⁶⁷Zn, the disorder structure around Zn caused by doping can be analyzed by the NMR spectrum. For ²⁷Al, the NMR lines around 0 ppm and 80 ppm characterize the four-coordinated and six-coordinated Al in ZnO and correspond to the Al_{Zn} and the Al_i located in the octahedral interstitial sites, respectively. In addition, the NMR signal in Al-doped ZnO ceramics far from the conventional shift range is related to high conductivity, and the high concentration of delocalized electrons induced in ZnO acting on Al_{Zn} can cause the shift of related lines^[90].

1.3 Applications, recent advances and trends in ZnO based materials

1.3.1 Application of ZnO-based semiconductor

ZnO is a multi-functional material with excellent semiconductor properties. In addition, it has the advantages of high stability, high temperature resistance, oxidation resistance, abundant raw materials, low price, and environmental friendly. Therefore, ZnO has wide applications in the fields of conductive, thermoelectric, photoelectric, magnetic, gas sensitive, photosensitive and moisture sensitive materials.

Highly conductive ZnO ceramics play an important role in circuits such as conduction circuits, ultra-high voltage transmission and transformation circuits and protection circuits. Due to the characteristics of ceramics such as high chemical stability, strong corrosion resistance, and wide application temperature, ZnO ceramic resistors can operate stably in complex environments with severe cold, extreme heat, humidity, or corrosion. In addition, it has the characteristics of easy resistance adjustment, high linearity, small TCR, high energy density, small inductance, low cost, and easy production. Therefore, ZnO ceramic has great advantages in the application of circuit breakers, energy release resistors, grounding resistors and non-inductive resistance devices, energy absorption devices, surge absorption devices, rectification equipment, lightning protection devices, etc.^[91-96]. The current devices tend to be miniaturized, so it is necessary to study the resistance adjustment methods of ZnO ceramics and the preparation measures of highly conductive ZnO ceramics.

In 1968, Panasonic Corporation in Japan developed nonlinear ZnO varistor, which is one of the mature and widely used achievements of ZnO ceramic. The non-linear volt-ampere property of ZnO varistors ensures its normal operation in circuits with severe voltage fluctuations, thus ZnO varistors are mainly used for overvoltage protection circuits. ZnO varistor is connected in parallel with the components to be

protected, so that the circuits will not be damaged by the impact of high voltage or strong current, and can greatly provide the service life and safety of the equipment. Therefore, ZnO varistors play an important role in power transmission systems, communication network components, power supply and microelectronic devices^[97-99].

The thermoelectric material is an environment-friendly material that can utilize the migration of carriers in the material to realize the conversion of thermal energy and electrical energy. N-type ZnO high-temperature thermoelectric materials with higher carrier concentration obtained by doping modification and different preparation processes have high research and application value. A large number of studies have focused on comprehensively regulating electrons and phonons to obtain the best thermoelectric figure of merit to improve the conversion efficiency between electricity and thermal energy. ZnO thermoelectric materials can efficiently convert the thermal energy of solar energy, industrial waste heat, automobile exhaust, and bio-heat into electrical energy, and play an important role in thermal power generation^[100-103].

Mn, Fe, Co or Ni-doped ZnO-based dilute magnetic semiconductors have both semiconductor and magnetic material properties, and therefore have broad application prospects in spintronic devices, semiconductor lasers, magnetic sensors, non-volatile memories, etc.^[104, 105]. Based on the versatility of ZnO semiconductors, researchers have also used their electrical conductivity sensitivity to specific gases to prepare gas-sensitive materials, which can monitor and alarm harmful gases in the environment^[106, 107]; moisture-sensitive materials with different compositions and morphologies have been prepared using the dependence of surface conductivity on environmental humidity^[108]; the thermistor has been developed based on the negative TCR of ZnO semiconductors such as Zn-Ni-O and Mn-Co-Cu-Zn-O, which is used as a temperature protection device to protect the circuit from thermal shock^[109, 110]. Furthermore, the N-type doped ZnO semiconductor with a wide band gap prepared by a special way is a transparent conductive oxide (TCO) material in the visible region,

which can be used in solar cells, liquid crystal displays and energy-saving thermal insulation coatings^[111, 112].

1.3.2 Advantages of ZnO conductive ceramics

The main research object of this thesis is ZnO-based ceramics with high conductivity, which plays an important role in the circuit as ceramic resistors. In some cases, ZnO-based ceramics resistors can replace metal or carbon resistors, so it is necessary to explain the superiority of ZnO conductive ceramic resistors. Metal resistors and carbon-based resistors are still the materials of choice for widely used resistance devices. However, they are not suitable in some special application environments and conditions, so it is necessary to study a new type of ZnO-based ceramic resistor which is expected to replace metal resistors and carbon-based resistors in certain fields with the improvement of performance and preparation technology. Compared with traditional metal resistors and carbon-based resistors, ZnO ceramic resistors have the advantages of high strength, corrosion resistance, oxidation resistance, chemical stability and thermal stability, small size and light weight. The electrical properties of ZnO conductive ceramic resistors also have unique highlights. The differences in electrical properties of metal resistors, carbon-based resistors, and ZnO ceramic resistors are summarized in Table 1.2, it can be seen that ZnO ceramic resistors have many superior properties^[113]. The resistance of ZnO conductive ceramics can be adjusted in a wide range to be suitable for many occasions; TCR is small and can be positive, the resistance is less affected by temperature, so the stability and safety are higher; the energy density of ZnO ceramic resistors can reach about three times that of metal and carbon series resistors, indicating that the volume is greatly reduced under the same energy absorption requirements, which is conducive to the miniaturization and lightness of the devices. Besides, the high energy density reflects the high instantaneous energy absorption and strong impact resistance, which can greatly improve the stability of the circuit and the service life of the device; the special structure of ZnO ceramic makes it resistant to thermal shock, not easily oxidized and

thermally corroded, so it is a good choice at high temperature. Stable performance and anti-shock, anti-oxidation, and corrosion-resistant characteristics make it very useful in extreme environments such as oil pollution, high temperature, low temperature, humidity, and seabed corrosion. Therefore, ZnO ceramic resistors can well meet the current high requirements for the power industry, have outstanding advantages in certain aspects.

Table 1.2 Properties of metal resistor, carbon resistor and ZnO ceramic resistor

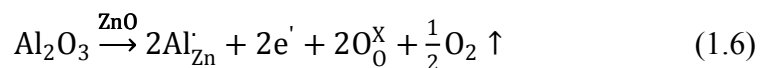
Parameter	Unit	Metal resistor	Carbon resistor	ZnO ceramic resistor
Resistivity	$\Omega \cdot \text{cm}$	$10^{-5} - 10^{-3}$	4×10^2	$1 - 10^4$
Temperature resistance coefficient	$1/^\circ\text{C}$	10^{-4}	-9×10^{-2}	$-5 \times 10^{-4} - 5 \times 10^{-4}$
Energy Density	J/cm^3	$2 \times 10^2 - 3 \times 10^2$	2×10^2	$5 \times 10^2 - 8 \times 10^2$
Stability	-	better	poor	better
The highest operating temperature	$^\circ\text{C}$	70	200	300

1.3.3 Contributions to improve the electrical conductivity

ZnO highly conductive ceramics have both conductive properties like metals and good stability of ceramics, thus playing an important role in the field of resistors. ZnO has abundant raw materials, easy extraction, and low cost, and ZnO conductive ceramics have simple preparation methods and excellent properties, which are suitable for industrial mass production. Therefore, the research and application of ZnO-based ceramic materials are popular. ZnO conductive ceramics obtained by adjusting specific experimental parameters have a wide range of applications in the fields of conduction resistors, linear resistors, thermoelectric devices, transparent conductive film targets, solar cells, etc.^[7, 114-117]. ZnO conductive ceramics with high conductivity can be obtained by increasing the carrier concentration and mobility. The main methods are: adding donor dopants can increase the conductivity by greatly increasing the carrier concentration; the similar orientation and regular structure

produced by the textured ceramics are beneficial to reduce the grain boundary barrier, and the carriers are easier to migrate to improve the conductivity; the effective sintering preparation method can also improve the conductivity by adjusting the ceramic structure; optimizing the sintering parameters and heat treatment process will also affect the electrical conductivity of ZnO ceramics.

Pure ZnO has a very low N-type conductivity due to intrinsic donor defects, so donor doping is the most effective and commonly used method to increase the conductivity of ZnO ceramics. Over the years, researchers have doped various donor elements in ZnO, the most common of which are Al, Ga, and In in group IIIA. Based on the ionic radius, coordination number and doping efficiency, Al can most effectively improve the conductivity of ZnO, so Al is currently the donor doping element that has been selected and studied. In 1984, Tadatsugu Minami prepared a highly Al-doped ZnO thin film, which proved that the resistivity after adding 1-2 wt% Al₂O₃ can be as low as $2 \times 10^{-4} \Omega \cdot \text{cm}$, indicating Al₂O₃ is beneficial to improve electrical conductivity^[118]. In 1996, Michitaka Ohtaki found in Al₂O₃ doped ZnO ceramics that Al solved into ZnO grains can increase the concentration of electron carriers, up to $6.5 \times 10^{19} \text{cm}^{-3}$, making the conductivity increase to $6.14 \times 10^4 \text{ S} \cdot \text{m}^{-1}$ ^[119]. KF Cai explored the correction between conductivity and doping ratio by adding 1-5 mol% Al₂O₃ to ZnO ceramics, and explained that doping Al can enhance the conductivity of ZnO ceramics by forming Al_{Zn} donors and generating more electronics according to the following expression:



Meanwhile, it was found that doping more Al₂O₃ will produce a high-resistance ZnAl₂O₄ phase, which is harmful to the increase in conductivity^[21]. Analogous to the doping effect of Al, the researchers also studied other donor doping elements^[120-125], such as Ga, In, Ti, Co, Sb, Ni, La, Y, which also produce donor defects to improve ZnO conductivity. However, due to their low solid solubility in ZnO to easily generate the second phase, the effect of improving the conductivity of ZnO ceramics is far less

than that of Al.

The Schottky barrier at the grain boundary hinders the migration of carriers, so that the electrical conductivity of ZnO ceramics cannot be effectively increased. The growth orientation of ZnO grains will have an important effect on the grain boundary structure and electrical properties of ceramics. The uniformly oriented ZnO grains can form a periodic grain boundary structure and reduce the Schottky barrier at the grain boundaries^[126]. Hisashi Kaga analyzed the microstructure and transmission characteristics of Al-doped ZnO textured conductive ceramics and found that a higher degree of texture can lead to a smaller scattering effect of ZnO grain boundaries on electron transport. Then the electron mobility was increased to obtain a room temperature conductivity of $1.4 \times 10^5 \text{ S} \cdot \text{m}^{-1}$, indicating that the conductivity is higher than that of non-textured ZnO ceramics^[127].

On the basis of adding appropriate dopants, optimizing the preparation and sintering process can obtain ZnO conductive ceramics with better properties. Yoshinobu Fujishiro^[128] hot-pressed the $\text{Zn}_{1-x}\text{Al}_x\text{O}$ nano-powders obtained by co-precipitation and spray drying to prepare ZnO polycrystalline ceramics with improved conductivity. The corresponding ZnO ceramic prepared has very compact structure to increase the carrier concentration and mobility, so the electrical conductivity has been increased^[128]. Tian Tian increased the solubility of the donor dopant Ti and the density of the ceramic by spark plasma sintering (SPS) to prepare a ZnO highly conductive ceramic with a conductivity of $2.3 \times 10^5 \text{ S} \cdot \text{m}^{-1}$ ^[29]. Yang Jing synthesized high-density ZnO ceramics by cold sintering process, and the electrical conductivity increased significantly from $5 \times 10^{-4} \text{ S} \cdot \text{cm}^{-1}$ to $16.4 \text{ S} \cdot \text{cm}^{-1}$ after heat treatment in Ar^[117]. Based on the simple process, reduced cost, and ease of mass industrial production, the traditional solid phase sintering method is the most common method for preparing ZnO conductive ceramics. The conductivity can also be improved through the exploration of this sintering process, such as sintering atmosphere, temperature, holding time and cooling rate. Yu Zhao found that the conductivity of Al-doped ZnO

increased from 10^{-5} to 10^3 S·cm⁻¹ in the sintering atmosphere from air to nitrogen and then to vacuum. Because sintering in a low oxygen partial pressure atmosphere promotes the substitution of Al for Zn and increases the concentration of interstitial Zn (Zn_i), then the rising carrier concentration increases the conductivity^[30]. Apart from the atmosphere, a suitably high sintering temperature can also contribute to the substitution of Al³⁺ at the Zn²⁺ site to reduce the resistivity of ZnO grains and grain boundaries^[129]. The holding time at the optimal sintering temperature will affect the structure and properties of ZnO ceramics. ZnO grains can't grow well into ceramics under short holding time; while a longer holding time will cause excessive growth of ceramics and lead to grain deformity, therefore the proper sintering holding time is also very important. The size of the grains, the content of the second phases, defects, and density can be controlled by the sintering holding time to adjust the electrical properties of ZnO ceramics^[130, 131]. Similarly, the cooling rate also affects the structure of ZnO ceramics, which in turn affects the electrical properties^[132].

In summary, the doping of N-type elements such as Al in ZnO ceramics can greatly increase the carrier concentration, which is the most important and efficient way to increase the electrical conductivity. In addition, a suitable preparation or sintering process also contributes to improving the electrical conductivity of ZnO ceramics by adjusting the composition and structure.

1.4 Reference

- [1] Desgreniers S. High-density phases of ZnO: Structural and compressive parameters[J]. *Physical Review B*, 1998, 58(21):14102.
- [2] Zhang Y, Ram M K, Stefanakos E K, et al. Synthesis, Characterization, and Applications of ZnO Nanowires[J]. *Journal of Nanomaterials*, 2012, 2012:1-22.
- [3] Klingshirn C. ZnO: material, physics and applications[J]. *Chemphyschem*, 2007, 8(6):782-803.

- [4] Ma Z, Ren F, Ming X, et al. Cu-Doped ZnO Electronic Structure and Optical Properties Studied by First-Principles Calculations and Experiments[J]. *Materials*, 2019, 12(1).
- [5] Mehrabian M, Azimirad R, Mirabbaszadeh K, et al. UV detecting properties of hydrothermal synthesized ZnO nanorods[J]. *Physica E*, 2011, 43(6): 1141-5.
- [6] 王振林, 李盛涛. 氧化锌压敏陶瓷制造及应用[M]: 科学出版社, 2009.
- [7] Pearton S. Recent progress in processing and properties of ZnO[J]. *Progress in Materials Science*, 2005, 50(3):293-340.
- [8] Liu W, Zhang L, Kong F, et al. Enhanced voltage gradient and energy absorption capability in ZnO varistor ceramics by using nano-sized ZnO powders[J]. *Journal of Alloys and Compounds*, 2020, 828:154252.
- [9] Shawuti S, Can M M, Gülgün M A, et al. Grain Size Dependent Comparison of ZnO and ZnGa₂O₄ Semiconductors by Impedance Spectrometry[J]. *Electrochimica Acta*, 2014, 145:132-8.
- [10] Ymanoğlu R, Bradbury W L, Olevsky E A, et al. Comparative evaluation of densification and grain size of ZnO powder compacts during microwave and pressureless spark plasma sintering[J]. *Advances in Applied Ceramics*, 2012, 111(7):422-6.
- [11] Sun Q, Li G, Tian T, et al. Controllable microstructure tailoring for regulating conductivity in Al-doped ZnO ceramics[J]. *Journal of the European Ceramic Society*, 2020, 40(2):349-54.
- [12] TASAKI S, Tatami J, Nakano H, et al. Fabrication of ZnO ceramics using ZnO/Al₂O₃ nanocomposite particles prepared by mechanical treatment[J]. *Journal of Ceramic Society Japan*, 2010, 118(1374):118-21.
- [13] Meyer B K, Sann J, Hofmann D M, et al. Shallow donors and acceptors in ZnO[J]. *Semiconductor Science and Technology*, 2005, 20(4):S62-S6.
- [14] Xu L, Zheng G, Xian F, et al. The morphological evolution of ZnO thin

- films by Sn ions doping and its influence on the surface energy and photocatalytic activity[J]. *Materials Chemistry and Physics*, 2019, 229: 215-25.
- [15] S. Bernik, N. Daneu, Recnik A. Inversion boundary induced grain growth in TiO₂ or Sb₂O₃ doped ZnO-based varistor ceramics[J]. *Journal of the European Ceramic Society*, 2004, 24:3703–8.
- [16] Zhaosheng Z, Zhenya L. TiO₂ and MgO doped ZnO conductive ceramics[J]. *Functional Materials*, 2009, 9(40):1455-60.
- [17] Kei-Ichiro Kobayashi, Osamu Wada, Masahiro Kobayashi, et al. Continuous existence of Bismuth at grain boundaries of Zinc Oxide varistor without intergranular phase[J]. *Journal of the American Ceramic Society*, 1998, 81(8):2071-76.
- [18] Brillson L J, Lu Y. ZnO Schottky barriers and Ohmic contacts[J]. *Journal of Applied Physics*, 2011, 109(12).
- [19] Tian J, Xu R, He H, et al. The nonlinear conductivity and mechanism of ZnO ceramic-epoxy composite material[J]. *Journal of Alloys and Compounds*, 2017, 723:1011-7.
- [20] G M W. Grain Boundaries in Engineering Materials [J]. *Journal of Vacuum Science and Technology*, 2006, 13(1):926-9.
- [21] Cai K, Müller E, Drašar C, et al. Preparation and thermoelectric properties of Al-doped ZnO ceramics[J]. *Materials Science and Engineering B*, 2003, 104(1-2):45-8.
- [22] Tian T, Cheng L, Zheng L, et al. Defect engineering for a markedly increased electrical conductivity and power factor in doped ZnO ceramic[J]. *Acta Materialia*, 2016, 119:136-44.
- [23] K P, K K. Effect of TiO₂ on high-temperature thermoelectric properties of ZnO[J]. *Journal of Alloys and Compounds*, 2007, 430:200-4.
- [24] Tsubota T, Ohtaki M, Eguchi K, et al. Thermoelectric properties of

- Al-doped ZnO as a promising oxide material for high temperature thermoelectric conversion[J]. *Journal of Materials Chemistry* 1997, 7(1):85–90.
- [25] Sun Q, Li G, Tian T, et al. Co-doping effects of (Al, Ti, Mg) on the microstructure and electrical behavior of ZnO based ceramics[J]. *Journal of the American Ceramic Society*, 2020, 103:3194–204.
- [26] Chen M, Liu Q, Zhu J, et al. Effect of ZnAl₂O₄ content on the microstructure and electrical properties of ZnO-based compound conductive ceramics[J]. *Journal of Alloys and Compounds*, 2018,750: 213-9.
- [27] 田甜. 基于晶界肖特基势垒调控的 ZnO 陶瓷的电学性能及其结构性能关系研究: 中国科学院上海硅酸盐研究所; 2017.
- [28] Han J, Mantas P Q, Senos A M R. Densification and grain growth of Al-doped ZnO[J]. *Journal of Materials Research*, 2001, 16(2):459-67.
- [29] T T, L C, J X, et al. Effects of sintering on the microstructure and electrical properties of ZnO-based thermoelectric materials[J]. *Materials and Design*, 2017, 132:479-85.
- [30] Zhao Y, Wang J, Huxtable S, et al. Role of Sintering Atmosphere and Synthesis Parameters on Electrical Conductivity of ZnO[J]. *Energy Harvesting and Systems*, 2015, 2(1-2).
- [31] LI S, LI J, ALIM M A. Structural Origin of Dimensional Effect in ZnO Varistors[J]. *Journal of Electroceramics*, 2003, 11:119-24.
- [32] 徐业彬, 季幼章. ZnO-Al₂O₃-MgO 陶瓷性能研究[J]. *无机材料学报*, 1994, 9(4):497-501
- [33] GUPTA T K. Application of Zinc-Oxide Varistors[J]. *Journal of the American Ceramic Society*, 1990, 73(7):1817-40.
- [34] Masteghin M G, Orlandi M O. Grain-Boundary Resistance and Nonlinear Coefficient Correlation for SnO₂-Based Varistors[J]. *Materials Research*,

2016, 19(6):1286-91.

- [35] Filho F M, Simões A Z, Ries A, et al. Nonlinear electrical behaviour of the Cr_2O_3 , ZnO, CoO and Ta_2O_5 -doped SnO_2 varistors[J]. *Ceramics International*, 2006, 32(3):283-9.
- [36] Wang Y, Peng Z, Wang Q, et al. Highly nonlinear varistors from oxygen-deficient zinc oxide thin films by hot-dipping in Bi_2O_3 : Influence of temperature[J]. *Applied Surface Science*, 2016, 390:92-9.
- [37] 徐业彬, 季幼章, 王士良. ZnO-MgO- Al_2O_3 陶瓷性能研究 [J]. *无机材料学报*, 1994, 4(1994).
- [38] Eda K. Destruction mechanism of ZnO varistors due to high currents[J]. *Journal of Applied Physics*, 1984, 56(10):2948-55.
- [39] P. Díaz-Chao, F. Giovannelli, O. Lebedev. Textured Al-doped ZnO ceramics with isotropic grains[J]. *Journal of the European Ceramic Society*, 2014, 34(16):4247-56.
- [40] Vempati S, Mitra J, Dawson P. One-step synthesis of ZnO nanosheets: a blue-white fluorophore[J]. *Nanoscale Research Letters*, 2012, 7(1):470.
- [41] HAGEMARK K I. Defect Structure of Zn-Doped ZnO[J]. *Journal of Solid State Chemistry*, 1976, 16:293-9.
- [42] HOFFMANN K, HAHN D. Electron Spin Resonance of Lattice Defects in Zinc Oxide[J]. *physica status solidi (a)*, 1974, 24:637.
- [43] Oba F, Choi M, Togo A, et al. Point defects in ZnO: an approach from first principles[J]. *Science and Technology of Advanced Materials*, 2011, 12(3):034302.
- [44] McCluskey M D, Jokela S J. Defects in ZnO[J]. *Journal of Applied Physics*, 2009, 106(7):071101.
- [45] Lany S, Zunger A. Assessment of correction methods for the band-gap problem and for finite-size effects in supercell defect calculations: Case

- studies for ZnO and GaAs[J]. *Physical Review B*, 2008, 78(23).
- [46] Janotti A, Van de Walle C G. Native point defects in ZnO[J]. *Physical Review B*, 2007, 76(16).
- [47] Liu L, Mei Z, Tang A, et al. Oxygen vacancies: The origin of n-type conductivity in ZnO[J]. *Physical Review B*, 2016, 93(23).
- [48] Bandopadhyay K, Mitra J. Zn interstitials and O vacancies responsible for n-type ZnO: what do the emission spectra reveal[J]. *RSC Advances*, 2015, 5(30):23540-7.
- [49] McCluskey M D, Jokela S J, Hlaing Oo W M. Hydrogen in bulk and nanoscale ZnO[J]. *Physica B*, 2006, 376-377:690-3.
- [50] Nuno Neves, Raquel Barros, Elsa Antunes, et al. Aluminum doped zinc oxide sputtering targets obtained from nanostructured powders: Processing and application[J]. *Journal of the European Ceramic Society*, 2012, 32(16):4381-91.
- [51] Zhang Z Z, Wei Z P, Lu Y M, et al. p-Type ZnO on sapphire by using O₂-N₂ co-activating and fabrication of ZnO LED[J]. *Journal of Crystal Growth*, 2007, 301-302:362-5.
- [52] Meyer B K, Sann J, Zeuner A. Lithium and sodium acceptors in ZnO[J]. *Superlattices and Microstructures*, 2005, 38(4-6):344-8.
- [53] Li J, Liu Y, Mei Z, et al. Limitation of Na-H codoping in achieving device-quality p-type ZnO[J]. *Materials Science in Semiconductor Processing*, 2017, 69:28-31.
- [54] Yan Y, Zhang S B, Pantelides S T. Control of doping by impurity chemical potentials: predictions for p-type ZnO[J]. *Physical review letters*, 2001, 86(25):5723-6.
- [55] Orlinskii S B, Schmidt J, Baranov P G, et al. Probing the wave function of shallow Li and Na donors in ZnO nanoparticles[J]. *Physical review letters*, 2004, 92(4):047603.

- [56] Lu J, Zhang Y, Ye Z, et al. Low-resistivity, stable p-type ZnO thin films realized using a Li-N dual-acceptor doping method[J]. Applied Physics Letters, 2006, 88(22).
- [57] Shoji M T S, Shirakawa S. Effect of Al₂O₃, MgO and SiO₂ additives on electrical resistivity and sintering property of ZnO ceramics[J]. Journal of the Ceramic Society of Japan 2000, 108(1):89-93
- [58] Makino T, Segawa Y, Tsukazaki A, et al. Electron transport in ZnO thin films[J]. Applied Physics Letters, 2005, 87(2).
- [59] Lee Y J, Kim H H, Lee Y J, et al. Corrigendum: Electron transport phenomena at the interface of Al electrode and heavily doped degenerate ZnO nanoparticles in quantum dot light emitting diode[J]. Nanotechnology, 2019, 30(36).
- [60] Hamza Taha M K, Boisron O, Canut B, et al. Control of the compensating defects in Al-doped and Ga-doped ZnO nanocrystals for MIR plasmonics[J]. RSC Advances, 2017, 7(46):28677-83.
- [61] KOUMOTO K, AOKI N, KITAORI N, et al. Enhancement of Electrical Conduction in ZnO by CoO Doping[J]. Communications of the American Ceramic Society, 1982:93-4.
- [62] Jian Feng Z, Hai Bo Yang, Fen Wang. Effect of TiO₂ addition on the microstructure and electrical properties of ZnO-based linear resistance ceramics[J]. Journal of Materials Science: Materials in Electronics, 2012, 23:445–50.
- [63] Wang F, Seo J H, Li Z, et al. Cl-doped ZnO nanowires with metallic conductivity and their application for high-performance photoelectrochemical electrodes[J]. ACS Appl Mater Interfaces, 2014,6(2): 1288-93.
- [64] Jiamprasertboon A, Dixon S C, Sathasivam S, et al. Low-Cost One-Step Fabrication of Highly Conductive ZnO:Cl Transparent Thin Films with Tunable Photocatalytic Properties via Aerosol-Assisted Chemical Vapor

- Deposition[J]. ACS Appl Electron Mater, 2019, 1(8):1408-17.
- [65] Colibaba G V. Sintering highly conductive ZnO:HCl ceramics by means of chemical vapor transport reactions[J]. Ceramics International, 2019, 45(13):15843-8.
- [66] Kelchtermans A, Adriaensens P, Slocombe D, et al. Increasing the Solubility Limit for Tetrahedral Aluminium in ZnO:Al Nanorods by Variation in Synthesis Parameters[J]. Journal of Nanomaterials, 2015, 2015:1-8.
- [67] Serier H, Gaudon M, Ménétrier M. Al-doped ZnO powdered materials: Al solubility limit and IR absorption properties[J]. Solid State Sciences, 2009, 11(7):1192-7.
- [68] Tian T, Cheng L H, Zheng L Y, et al. Defect engineering for a markedly increased electrical conductivity and power factor in doped ZnO ceramic[J]. Acta Materialia, 2016, 119:136-44.
- [69] Zhang D, Zhang B, Ye D, et al. Enhanced Al/Ni co-doping and power factor in textured ZnO thermoelectric ceramics prepared by hydrothermal synthesis and spark plasma sintering[J]. Journal of Alloys and Compounds, 2016, 656:784-92.
- [70] Cheng H, Xu X J, Hng H H, et al. Characterization of Al-doped ZnO thermoelectric materials prepared by RF plasma powder processing and hot press sintering[J]. Ceramics International, 2009, 35(8):3067-72.
- [71] Wang X-m, Bai X, Duan H-y, et al. Preparation of Al-doped ZnO sputter target by hot pressing[J]. Transactions of Nonferrous Metals Society of China, 2011, 21(7):1550-6.
- [72] Lavrov E V. Infrared absorption spectroscopy of hydrogen-related defects in ZnO[J]. Physica B, 2003, 340-342:195-200.
- [73] Cao Y, Luo J, Huang W, et al. Probing surface defects of ZnO using formaldehyde[J]. The Journal of Chemical Physics, 2020, 152(7):074714.

- [74] Tamil Many K. Thandavan, Siti Meriam Abdul Gani, Chiow San Wong, et al. Enhanced photoluminescence and Raman properties of Al-Doped ZnO nanostructures prepared using thermal chemical vapor deposition of methanol assisted with heated brass[J]. PloS one, 2015, 10(3):1-18.
- [75] Mondal A, Pal S, Sarkar A, et al. Raman spectroscopic analysis on Li, N and (Li,N) implanted ZnO[J]. Materials Science in Semiconductor Processing, 2018, 80:111-7.
- [76] Jang M S, Ryu M K, Yoon M H, et al. A study on the Raman spectra of Al-doped and Ga-doped ZnO ceramics[J]. Current Applied Physics, 2009, 9:651-7.
- [77] Isik M, Gasanly N M. Thermoluminescence properties of Al doped ZnO nanoparticles[J]. Ceramics International, 2018, 44(12):13929-33.
- [78] Commandeur D, Brown G, Hills E, et al. Defect-Rich ZnO Nanorod Arrays for Efficient Solar Water Splitting[J]. ACS Applied Nano Materials, 2019, 2(3):1570-8.
- [79] Xue Z, Cheng Z, Xu J, et al. Controllable Evolution of Dual Defect Zn and VO Associate-Rich ZnO Nanodishes with (0001) Exposed Facet and Its Multiple Sensitization Effect for Ethanol Detection[J]. ACS Appl Mater Interfaces, 2017, 9(47):41559-67.
- [80] Sun Q, Tian T, Zheng L, et al. Electronic active defects and local order in doped ZnO ceramics inferred from EPR and ²⁷Al NMR investigations[J]. Journal of the European Ceramic Society, 2019, 39(10):3070-6.
- [81] Orlinskii S B, Schmidt J, Baranov P G, et al. Identification of shallow Al donors in Al-doped ZnO nanocrystals: EPR and ENDOR spectroscopy[J]. Physical Review B, 2008, 77:115334.
- [82] Garces N Y, Giles N C, Halliburton L E, et al. Production of nitrogen acceptors in ZnO by thermal annealing[J]. Applied Physics Letters, 2002, 80(8):1334-6.

- [83] Gonzalez C, Block D, Cox R T, et al. Magnetic resonance studies of shallow donors in Zinc Oxide[J]. *Journal of Crystal Growth*, 1982, 59:357-62.
- [84] A J R, MK K, H N, et al. EPR, thermo and photoluminescence properties of ZnO nanopowders[J]. *Spectrochim Acta A Mol Biomol Spectrosc*, 2011, 81(1):59-63.
- [85] Krasil'nikov V N, Dyachkova T V, Tyutyunnik A P, et al. Magnetic and optical properties as well as EPR studies of polycrystalline ZnO synthesized from different precursors[J]. *Materials Research Bulletin*, 2018, 97:553-9.
- [86] Wang J, Chen R, Xiang L, et al. Synthesis, properties and applications of ZnO nanomaterials with oxygen vacancies: A review[J]. *Ceramics International*, 2018, 44(7):7357-77.
- [87] Kao H-M, Wu R-R, Chen T-Y, et al. Probing the formation process of aluminium hydroxide nanoparticles prepared by laser ablation with ^{27}Al NMR spectroscopy[J]. *Journal of Materials Chemistry*, 2000, 10(12): 2802-4.
- [88] Choi M, Matsunaga K, Oba F, et al. ^{27}Al NMR Chemical Shifts in Oxide Crystals: A First-Principles Study[J]. *The Journal of Physical Chemistry C*, 2009, 113:3869-73.
- [89] Huang Y, Sutrisno A. Recent Advances in Solid-State ^{67}Zn NMR Studies. *Annual Reports on NMR Spectroscopy*, 2014. p. 1-46.
- [90] Momot A, Amini M N, Reekmans G, et al. A novel explanation for the increased conductivity in annealed Al-doped ZnO: an insight into migration of aluminum and displacement of zinc[J]. *Physical Chemistry Chemical Physics*, 2017, 19(40):27866-77.
- [91] 季幼章, 徐业彬, 袁方利. 一种新型电阻元件—氧化锌陶瓷电阻器[J]. *电子元器件应用*, 2001, 3(6):14-8

- [92] 彭济南, 叶德平, 陈敬. 氧化锌线性电阻中性点接地电阻器[J]. 电瓷避雷器, 2001, 6:16-21
- [93] 储登. 氧化锌电阻在发电机灭磁中的应用[J]. 江苏电器, 2008, 3:44-6.
- [94] 李盛涛, 刘辅宜, 徐传骧. 新型 ZnO 陶瓷线性电阻材料[J]. 功能材料, 1996, 27(1):55-60.
- [95] 张伟强, 杨小平, 李建英. 浪涌保护器的发展动向[J]. 电瓷避雷器, 2001, 4:29-33.
- [96] 李盛涛, 张炜. ZnO 线性电阻陶瓷体与烧银电极的电接触[J]. 功能材料, 1998, 29(1):85-8.
- [97] 范积伟, 夏良, 张小立. 新型压敏陶瓷材料的研究与进展[J]. 功能材料信息, 2010, 7(3):21-5.
- [98] Xu Z, Bai H, Ma S, et al. Effect of a Bi–Cr–O synthetic multi-phase on the microstructure and electrical properties of ZnO–Bi₂O₃ varistor ceramics[J]. *Ceramics International*, 2016, 42(13):14350-4.
- [99] Levinson L, Philipp H R. Zinc Oxide Varistors - A Review[J]. *American Ceramic Society Bulletin*, 1986, 65(4):639-46.
- [100] 范强, 杨建会, 邓迟, et al. 氧化锌基热电材料研究进展[J]. 乐山师范学院学报, 2015, 30(12):21-5.
- [101] Mohammed M, Izman S, Alias M N, et al. A review of thermoelectric ZnO nanostructured ceramics for energy recovery[J]. *International Journal of Engineering & Technology*, 2018, 7(2.29).
- [102] Qu X, Wang W, Lv S, et al. Thermoelectric properties and electronic structure of Al-doped ZnO[J]. *Solid State Communications*, 2011, 151(4):332-6.
- [103] Radingoana P M, Guillemet-Fritsch S, Noudem J, et al. Thermoelectric properties of ZnO ceramics densified through spark plasma sintering[J].

- Ceramics International, 2020, 46(4):5229-38.
- [104] Fukumura T, Jin Z, Ohtomo A, et al. An oxide-diluted magnetic semiconductor: Mn-doped ZnO[J]. Applied Physics Letters, 1999, 75(21):3366-8.
- [105] Yang Z. A perspective of recent progress in ZnO diluted magnetic semiconductors[J]. Applied Physics A, 2013, 112(2):241-54.
- [106] Jun S T, Choi G M. CO gas-sensing properties of ZnO/CuO contact ceramics[J]. Sensors and Actuators B, 1994, 17:175-8.
- [107] Rao G T, Rao D T. Gas sensitivity of ZnO based thick film sensor to NH₃ temperature[J]. Sensors and Actuators B: Chemical, 1999, 55:166-9.
- [108] Wang X-H, Ding Y-F, Zhang J, et al. Humidity sensitive properties of ZnO nanotetrapods investigated by a quartz crystal microbalance[J]. Sensors and Actuators B: Chemical, 2006, 115(1):421-7.
- [109] Park K, Lee J K. Mn-Ni-Co-Cu-Zn-O NTC thermistors with high thermal stability for low resistance applications[J]. Scripta Materialia, 2007, 57(4):329-32.
- [110] Sun X, Zhang H, Liu Y, et al. Characterization of new negative temperature coefficient thermistors based on Zn-Ni-O system[J]. Journal of Advanced Ceramics, 2016, 5(4):329-36.
- [111] Yamny S E, Rafea M A. Preparation and Characterization of ZnO: In Transparent Conductor by Low Cost Dip Coating Technique[J]. Journal of Modern Physics, 2012, 03(09):1060-9.
- [112] Jang J S, Kim J, Ghorpade U, et al. Comparison study of ZnO-based quaternary TCO materials for photovoltaic application[J]. Journal of Alloys and Compounds, 2019, 793:499-504.
- [113] 杨胜辉. ZnO 陶瓷释能电阻材料的研究. 成都: 电子科技大学; 2014.
- [114] Zhu J, Wang J, Zhou Y, et al. Major effects on microstructure and

- electrical properties of ZnO-based linear resistance ceramics with MgO changes[J]. *Journal of Materials Science: Materials in Electronics*, 2014, 25:2273-8.
- [115] Sharma V, Kumar P, Kumar A, et al. High-performance radiation stable ZnO/Ag/ZnO multilayer transparent conductive electrode[J]. *Solar Energy Materials and Solar Cells*, 2017, 169:122-31.
- [116] Ellmer K, Klein A. ZnO and Its Applications. In: Ellmer K, Klein A, Rech B, editors. *Transparent Conductive Zinc Oxide*: Springer; 2008. p. 1-27.
- [117] Jing Y, Luo N, Wu S, et al. Remarkably improved electrical conductivity of ZnO ceramics by cold sintering and post-heat-treatment[J]. *Ceramics International*, 2018, 44(16):20570-4.
- [118] Minami T, Nanto H, Takata S. Highly Conductive and Transparent Aluminum Doped Zinc Oxide Thin Films Prepared by RF Magnetron Sputtering[J]. *Japanese Journal of Applied Physics*, 1984, 23(5):280-2.
- [119] Ohtaki M, Tsubota T, Eguchi K, et al. High-temperature thermoelectric properties of $(\text{Zn}_{1-x}\text{Al}_x)\text{O}$ [J]. *Journal of Applied Physics*, 1996, 79(3): 1816-8.
- [120] Dulin F H, Rase D E. Phase Equilibria in the System ZnO-TiO₂[J]. *Journal of the American Ceramic Society*, 1960, 43:125-31.
- [121] Jung K-H, Choi S-M, Lim C-H, et al. Phase analysis and thermoelectric properties of $\text{Zn}_{1-x}\text{M}_x\text{O}$ (M= Al, Ga) samples[J]. *Surface and Interface Analysis*, 2012, 44(11-12):1507-10.
- [122] Liang X, Clarke D R. Relation between thermoelectric properties and phase equilibria in the ZnO-In₂O₃ binary system[J]. *Acta Materialia*, 2014, 63:191-201.
- [123] Park K, Seong J K, Kim G H. NiO added $\text{Zn}_{1-x}\text{Ni}_x\text{O}$ ($0 \leq x \leq 0.05$) for thermoelectric power generation[J]. *Journal of Alloys and Compounds*, 2009, 473(1-2):423-7.

- [124] Park K, Seong J K, Nahm S. Improvement of thermoelectric properties with the addition of Sb to ZnO[J]. *Journal of Alloys and Compounds*, 2008, 455(1-2):331-5.
- [125] Ellmer K, Bikowski A. Intrinsic and extrinsic doping of ZnO and ZnO alloys[J]. *Journal of Physics D: Applied Physics*, 2016, 49(41).
- [126] Ning J L, Jiang D M, Kim K H, et al. Influence of texture on electrical properties of ZnO ceramics prepared by extrusion and spark plasma sintering[J]. *Ceramics International*, 2007, 33(1):107-14.
- [127] Kaga H, Kinemuchi Y, Yilmaz H, et al. Orientation dependence of transport property and microstructural characterization of Al-doped ZnO ceramics[J]. *Acta Materialia*, 2007, 55(14):4753-7.
- [128] Fujishiro Y, Miyata M, Awano M, et al. Effect of Microstructural Control on Thermoelectric Properties of Hot-Pressed Aluminum-Doped Zinc Oxide[J]. *Journal of the American Ceramic Society*, 2003, 86:2063–66.
- [129] Zhao Y, Kumar A, Khodaparast G A, et al. Sintering Temperature - Dependent Chemical Defects and the Effect on the Electrical Resistivity of Thermoelectric ZnO[J]. *Energy Harvesting and Systems*, 2014, 1:1-2.
- [130] Tak S K, Shekhwat M S, Mangal R. Electrical Property of Conventionally Sintered ZnO[J]. *International Journal of Modern Physics*, 2013, 22:501-10.
- [131] Liu S, Liu J, Jiang W, et al. Aluminum- and boron-co-doped ZnO ceramics: structural, morphological and electrical characterization[J]. *Applied Physics A: Materials Science and Processing*, 2016, 122(10).
- [132] Hongyu L, Hui K, Dongmei J, et al. Effects of cooling rate on the microstructure and electrical properties of Dy₂O₃-doped ZnO-based varistor ceramics[J]. *Rare Metals*, 2007, 29(1):39.

Chapter 2

Experimental procedures and Instrumentation

The chapter introduces the experimental methodology and techniques developed for the synthesis of the ZnO-based ceramics, their treatments and the investigations of their related physical and chemical properties. The characterization methods which were used for this thesis work concern the structural investigations by X-ray diffraction (XRD) and Raman spectrometry, the morphology and microstructures by scanning (SEM) and transmission (TEM) electron microscopy, the electrical and dielectric measurements and magnetic resonance techniques such as electron paramagnetic resonance (EPR) and Solid state nuclear magnetic resonance (NMR). The main techniques and experimental details are outlined in the forthcoming sections.

2.1 Processing of doped ZnO based materials

2.1.1 Experimental flow

The experimental methodology of the thesis work is shown in Figure 2.1. First, the chemical compositions of ZnO-based ceramics are defined as function of the targeted properties defined as objective of our studies. Thus, raw materials in defined stoichiometric ratios and sintering methods under different atmospheres were used to prepare the required ceramic samples. The fabrication processes are followed by characterizations of the structure, morphology and electrical properties. After analyzing the performance indicators, the ceramic formula and sintering parameters were optimized and modified. The modified parameters are: composition of the solid solutions, doping elements and the conditions on the sintering atmospheres.

- (5) Granulation: The powder is granulated after passing through a 40-mesh sieve and 10 wt.% PVA solution (concentration: 5 wt.%) is added as a binder and ground for half an hour. After passing through the 40-mesh screen, the powder is pressed into one bulk. After standing for 24 hours, the bulk is broken apart to obtain granulated powder. After two sieving, powder particles with good fluidity are obtained.
- (6) Tableting: Weigh an appropriate amount of granulated powder into a mold, and press into a green pellet with a thickness of 2 mm and a diameter of 12 mm under a pressure of 200 Mpa.
- (7) Debinding: The ceramic green pellets are arranged in a muffle furnace and kept at 500 °C for 6 hours to remove the binder. In order to prevent cracks in the green pellet, the heating rate is 1 °C/min.
- (8) Sintering: The green pellets after debinding are placed in a muffle furnace, held at 1200 °C for 2 hours, and sintered in an atmosphere of air, nitrogen, nitrogen and carbon monoxide, respectively, to obtain a dense ceramic sheet.

2. Spark plasma sintering

Spark plasma sintering (SPS), also known as field-assisted sintering technology (FAST) or pulsed electric current sintering (PECS), is a fast and efficient new sintering method with high heating rate, short sintering time and high density of sintered ceramics. The specific preparation process uses the powder preparation method as described above (1)-(4) for the traditional solid-phase synthesis process, but the subsequent sintering steps are different. An appropriate amount of the mixed powder is weighed into a graphite mold with a diameter of 15 mm, and then it is placed in a spark plasma sintering furnace. In a vacuum atmosphere, the pressure is applied to 65 MPa, and the temperature is raised to 1000 °C for 5 minutes. The pressure is released after sintering, and the SPS sintered ceramic sample is taken out after the temperature drops to the room temperature.

The ceramic pellets prepared by the above two preparation and sintering methods were then subjected to grinding or polishing, cutting, silver plating or wire welding to perform subsequent characterization studies.

2.2 Characterization techniques

2.2.1 Electrical measurements (Four-point method)

The resistance measurement is usually performed by the two-points method, that is, two leads are drawn on both sides of the sample, and the current source with the voltmeter or the voltage source with the ammeter are connected at the same time. Due to the existence of lead resistance and contact resistance, this method is only applicable to the measurement of large resistance samples. For samples with small resistance values, the lead resistance and contact resistance cannot be ignored compared with the sample resistance. Also, a large error is committed with the two-point method, which has a great impact on the actual measured resistance value. Therefore, the four-point method is generally used to test the resistance value of the small resisting sample. The main difference between these two test methods (two-points and four-points) lies in the number of leads from the sample. As shown in Figure 2.2 (a), in the two-points method, two leads from the side of the sample are connected to the ammeter and voltmeter simultaneously. Figure 2.2 (b) shows the four-terminal method where two leads from the two ends of the sample are connected to the ammeter, and two leads from the upper surface are connected to the voltmeter. The principle of both measurement methods follows Ohm's law, and the conductivity test formula is:

$$\sigma = \frac{I}{V} \times \frac{a \times b}{l} \quad (2.1)$$

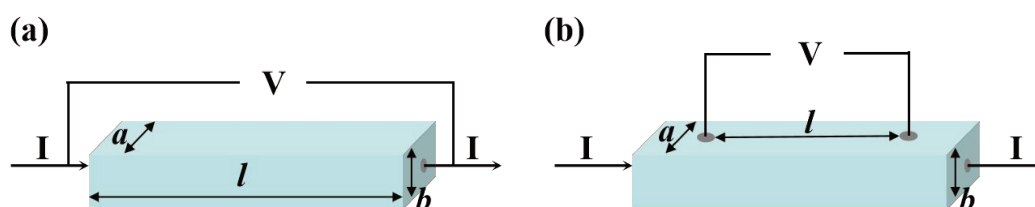


Figure 2.2 Schematic comparison of (a) two-point and (b) four-point method

The investigated ceramics in this thesis are highly conductive samples, so the

four-terminal method is used for the resistance measurements. According to the four-terminal test principle, two methods are used to measure the conductivity.

The first method is to measure the electrical conductivity through a self-assembled resistance test equipment, which mainly includes Keithley 6221 current source and Keithley 2182A two-channel nanovoltmeter. The operation method is based on a ceramic pellet with a diameter of 12 mm which is cut into small cuboid with a width of “a” and a height of “b”. The copper wire electrodes are welded at two points on the surface and two points at both ends of the cuboid to connect the voltmeter and the current source, respectively. The distance “l” between the two electrode points in the middle is measured by a vernier caliper. For the measurements, Keithley 6221 current source provides a pulse current (I) with a pulse width of 0.2 ms and a delay of 0.1 ms. The voltage (V) is measured using a 2182A nanovoltmeter. The measurement diagram is shown in Figure 2.3. Based on the measured corresponding voltage, current, and size of the ceramic cuboid, the conductivity (σ) can be calculated.

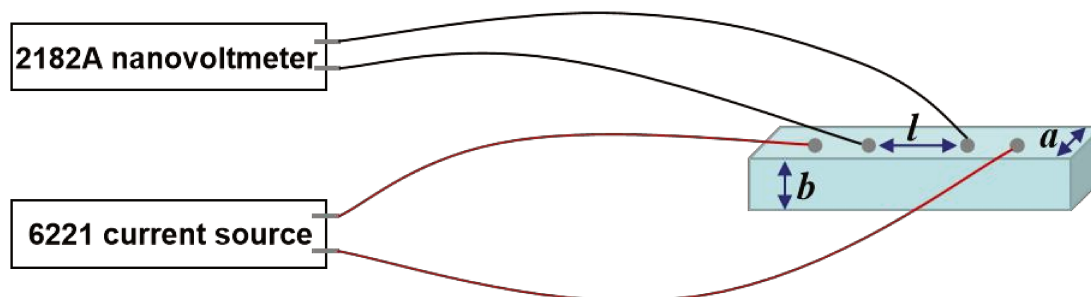


Figure 2.3 Schematic diagram of self-assembly test resistance measurement equipment

The second method is to use the Pro4 four-points probe test system of Lucas Labs, as shown in Figure 2.4 (a). The test system mainly includes Keithley 2400, Pro4 probe station and Pro4 software. The key components of the Pro4 probe station is the four-point probe head composed of four tungsten carbide plastic steel probes arranged in a row and the distance between the probes is “s”, as shown in Figure 2.4 (b). Among them, the two probes in the middle are used to measure the voltage while the

two probes on both sides are used for the current.

The operation process consists in first introducing the data related to the shape and thickness of the sample in the Pro4 software. The smooth ceramic pellet is placed to be tested on the sample stage, and adjust the four-points probe head to connect the sample to the setup with a computer monitoring. After running the test, the system selects the appropriate current according to the conductive ability of the sample, and then measures the corresponding voltage. The test result leads to the resistivity value and then the conductivity. The same operation is repeated six times to evaluate the conductivity “ σ ” of the sample and the related measurement errors.

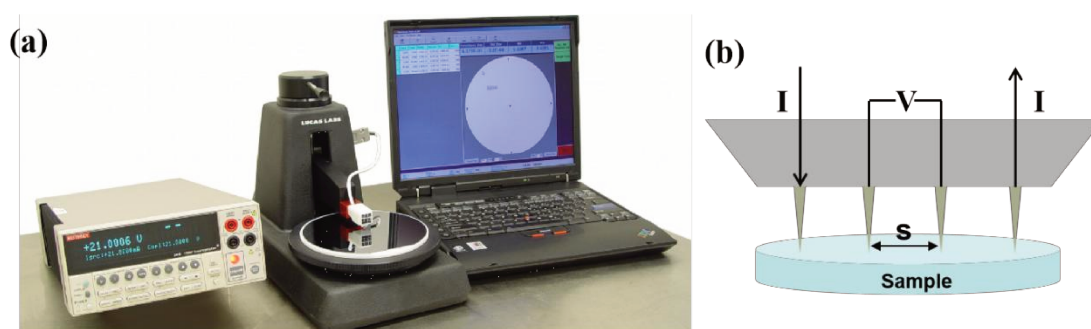


Figure 2.4 (a) Pro4 four-point probe test system, (b) Four probe head

The temperature coefficient of resistance (TCR) is calculated based on the relative change in the resistance with the sample temperature. Based on the first test method, the sample is placed in a thermostat to ensure measurements in the temperature range $-50\text{ }^{\circ}\text{C}$ to $150\text{ }^{\circ}\text{C}$. The temperature coefficient of resistance (TCR) of the sample can be calculated by the following equation 2.2.

$$\text{TCR} = \frac{R_2 - R_1}{R_1(T_2 - T_1)} \times 10^{-6} \quad (2.2)$$

Among them, R_1 is the resistance at room temperature (T_1), and R_2 is the resistance after heating up to T_2 . The usually used unit of TCR is “ppm / $^{\circ}\text{C}$ ”.

2.2.2 Physical Property Measurement System (PPMS)

The carrier concentration and mobility of the experimental samples were performed by the physical property measurement system (PPMS-9) of Quantum Design Company (US). The instrument can measure the electrical, thermal, magnetic properties of materials leading to the electrical resistivity, Hall coefficient, thermal conductivity, specific heat, Seebeck coefficient, magnetic susceptibility, and hysteresis loop, etc. As this thesis work focus on the conductivity of ceramic samples, the carrier concentration and mobility are the direct factors required from our measurements. Therefore, this work mainly uses the PPMS-9 instrument for Hall effect characterizations. Then, the carrier concentration and mobility of the sample can be evaluated.

The Hall effect mainly reflects the deflection of the moving charged particles (electrons or holes) by the Lorentz force due to the magnetic field. The induced deflection caused by the magnetic field on the charged particles in the ceramic body creates the Hall electric field (E_H). According to different types of charged particles, Hall electric fields in different directions are generated. A schematic diagram of this process is shown in Figure 2.5.

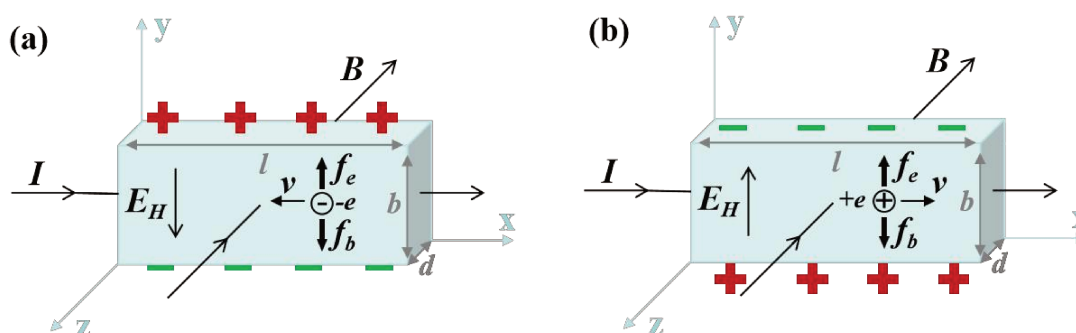


Figure 2.5 Schematic diagram of the Hall effect principle (a) Carriers are electrons (N-type) (b) Carriers are holes (P-type)

The dimensions of the sample consist in the width “b” and the thickness “d”. When the accumulated charge on both sides of the sample reaches a dynamic equilibrium, considering a carrier with a concentration of “n”, the electric field force eE_H compensates the Lorentz force evB . The potential difference between the upper and lower surfaces V_H is given by the following equation 2.3.

$$eE_H = e \frac{V_H}{b} = evB \quad (2.3)$$

The current generated when the carrier moves is:

$$I = nevbd \quad (2.4)$$

The following equation 2.5 is drawn from the above two equations:

$$V_H = \frac{1}{ne} \cdot \frac{IB}{d} = R_H \frac{IB}{d} \quad (2.5)$$

This leads to the equation 2.6,

$$\frac{V_H d}{I} = R_H B \quad (2.6)$$

Among them, $\frac{V_H d}{I}$ represents the Hall resistivity, which can be determined by the PPMS instrument. The proportionality coefficient R_H is a Hall coefficient and can be used to calculate the carrier concentration and mobility of the material. According to the Hall resistance measured by the PPMS instrument in the magnetic field strength of the magnetic field (up to 1 Tesla), a graph is plotted using these two parameters. The magnetic field strength is taken as the abscissa, the Hall resistivity is taken as the ordinate, and the slope obtained by the fitting is the Hall coefficient R_H . The carrier concentration (n) and mobility (μ) can be calculated according to the following equation 2.7 and equation 2.8.

$$R_H = \frac{1}{ne} \quad (2.7)$$

$$\sigma = ne\mu \quad (2.8)$$

2.2.3 Electron Microscopy (SEM and TEM)

When an electron beam enters a solid material, it interacts with its constitutive elements (atoms, molecules). These interactions include mainly: scattering of incident electrons, excitation of the solid by the incident electrons, and propagation of excited electrons in the solid. As shown in Figure 2.6, it is mainly presented in the form of

secondary electrons, backscattered electrons, characteristic X-rays, Auger electrons, transmitted electrons and so on. Secondary electrons are extra-nuclear electrons that are bombarded by the incident electron beam on the surface of the sample. They are generally emitted in the depth range of 5 nm to 50 nm on the surface of the sample and are very sensitive to the surface morphology. Therefore, secondary electron imaging of scanning electron microscope is commonly used to observe the surface micro-morphology of samples as it was used in the present thesis. Backscattered electrons are a part of the incident electrons reflected by the sample, including elastic backscattered electrons and inelastic backscattered electrons, mainly from the surface of the sample in the range of 100 nm to 1000 nm. Backscattered electron images are mainly derived from elastic backscattered electrons, and their yield is proportional to the atomic number. Therefore, in addition to morphological analysis, they can also be used qualitatively for the composition analysis based on the difference in the contrast of the atomic number of different atoms. The inner electrons of the sample are excited by the incident electrons or are ionized to form atoms in a higher energy excited states. At this time, the outer electrons transit to the inner layer to fill the vacancies and generate X-rays. According to the characteristic wavelength detected by the X-ray detector, the corresponding elements in the analyzed micro-regions can be determined, which is the principle of the X-ray energy spectrometer. For samples with a thickness less than the penetration depth, the electrons emitted by the incident electron penetrating sample from the other surface are transmitted electrons. The transmission electron microscopy depends mainly on the thickness, chemical composition and crystal structure of the analyzed micro-nano regions. The transmission electron microscope has the advantage of a high resolution, and can directly observe atomic images, so it can clearly observe the grain boundary and lattice structure of ceramics.

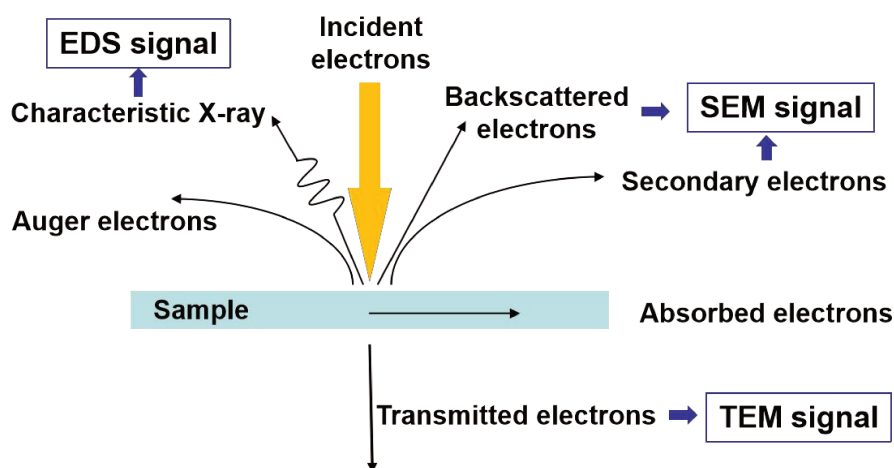


Figure 2.6 Schematic diagram of material-electron interaction

In this research work, the morphology and structure of the samples are analyzed using a scanning electron microscope (SEM, JEOL JSM 6510 LV, Japan) equipped with an X-ray spectrometer (EDS, X-MaxN, Oxford, UK) as shown in Figure 2.7. The used transmission electron microscope (TEM, JEOL 2100 HR) is shown in Figure 2.8 for the observations and analyses which provide relevant information for the study of the relationship between the performances and the microstructures of the samples.



Figure 2.7 Scanning electron microscope



Figure 2.8 Transmission electron microscope

SEM investigations were performed on polished and hot-etched surfaces of the samples to obtain clear and complete morphological images. The purpose of polishing is to obtain a fresh and clean ceramic surface while thermal corrosion allows to show the grain morphology on the ceramic surface. Compared with grains, grain boundaries with more defects are more likely to be corroded. The processing consists in mechanical polishing the sintered pellets and then the sample is placed in a muffle furnace and heated to a temperature close to the sintering temperature ($1100\text{ }^{\circ}\text{C} \sim 1150\text{ }^{\circ}\text{C}$) using an extremely fast heating rate ($10\text{ }^{\circ}\text{C}/\text{min}$). After holding for 10 minutes and cooling to room temperature with the furnace, the sample is taken out and cleaned ultrasonically, then used for SEM observations.

By an acceleration voltage during the test about 10 kV, the SEM images illustrate the surface morphology of the samples to obtain the crystal shape, size, porosity and composition of the ceramics.

The ground and ion-etched ceramic samples are placed on a copper mesh for TEM observations. High-resolution images were obtained for the ceramic grains and grain boundaries at the atomic level. Valuable information can be obtained on the sample-related structural defects, grain boundary phases, unit cell parameters, and chemical composition.

2.2.4 X-ray Diffraction

X-ray diffractometer is a commonly used for structural investigations. It is mainly composed by an X-ray source, goniometer or sample holder, X-ray intensity measurement system with a computer controlling the diffractometer, data acquisition and processing. The crystal structure of the investigated sample can be identified and analyzed according to the X-rays diffraction pattern features such as the position, intensity and number of diffraction lines. The diffraction lines obey to the Bragg equation 2.9 which depends on the X-ray wavelength, the reticular distance ($d=d_{hkl}$) between a family of parallel (hkl) (figure 9) and the angle of X-ray incidence θ .

$$2d\sin\theta = n\lambda \quad (2.9)$$

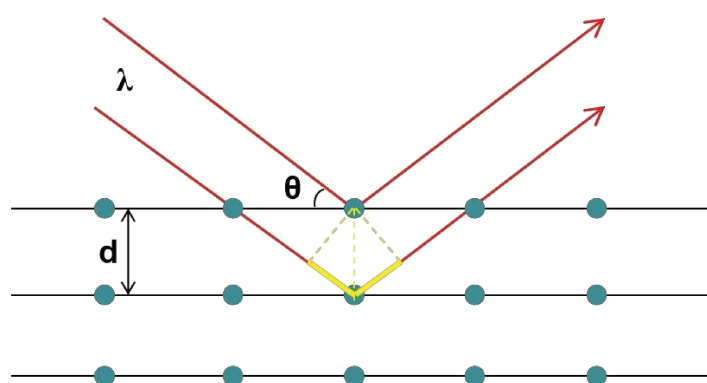


Figure 2.9 Schematic diagram of Bragg diffraction

For a polycrystalline material, the phase composition and changes of ceramics can be identified by analyzing the position, number, intensity, and shape of X-ray diffraction peaks. Through accurate measurement of the angle, intensity and peak shape of the diffraction peak, crystal information such as the cell parameters, phase content, crystal size and distortion of the crystalline structure can be obtained. In addition, through Rietveld refinement analysis of the X-ray diffraction pattern, it is possible to obtain precise insights on the lattice parameter changes, unit cell distortions or phases coexistence,...

In this work, a Panalytical-Empyrean X-ray diffractometer shown in Figure 2.10 is used for the structural analysis. The instrument is equipped with a Cu anticathode

with a selected wavelength at 1.5406 \AA and the operating voltage and current are 45 kV and 30 mA, respectively. The experimental patterns are recorded in the range $2\theta = 20^\circ\text{-}70^\circ$ with a step width of 0.013° . Under this experimental condition, a superposition of several scans ensures well resolved XRD patterns. Then X'Pert HighScore Plus software was used to analyze the X-ray diffraction pattern, and compared with the *jcpds pdf* of the standard database to obtain the involved structural features consistent with the diffraction patterns. In this identification process, the Rietveld module for analysis and refinement leads to the lattice constants, intensity and the FWHM (full width at half maximum) of the spectral peaks.



Figure 2.10 PANalytical-Empyrean X-ray diffractometer

2.2.5 Raman Spectroscopy

Raman spectroscopy provides deep insights on the vibrational properties of materials. The studies are based on the light scattering by the molecules due to their vibrational motions which are characteristic of their compositions, geometries, bond lengths,.. Raman spectra of the materials can be used to identify the involved molecular groups, the crystalline structure, co-existence of phases...

The physical principle of Raman scattering is based on the interaction between an excitation line (photons) and the vibrational spectrum of the molecules. As depicted in

Figure 2.11 (a), the induced transitions between molecular levels give rise to the Raman spectrum. When the molecules in the sample are illuminated by a laser excitation, different scenarios can occur depending on the photon energy compared to the vibrational energy levels of the molecules. Thus, if the energy of the incident photon is much greater than the energy required for the transition between vibrational energy level, and not enough to excite the electronic states, the molecules in the ground state energy level will absorb the photons and reach virtual excited states. Such excited states are unstable and return to the ground state by an emission of a scattered light. The scattering process is divided into Rayleigh scattering and Raman scattering according to the initial and final vibrational energy levels of the molecule. The Rayleigh scattering is a process in which the virtual state of the molecular returns to the ground state without any change on the initial photon frequency. Raman scattering occurs when the return of the molecules from the virtual to the ground state is accompanied by a photon of energy higher or lower compared to the initial absorbed photon. Depending on the difference between these frequencies the Raman process can be associated to Stokes Raman line and anti-Stokes Raman line. The corresponding frequencies are located on both sides of the Rayleigh line at equal intervals, as shown in Figure 2.11 (b). According to Boltzmann's law and at room temperature, most molecules are at the lowest vibrational energy level in the ground state, and the most molecules return to the same vibrational energy level after being excited by photons. Thus, Rayleigh scattering is stronger than Stokes scattering while anti-Stokes scattering has the lowest intensity. Therefore, the Stokes Raman lines are preferentially recorded and are located at Raman shift position ($\Delta\nu$) defined with respect to the Rayleigh scattering line being located at the origin.

When the sample is irradiated with incident light, the charge distribution in the dielectric molecules or some of the groups changes, which causes polarization. Molecules produce induced dipole moments in the photoelectric field, which causes the energy exchange between the molecules and the incident photons during the vibration of the molecules, thereby generating Raman spectra. The induced dipole moment ρ has the following relationship with the photoelectric field E and molecular polarizability α :

$$\rho = \alpha E \quad (2.10)$$

Concerning the Raman activity of molecular vibrations, only the ones that cause changes in the molecular polarizability will produce Raman scattering lines which correspond to Raman active vibration modes. In crystalline structure, the Raman process which probes the vibrational features is analyzed in terms of Raman modes which depend on the crystalline space groups, the crystalline quality....

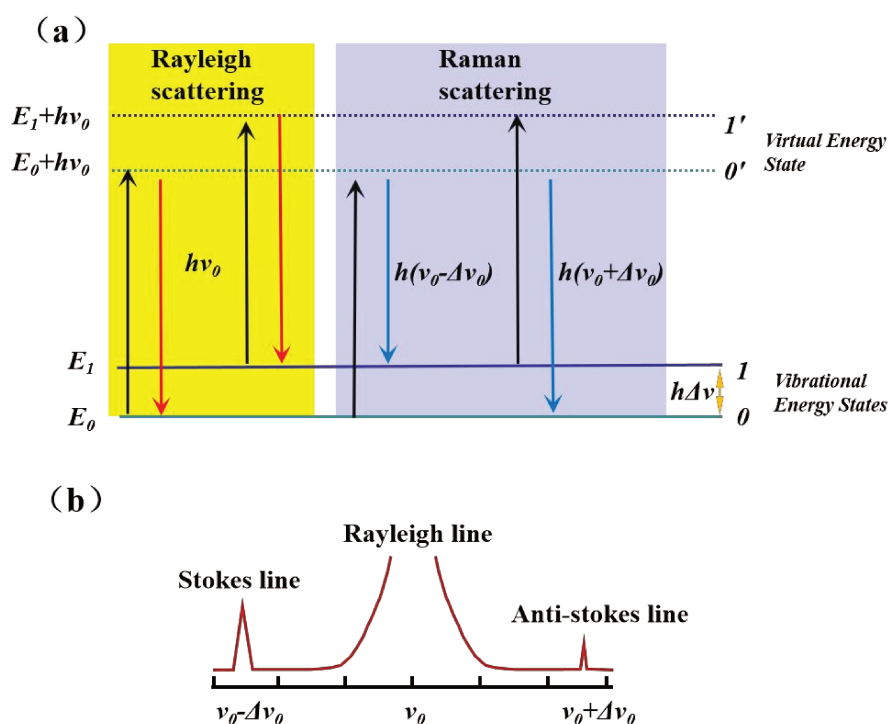


Figure 2.11 (a) Molecular scattering energy level diagram (b) Scattering spectrum diagram

In this work, the XploRA laser Raman spectrometer from HORIBA company shown in Figure 2.12 is used for Raman spectroscopy experiments to analyze the changes of the ceramic structure. All samples were investigated by using a 532 nm laser diode excitation light source and 4 mW output power, and the experiments were performed under a microscope with an objective lens of $\times 50$ LWD. Raman spectra were recorded in the wavenumber range of 90-1200 cm^{-1} .



Figure 2.12 XploRA Raman spectrometer from HORIBA Company

2.2.6 Electron Paramagnetic Resonance

Electron paramagnetic resonance (EPR), also known as electron spin resonance (ESR), is a spectroscopy technique that can directly detect and study paramagnetic species with unpaired spins involved in materials. Under a static magnetic field (B) and a microwave radiation with a fixed frequency (ν), transitions are induced between the spin levels in the resonance conditions. Particularly, by sweeping the magnetic field B , an EPR transition occurs between two spins states with an energy difference ΔE when $B=B_0$ according to the relation (Equation 2.11):

$$\Delta E = g\beta B_0 = h\nu \quad (2.11)$$

With β the Bohr magneton and g factor which characterize the electronic states of the paramagnetic species (ions, radicals, F-centres,...). The EPR line associated to the transition is a derivative of the microwave power absorbed at the resonance condition as depicted in Figure 2.13. The magnetic field at the resonance defines the line position and determines the value of g -factor according to equation 2.11. In a crystalline structure, g -factor is in general represented by a tensor with the components depending on the direction of the magnetic field in the crystalline frame. Thus, the EPR signal contains the information on the symmetry of the local environment around the paramagnetic centre.

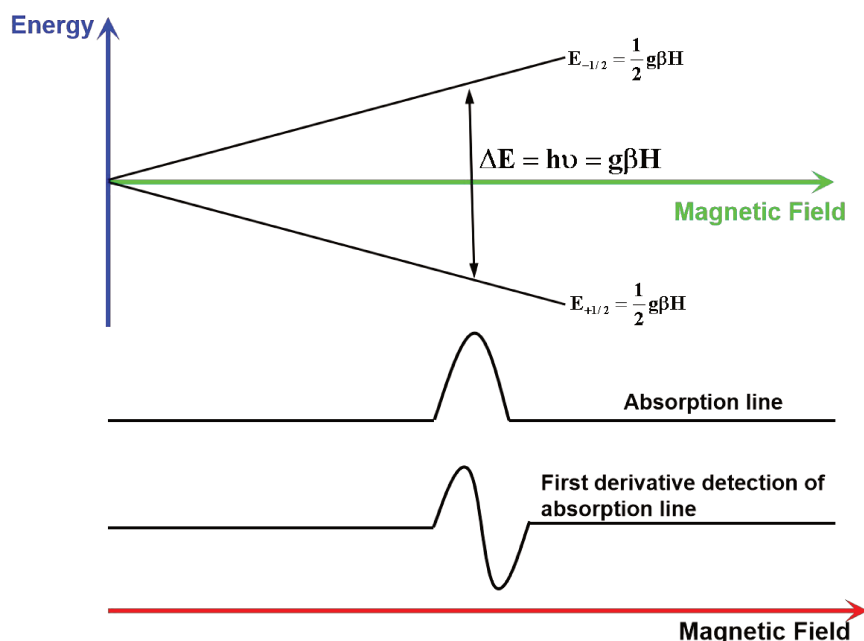


Figure 2.13 Schematic of Electron Paramagnetic Resonance, the magnetic field is swept and induces splitting of the energy of spin states. At the resonance conditions, absorption of microwave power with fixed frequency provokes a transition between the spin states. The EPR line is the derivative of the microwave absorption curve.

In this work, an X-Band Bruker EMX spectrometer (Figure 2.14) is used for EPR experiments in ZnO-based ceramics with different doping elements. Due to the high electrical conductivities in the samples, the microwave power in the resonant EPR cavity is highly damped by the charge carriers and this effect prevents to detect an EPR signal. Therefore, ZnO ceramics were ground into powder to limit the macroscopic conductivity and succeed to record the EPR spectra. The relevant experimental parameters consist in a microwave frequency at 9.5 GHz, microwave power at 20 mW magnetic field modulation frequency at 100 kHz and magnetic field modulation amplitude about 5 G. The EPR spectra were recorded in the range 0 to 6000 G with a magnification when a high resolution of the EPR lines is required for the simulation with a precise evaluation of the EPR spectral parameters (g-factor, FWHM, Integrated intensity). Finally the EPR experiments can be performed at different temperatures from 4 K-770 K by using suitable cryostats (Bruker 100 K-300 K, Oxford Instruments 4 K-300 K and Bruker high temperature 300 K-750 K).



Figure 2.14 Electron paramagnetic resonance spectrometer

2.2.7 Nuclear Magnetic Resonance

Nuclear magnetic resonance spectroscopy abbreviated as NMR is a resonance spectroscopy technique that detects the magnetic resonance signals from nuclei with nuclear spins. As examples of nuclei with non-zero spins and then magnetic moments, we report the cases of ^1H , ^{13}C , ^{15}N , ^{27}Al , ^{67}Zn , etc.). The main principle of NMR experiments is similar to EPR but the static magnetic field is higher (around 7 T) and the frequency is in the range ~ 100 MHz. However, instead of continuous wave which irradiates the samples in EPR, NMR technique is used with pulsed radio-frequency wave with defined pulse duration and delays. Under the static magnetic field and radio-frequency electromagnetic radiation the nucleus can absorb the electromagnetic wave with the corresponding frequency and then a nuclear magnetic resonance transition phenomenon occurs between the nuclear spin levels being modified by the static magnetic field^[1]. In usual experiments, the magnetic moment of spin systems is in equilibrium aligned along the fixed magnetic field taken as Oz axis. By using pulsed radio-frequency radiation, the magnetization is out from the Oz axis and the return to the equilibrium is made according to relaxation processes associated with the energy transfer from spin system to the environment such as lattice and other neighboring spins. Relaxation times are involved and account for the time dependence

of the magnetization during the return to equilibrium. The time dependence of magnetization can be transformed by Fourier to obtain the experimental NMR spectrum^[2]. According to the relative intensity, chemical shift and FWHM of resonance peaks in NMR spectrum, the local environments of the nuclei and structural characteristics of the material can be analyzed.

High-resolution solid-state magnetic resonance method has become a relatively complete and advanced characterization method. Experimental versatility of the Solid state NMR technique is developed including magic angle spinning, cross polarization between neighboring nuclei as well as particular sequences of pulses and detection required for relaxation times evaluation. Figures 2.15 and 2.16 show the setup of a typical NMR instrumentation, which mainly includes superconducting electromagnet, RF transmitter, RF receiver and amplifier, magnet poles, sweep generator, sweep coils, sample tube, control console and recorder, etc.

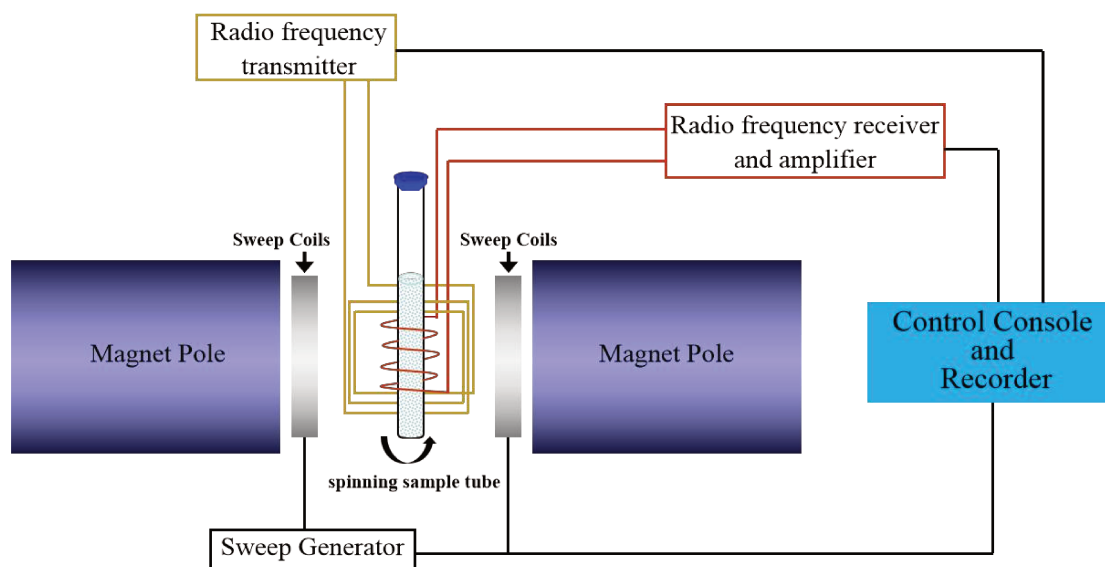


Figure 2.15 Schematic diagram of NMR spectrometer



Figure 2.16 NMR spectrometer

^{27}Al and ^{67}Zn nuclei can be investigated by Solid state NMR in Al_2O_3 doped ZnO ceramics due to their resonance transitions at characteristic chemical shifts. For the NMR studies, the ceramic pellet needs to be ground into small ceramic particles and then suitable amount particles are placed in a cylindrical rotor for magic angle spinning (MAS) required for NMR experiments. In this work, ^{27}Al solid state NMR experiments were realized at a magnetic field of 7.0 T (corresponding to a ^1H Larmor frequency of 300 MHz), equipped with a 2.5 mm VTN dual channel probe. The investigated ceramics were ground into particles and filled into rotors of 2.5 mm outer diameter. The spectra were acquired under magic angle spinning (MAS) of 25 kHz. 12 K scans were accumulated with a recycle delay of 5 s. The spectra were referenced to an aqueous solution of $\text{Al}(\text{NO}_3)_3$. ^{67}Zn spectra were acquired under static conditions with a 7 mm VTN dual channel probe adapted for low frequencies. Different amounts of samples (typically about 600 mg) can be investigated. Between 24 and 60 K scans were accumulated with a 100 ms echo sequence, the recycle delay was 2.5 s. The spectra have been referenced to a saturated solution of $\text{Zn}(\text{NO}_3)_2$.

Chapter 3

Role of the reducing sintering atmosphere on the electrical properties and microstructure of (Al, Ti, Mg) oxide co-doped ZnO ceramics

3.1 Introduction

ZnO with wurtzite structure is a well-known semiconducting oxide (SCO) with a direct wide band gap ($E_g=3.37\text{eV}$) and a large exciton binding energy (60 meV) at 300K^[1]. This compound possesses also several further advantageous properties such as a high abundance, low toxicity, high stability and good optical transparency^[2, 3]. These features are the reasons for the application of ZnO in varistors, gas sensors, transparent electrodes, solar cells, liquid crystal displays, piezoelectric, electro-optical and thermoelectric devices^[4-9].

Intrinsically, ZnO is a n-type SCO due to native defects as zinc interstitials (Zn_i) as well as neutral or charged oxygen vacancies (V_O , V_O^\cdot , $V_O^{\cdot\cdot}$). However, the substitutional doping by metallic elements as Al, Ti, Ga, In, etc. contributes to an enhanced n-type conductivity^[10, 11]. In particular, a small atomic percentage of Al doping ($Zn_{1-x}Al_x$)O in the range $0 < x < 0.05$ enhances critically the conductivity up to $10^5 \text{ S}\cdot\text{cm}^{-1}$ in a dense form as it may be realized in ceramics^[8]. On the other hand, a proper doping by TiO_2 also plays a similar role as Al_2O_3 and the substitution of Zn^{2+} by Ti^{4+} provides donor centres enhancing the carrier concentration and the conductivity^[12]. However, the tendency to form a minor spinel phase compromises the efficiency of Ti doping compared to Al to improve the electrical properties. For MgO doping, a slight increase of the band gap occurs even if the electron concentration increases in $Zn_{1-x}Mg_xO$ ($x=0-40\%$) with the doping content through a process of point defects creation in ZnO^[13]. Beyond the nature of the doping elements, the thermal treatment of

the doped ceramics also modulates the conductivity. Thus, ZnO ceramics co-doped by Al₂O₃ and TiO₂ possess higher electrical conductivities by using spark plasma sintering (SPS)^[14] or when the sintering is carried out under a reducing atmosphere such as N₂+CO^[15]. In these cases, improving the Hall mobility occurs from a limitation of the intrinsic acceptor defects at the grain boundaries along with the reduction of Schottky barriers, as earlier discussed by Tian^[15]. Depending on its oxidizing or reducing nature, the sintering atmosphere has a major effect on the performance of ceramics. In particular, the defect content in oxide ceramics is related to the oxygen partial pressure in the sintering atmosphere^[16, 17]. This effect is in detriment to the required n-type behavior for higher conductivities. Oppositely, due to the lack of oxygen in N₂ or in N₂+CO atmosphere, more intrinsic defects such as Zn_i atoms and oxygen vacancies are formed, contributing to a higher charge carrier concentration in ZnO ceramics^[18]. Thus, the nature of the involved defects and their stabilization in doped ZnO based ceramics play a key role on the electrical conductivity. In this aim, the doping elements and the sintering atmosphere are worthy of interest.

The above-mentioned features require deep insights on the doping ions in the lattice, as well as the sintering atmospheres which modulate their location in the host structure and the interaction with the lattice defects. Al₂O₃, TiO₂, and MgO were chosen as co-dopants of ZnO ceramics with the motivation to study their influence on the structure, morphology and electrical properties of the co-doped compounds. Characterization by XRD and Raman spectroscopy were used to analyze the changes on the structural and vibrational features due to the doping which may contribute to the lattice site distortion or to a secondary phase formation^[19, 20]. Electron paramagnetic resonance (EPR) spectroscopy and nuclear magnetic resonance (NMR) spectroscopy are local probe techniques. NMR can determine the coordination of defined chemical elements such as ²⁷Al, while EPR can identify paramagnetic doping ions or electronic active defects. Indeed, EPR is sensitive to some valence states of doping ions and also to the spin carrier species such as charged vacancies, anti-sites or interstitials (oxygen, zinc). Former works reported a fingerprint EPR signal at a g-factor of 1.960 was usually found as consequence of the involved defects in doped ZnO

ceramics^[21, 22]. Electrons in the conduction bands or defects as shallow donors formed by oxygen, zinc vacancies or interstitials are the possible EPR active centres also considered at the basis of the electrical behavior. NMR studies determine the host lattice sites of Al ions in the ZnO lattice and identify the environment of ²⁷Al ions^[23]. In addition, a characteristic NMR signal in Al-doped ZnO at the chemical shift 185 ppm was observed in all samples and cannot accommodate with Al being coordinated by Oxygen. The origin of this line can be caused by Knight shift effect from the conduction electrons as discussed by Momot et al.^[24] or induced from grain boundaries where chemical disorder and non-stoichiometry are involved. Therefore, NMR and EPR are effective methods to investigate the defect structure in ZnO ceramics.

Thus, the present work is dedicated to the fabrication of doped ZnO ceramics incorporating TiO₂, Al₂O₃ and MgO in defined ratios. Different sintering atmospheres (air, N₂, and CO+N₂) were considered in order to evaluate the reduction or oxidation effects on the coordination and stable valence states of doping elements along with the induced lattice defects. The investigations point out the gradual increase of the conductivity when using, respectively, air, N₂, and CO+N₂ as a sintering atmosphere with the highest conductivity $\sigma = 1.5 \times 10^5 \text{ S} \cdot \text{m}^{-1}$ at room temperature. The structural, composition and morphology investigations of the ceramics were carried out by using XRD, Raman and SEM. Exhaustive analyses were devoted to the local order probed by ²⁷Al solid state NMR and to the electronic active centres investigated by EPR. A good correlation was demonstrated between the 185 ppm NMR signal and the conductivity. A similar approach was also made from EPR experiments in order to correlate the intensity of EPR signals with the conductivity and the nature of the involved electronic active defects.

The work in this chapter establishes the relationship between the sintering atmosphere, the structure composition, the type of defects and the electrical properties through experimental analysis.

3.2 Sample preparation and characterization

Co-doped ZnO ceramics with the respective molar ratio (0.25 mol.%) Al_2O_3 , (0.50 mol.%) TiO_2 and (1.00 mol.%) MgO were synthesized by a conventional solid-state reaction method. The fabrication steps consist in ball milling the reactants, drying the products at 120 °C followed by calcination at 450 °C. Under the sintering conditions of temperature of 1200 °C and holding time of 2 hours, ZnO-based ceramic samples were prepared under different sintering atmospheres (air, N_2 , N_2+CO), referred below as A, N and C samples according to the sintering atmosphere, respectively.

The experimental methods used in the analysis and characterization mainly includes: The self-assembled four-probes resistance equipment was used to measure the conductivity and temperature coefficient of resistance of the samples. SEM was used for the observation of the surface morphology of ceramic samples and to analyze the compact structure and phase distribution. XRD and Raman investigations were used to obtain the phase structure and composition of ceramic samples. EPR and NMR were used to investigate the changes in local defects and structural disorder. From the perspective of structural defects, the effects of different sintering atmospheres on the conductive properties of ZnO-based ceramics were explored. The experimental parameters and procedures for the different characterization methods are detailed in the Chapter 2.

3.3 Structural and morphology studies

XRD and SEM experiments were conducted to show the effect of doping and sintering atmosphere on the structure and morphology of samples. Fig. 3.1a shows XRD patterns of ZnO doped TiO_2 , Al_2O_3 and MgO ceramics sintered in air (A), N_2 (N) and N_2+CO (C) respectively. The refinement procedure points out the main crystalline phase as the hexagonal wurtzite ZnO (JCPDS No. 36-1451) superimposed to a minor spinel phase Zn_2TiO_4 (JCPDS No. 18-1487). Fig. 3.1b reveals a small angle shift of the XRD line related to the secondary phase Zn_2TiO_4 as a function of the sintering

atmosphere. Moreover, focusing on the intense XRD diffraction lines of ZnO and Zn_2TiO_4 , their refinement was achieved by using a Gaussian line-shape. Fig. 3.2a, 3.2b summarize the Zn_2TiO_4 ratio and the ZnO lattice parameters for the involved ZnO structures.

Irrespective to the sintering atmosphere, XRD experiments did not show any secondary phases related to Al or Mg. Thus, these elements exhibit a higher solid solubility limit into the host ZnO lattice compared to Ti ions. Indeed, for TiO_2 doping, the formation of a spinel phase indicates different dissolution degrees in ZnO lattice depending on the sintering atmosphere. Thus, sample C has the lowest content of the secondary Zn_2TiO_4 phase (Fig. 3.2a) and suggests a preferential incorporation of Ti ions into ZnO. As a consequence, an expansion of the lattice parameters (a, c) occurs due to the different ion radius of Ti compared to Zn (Fig. 3.2b).

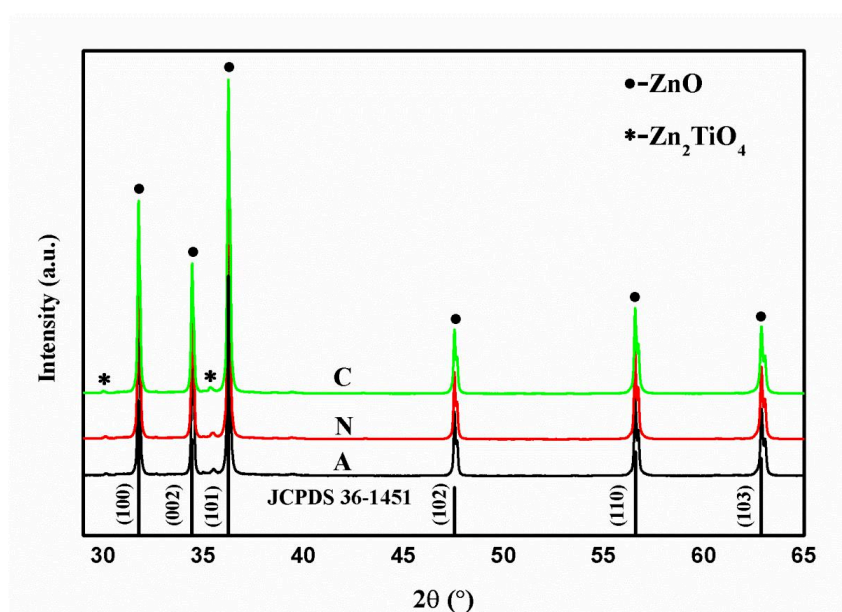


Figure 3.1 XRD patterns of ZnO-doped ceramics (A, N, C)

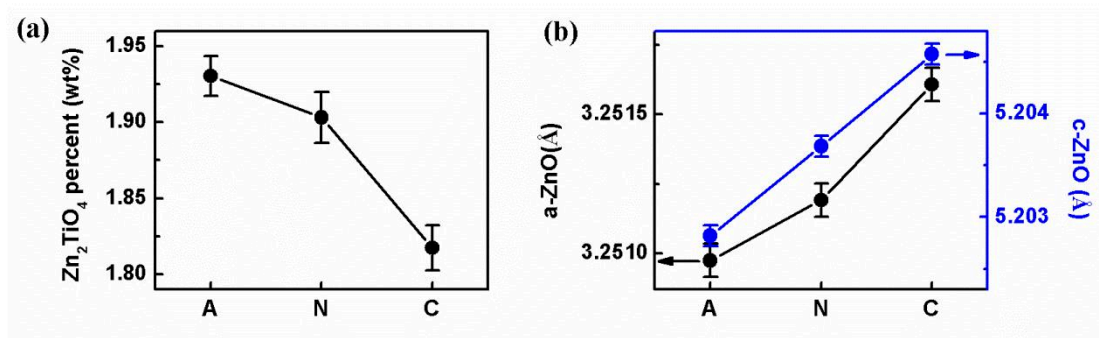


Figure 3.2 (a) Lattice parameters (a and c), (b) The content of Zn₂TiO₄ of ZnO in samples (A, N, C) through Rietveld refinement

In order to shed light on the organization of the ceramics composed by the two segregated phases, SEM experiments were performed on the considered samples as shown in Fig. 3.3 (a, b, c) for A, B, and C samples respectively. Similar features were seen with a dense structure, an average size in the range 10-15 μm (Fig. 3.3d) and marked boundaries. In addition, EDS analysis was realized on two selected zones shown in Fig. 3.3a; i.e. large grains (zone 1) and small clusters (zone 2). The large grains analysis shows the major composition from ZnO phase, while the incrustated small dots with rounded shape possess a chemical composition which is consistent with the minor spinel phase Zn₂TiO₄ in agreement with XRD investigations. This secondary phase is also located in the grain boundaries and seems to prevent the grain growth notably by a pinning effect^[25]. Besides, it was also inferred that Mg and Al ions can be dispersed in the ZnO lattice, while only a small amount of Ti can be found in ZnO grains due to its low solid solubility as shown in Table 3.1. However, N₂+CO sintering atmosphere increases the solid solubility limit of Ti in ZnO due to its reducing effects. Sintering atmosphere has an effect on the formation of spinel phase, sample C contains the least amount of spinel due to the high content of Ti in the ZnO grains, thus the average grain size is gradually increased for samples A, N and C, as shown at Fig. 3.3f.

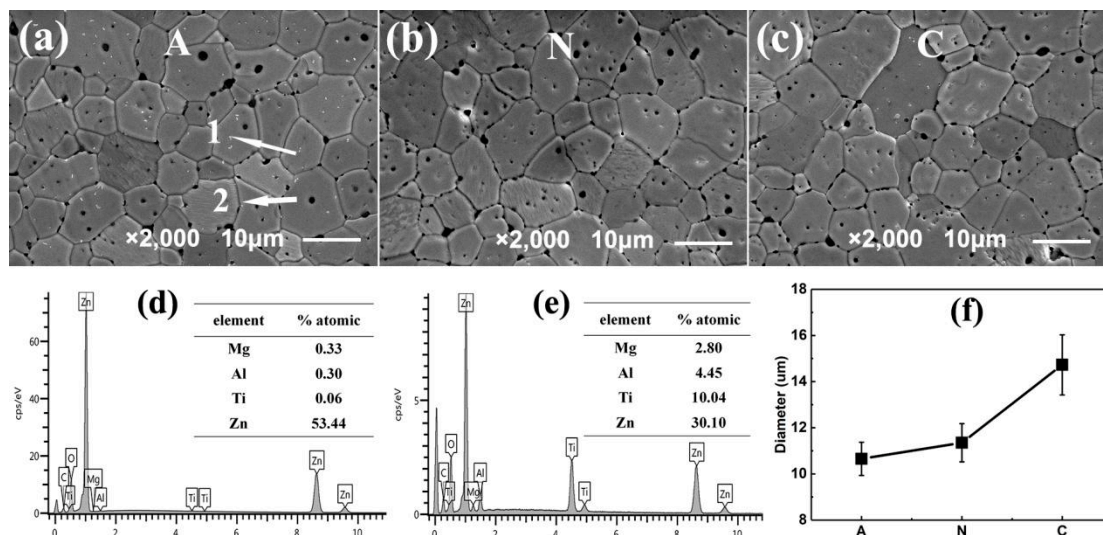


Figure 3.3 SEM images of doped ZnO ceramics (A - (a), N - (b), C - (c)). (d) and (e) : atomic ratios involved in the zones 1 and 2 of sample A by EDS analysis, (f) : average grain size

Table 3.1 Atomic percentage of Ti in ZnO phase by EDS analysis

Samples	Ti in ZnO phase (at.%)
A	0.06
N	0.09
C	0.16

The above investigations of the structural and morphology features point out the role of the sintering atmosphere on the involved crystalline phases and the microstructure of doped ZnO based ceramics. Moreover, relevant insights were also inferred on the solid solubility of the doping elements in the host structures, the ratio of the secondary phase and its location as isolated clusters on the main ZnO grain and also in the grain boundaries. This organization of the doped ceramics is expected to interfere on the electrical behavior which is expected from the doping process as discussed below.

3.4 Conduction features in ZnO ceramics

Conductivity measurements were performed on samples A, N and C by using the four-probes method and the results at different temperatures are summarized in Fig. 3.4. A significant increase of the conductivity is obtained in the different samples with the highest value at room temperature ($\sigma = 1.52 \times 10^5 \text{ S} \cdot \text{m}^{-1}$) achieved for the C sample. The thermal evolution of the conductivity in the range $[-50 \text{ }^\circ\text{C}, 150 \text{ }^\circ\text{C}]$ is almost similar for the samples A and N in contrast to the metallic-like behavior of the sample C. The exact role of the sintering atmosphere on the electrical behavior of doped ZnO ceramics is then clearly traduced on the conductivity values and its thermal evolution profiles. Charged vacancies and shallow donors induced by doping and sintering are necessary attributes to the conductivity. Particularly, oxygen vacancies favor the incorporation of doping elements in the lattice^[26] and the Al_{Zn} ions in crystalline sites of ZnO favor the high concentration of donor centres. For the application of ZnO conducting ceramics, the temperature coefficients of resistance (TCR) are worthy of interest. Their estimation was made in the temperature range $-50 \text{ }^\circ\text{C}$ to $150 \text{ }^\circ\text{C}$ (Fig. 3.4b) for samples, the results shown in Fig. 3.4 b indicate that ZnO-doped conducting ceramics can be used in a wide temperature range due to their quite low TCR. Samples A and N have negative TCR about $-626 \pm 6 \text{ ppm}/^\circ\text{C}$ and $-598 \pm 6 \text{ ppm}/^\circ\text{C}$ respectively, while sample C shows a positive TCR, $749 \pm 7 \text{ ppm}/^\circ\text{C}$. Lyashkov et al.^[27] claimed that negative TCR leads to an S-shaped curve of the current-voltage characteristics when the temperature is raised. In particular, a dramatic consequence of a negative TCR can manifest in a failure of the component performances. Also, by using $\text{N}_2 + \text{CO}$ sintering of ZnO based ceramics, the sample C achieves a positive TCR to ensure the working stability of electrical circuits as it may be required in metal-oxide varistors.

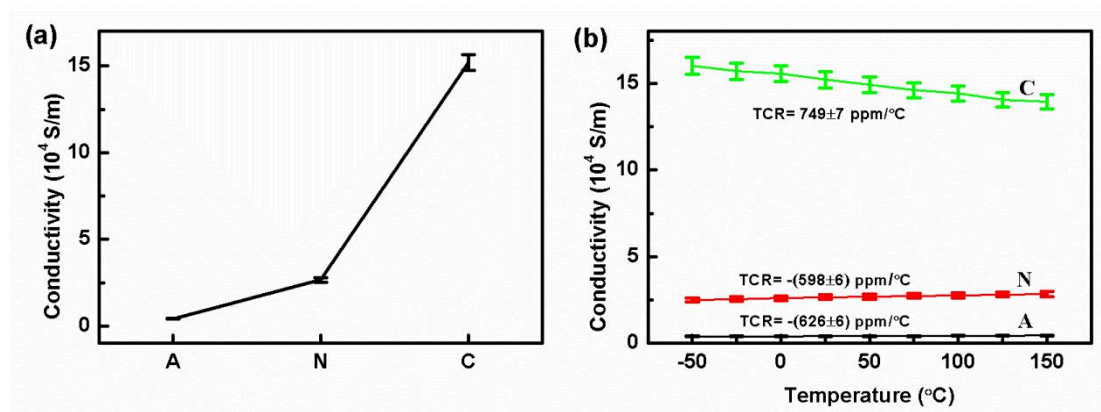


Figure 3.4 (a) Electrical conductivity of ZnO based ceramics (A, N, C) at room temperature, (b) TCR coefficients in the temperature range -50 °C to +150 °C

The above results underline that, while the doping and sintering conditions alter moderately the structural and microstructure of the doped ceramics, their corresponding electrical behaviors exhibit a marked difference on the conductivity values and its thermal evolution. The solid solubility limits of the doping elements depend on the sintering atmosphere particularly for Ti ions. Moreover, the incorporation of doping ions in the host lattice requires a reorganization of the local environments to accommodate with ionic radius and stable valence states. As matter of fact, charged vacancies and shallow donors induced by doping and sintering are necessary attributes to the electrical conductivity. Also, it was claimed^[26] that oxygen vacancies favor the incorporation of doping elements in the lattice and the Al_{Zn} ions in crystalline sites of ZnO leads to a high concentration of donor centres^[28]. Relevant experimental approaches based on Raman, EPR and Solid State NMR are outlined below in order to analyze quantitatively the doping effects from the lattice distortion in substitutional sites and the nature of electronic active defects in the doped structures.

3.5 Vibrational signatures of doped ZnO based ceramics

In doped ZnO ceramics, Raman studies give precise insights on the crystalline structures and local lattice distortions which may be induced by doping, defects or disorder. Indeed, the difference in the valence states and ionic radius induces distortions of the host crystalline sites and favor interstitials or vacancies. Also, the aim of the Raman studies is to compare the doping effects in ZnO based conducting

ceramics as a function of the sintering atmospheres. From Raman spectra, the wurtzite ZnO structure is involved and belongs to C_{6v}^4 ($P6_3mc$) space group with the unit cell containing 4 Zn atoms coordinated by oxygen atoms. According to group theory analysis, 12 normal modes are allowed by symmetry with 9 optical modes and 3 acoustic ones. The optical modes of ZnO can be expressed at the Brillouin zone center by the irreducible representation ($\Gamma=A_1+2B_1+E_1+2E_2$). Excluding B_1 modes as they are Raman inactive in perfect structure, the main characteristics of the Raman active modes are hereafter addressed. A_1 and E_1 modes are polar and active in IR and in Raman. They can split into longitudinal (LO) and transverse optical (TO) components due to their polar nature^[29] The nonpolar E_2 mode is Raman active only, and consists in two modes with low and high frequency phonons (E_2^{low} and E_2^{high}). From the obtained Raman spectra in Fig. 3.5, six Raman active modes are reported for wurtzite ZnO structure and consist in E_2^{high} , E_2^{low} , $A_1(TO)$, $A_1(LO)$, $E_1(TO)$ and $E_1(LO)$ modes. Additionally, second order Raman lines are also observed and occur from multi-phonon processes such as overtone of 2TA mode at 208 cm^{-1} , $E_2^{high}-E_2^{low}$ mode at 340 cm^{-1} , TO+LO mode at 1090 cm^{-1} and 2LO mode at 1150 cm^{-1} . Table 3.2 summarizes the main results of the Raman active modes^[30-32] for samples A, N, C.

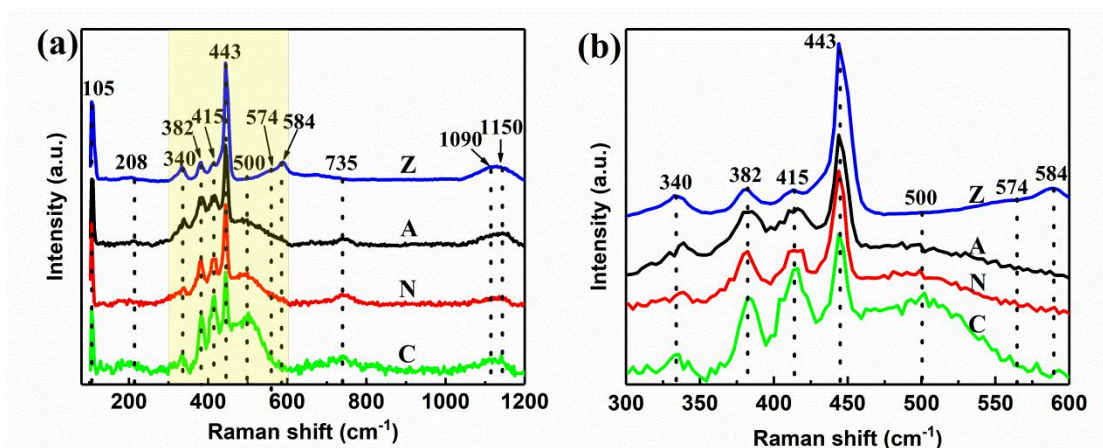


Figure 3.5 (a) Raman spectra and (b) the enlarged region from 300 to 600 cm^{-1} for the undoped ZnO (Z) and for samples A, N and C

Table 3.2 Measured Raman modes in samples A, N and C and their assignment in doped ZnO based ceramics

Normal mode designation	Raman shift ($\pm 2 \text{ cm}^{-1}$)	Assignment
E_2^{low}	105	Vibration Zn sub-lattice
B_1^{low}	250	Active only by disorder
$A_1(\text{TO})$	382	Oxygen vacancies
$E_1(\text{TO})$	415	Polar mode sensitive to crystal orientation
E_2^{high}	443	Vibration of oxygen sub-lattice
$A_1(\text{LO})$	574	Interstitial Zn_i
$E_1(\text{LO})$	584	Oxygen vacancies
Disordered Raman band	500	(*) Active by disorder due to interstitial Zn_i
A_{1g}	735	(*) Spinel phase

(*): Silent in ZnO

Significant changes are involved between the Raman spectra of samples A, N and C. First, $A_1(\text{TO})$ mode at 382 cm^{-1} induced by oxygen vacancies, shows gradual increase for samples A, N and C. Second, the B_1 mode at around 500 cm^{-1} , tentatively assigned by Friedrich et al.^[30] to vibration of interstitial Zn_i - O_i bonds, show different behavior in the conducted samples (A, N, C). As suggested by Serrano et al.^[32], the transitions between the optical modes involved at the Brillouin zone center are forbidden in a perfect crystalline structure but become allowed in a disordered lattice. The Raman frequency shifts for these transitions are distributed in the range $400\text{-}600 \text{ cm}^{-1}$, i.e. in the same range as the one covered by the broad background shape. Based on the dispersion curves in the reference^[32], the lattice defects contribute to disordered structures, which can activate the Raman mode (B_1). Therefore, this broad Raman band, tentatively attributed to disorder, depends on the sintering atmosphere; i.e. its intensity is higher in sample C compared to N or A samples. These features are indicative on the dependence of the doping efficiency or the modulated solid solubility limit by the used sintering conditions.

Raman spectra are consistently interpreted by the allowed modes of wurtzite structure.

Good crystalline quality is inferred from the well resolved and narrow Raman bands. However, disorder occurring from interstitial Zn_i seems involved as traduced by the broad Raman band around 500 cm^{-1} inducing transitions between optical modes at the Brillouin zone center.

3.6 Electronic active defects probed by EPR

EPR experiments were realized on doped ZnO ceramics (A, N, C) ground to powders with particle size of about $100\text{ }\mu\text{m}$. Indeed, the EPR spectra cannot be recorded on doped ZnO in the form of dense ceramics. The macroscopic conductivity in bulk ceramics induces strong damping of the EPR resonant cavity through the absorption of the microwave power. Therefore, we need to grind ZnO ceramics into powder to record their EPR signatures. In the performed experiments, the EPR spectra consist in a single resonance line with a weak asymmetry (Fig. 3.6). The spectral parameters intensity and line width depend strongly on the sintering atmosphere (A, N, C) but the paramagnetic species (PS) are associated to unpaired spins ($S=1/2$) located in a slightly anisotropic environment as traduced by the small asymmetry of the EPR line. The average value of the g-tensor components at 1.960(2) is a characteristic EPR fingerprint in all samples suggesting the same origin of the PS in the different samples irrespective to the sintering atmosphere. These PS are no longer connected with grains or surface effects and seem involved in the same crystalline site of the ZnO structure. Pham et al.^[33] discussed several assignments such as oxygen vacancies, anti-sites or interstitials interacting with the doping ions (Al^{3+} , Ti^{4+}). These defects must be electrically active to ensure the observed charge carriers leading to a high electrical conductivity in ZnO doped ceramics. The PS may in principle also occur from Ti doping ions in the valence state Ti^{3+} . However, Ti^{3+} gives rise to an EPR signal with a characteristic g factor ~ 1.930 ^[34, 35], i.e. quite far from the value 1.960(2), excluding then the involvement of Ti^{3+} . Another argument supporting this exclusion is that the $g = 1.960$ EPR signal remains observed in non-doped ZnO but with a very low intensity. Despite several EPR investigations attributing the $g = 1.960$ EPR signal to V_O^+ , this

assignment remains a subject of an open debate. According to Meyer et al.^[36] and Janotti et al.^[37], positively charged oxygen vacancies are not thermodynamically stable and can be created only under UV irradiation. For zinc vacancies (V_{Zn}), former works by EPR reported g-factors higher than 2.000, excluding then V_{Zn} as an origin for the involved PS. The possibility of zinc interstitials (Zn_i) was discussed by several authors as Sann et al.^[38] and Vlasenko et al.^[39]. This interpretation is consistent with the Raman experiments discussed above which assign the origin of the broad band ($\sim 500\text{ cm}^{-1}$) to disorder introduced by Zn_i .

The EPR spectral parameters line intensity (I_{EPR}) and the line width (ΔH) can be used to evaluate the integrated intensity Π_{EPR} and then the PS concentrations ($[PS]$) through the simple relation: $\Pi_{EPR} \sim [PS] \sim I_{EPR} * (\Delta H)^2$. Fig. 3.6b shows that the higher $[PS]$, the lower is the electrical conductivity. This indicates that all the charge carriers in doped ZnO are not probed by EPR due to their high mobility and short relaxation times. The thermal evolution of the EPR spectral parameters in the range 160 K - 300 K informs on the mobility, stability and thermal activation of the PS. The results are summarized in Fig. 3.6c and 3.6d for Π_{EPR} and ΔH in samples. In no case, the EPR integrated intensity follows the well-known Curie law for localized and non-interacting paramagnetic centres. The observed thermal behavior shows a nearly stationary integrated EPR intensity suggesting a Pauli like spin susceptibility induced by delocalized electrons. Moreover, the line widths of samples A and N remain constant when increasing the temperature while a linear increase is observed for ΔH in sample C as it may occur when conduction electrons contribute to the relaxation of the paramagnetic species (Korringa relaxation).

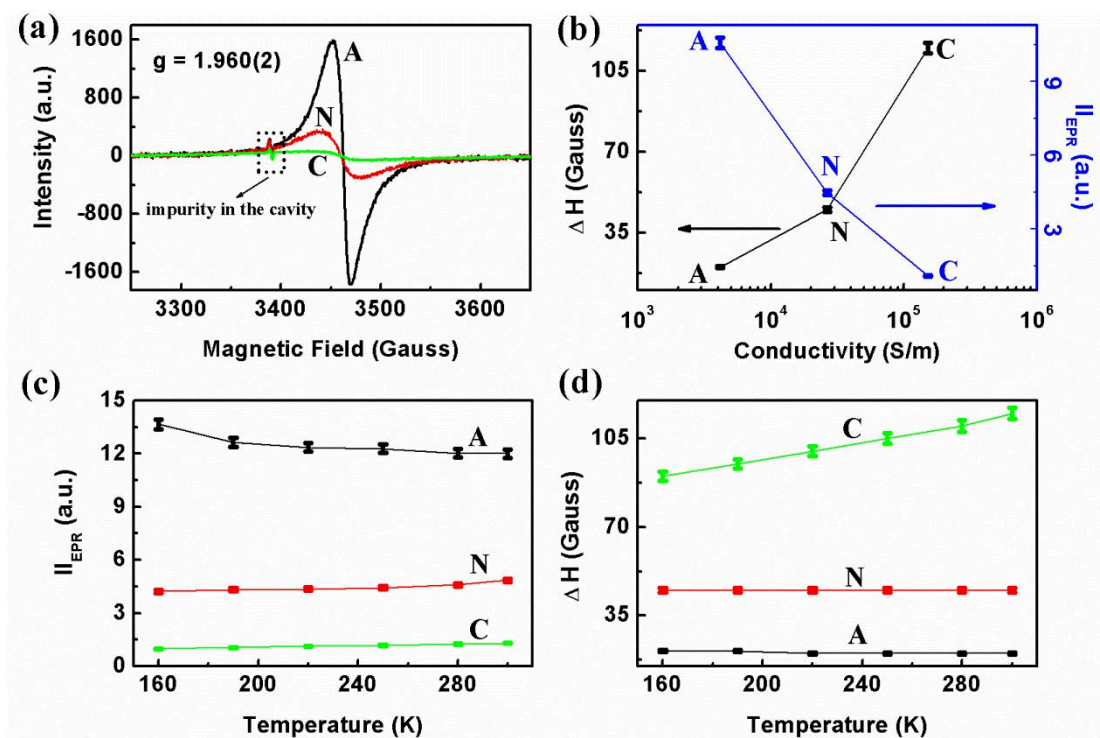


Figure 3.6 (a) EPR spectra in doped ZnO based ceramics. (b) Variation of the EPR signal features, line width and integrated intensity, versus the macroscopic electrical conductivity, (c) Thermal evolution of the EPR line integrated intensity and (d) Thermal evolution of the EPR line width for samples

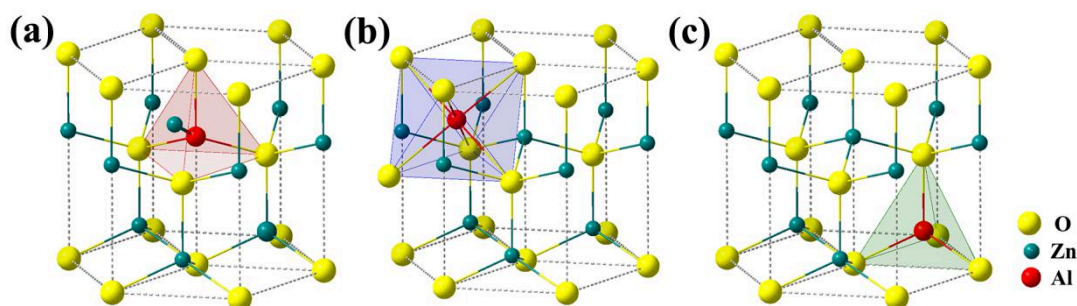


Figure 3.7 Local host sites for Al doping (red spheres-O, green spheres-Zn, blue spheres-Al): (a) Substitutional Al^{3+} - Interstitial Zn^{2+} ($\text{Al}_{\text{Zn}}\text{-Zn}_i$), (b) Interstitial Al^{3+} (Al_i), (c) Substitutional Al^{3+} (Al_{Zn})

Considering the above results and spectral parameters related to the EPR signal features, we may address qualitatively the possible assignment of the paramagnetic centres in doped ZnO. Al_2O_3 doping enhances the charge carriers of the n-type doped ZnO leading to a macroscopic conductivity up to $10^5 \text{ S}\cdot\text{m}^{-1}$ by promoting electrons in

the conduction bands. In the process of Al^{3+} substitution in Zn crystalline sites, lattice defects such as vacancies, anti-sites or interstitials are created and depending on their formation energies, stable configurations are expected to hold preferentially. As discussed above, among the possible charged defects, interstitials (Zn_i) are thermodynamically more stable defects and give rise to paramagnetic centres acting as shallow donors. The thermal activation of their mobility requires energies lower than 10 meV because of their delocalized nature at temperatures as low as 160 K. Thus, the association of substitutional Al^{3+} - Interstitial Zn^{2+} ($\text{Al}_{\text{Zn}}\text{-Zn}_i$) complexes (Fig. 3.7a) account for the active sites hosting the paramagnetic centres which also contribute to the charge carriers in doped ZnO ceramics.

The possibility of creation of ($\text{Al}_{\text{Zn}}\text{-Zn}_i$) complexes can be probed by the Solid state NMR through specific chemical shift related to substitutional Al but with local environment containing the interstitial Zn_i . This is the matter of the forthcoming analysis of ^{27}Al solid state NMR.

3.7 Local order probing of Al doping ions

Solid state NMR investigations were carried out on doped ZnO ceramics in order to probe the ^{27}Al nuclei in the ZnO lattice and to determine their local environments. ^{27}Al MAS NMR spectra of samples A, N and C were recorded with the experimental parameters outlined above. The spectra in Fig. 3.8a show three different environments for Al doping ions as illustrated by three NMR lines located at 0, 80 and 185 ppm with variable intensity depending on the considered samples. The NMR spectra are well resolved suggesting relatively low disorder in the Al location in the host doped structure. The signal at 0 ppm, associated to six-fold oxygen coordinated $\text{Al}^{[40]}$, is observed in all samples with decreasing intensity from samples A over N to C. This NMR line is then assigned to Al being located in interstitial crystalline sites of ZnO with six oxygen in the first coordination shell (Fig. 3.7b). The four-fold oxygen coordinated Al (Fig. 3.7c) was observed only in the sample A from the NMR line

located at 80 ppm (Fig. 3.8a). In contrast to the above usual oxygen coordinated Al, the third NMR line at 185 ppm cannot be associated with oxygen local environment as the chemical shift is far out from the usual range. The intensity ratio between the 185 ppm and the 0 ppm NMR signals increases for C sample; i.e for reducing atmosphere (Fig. 3.8b).

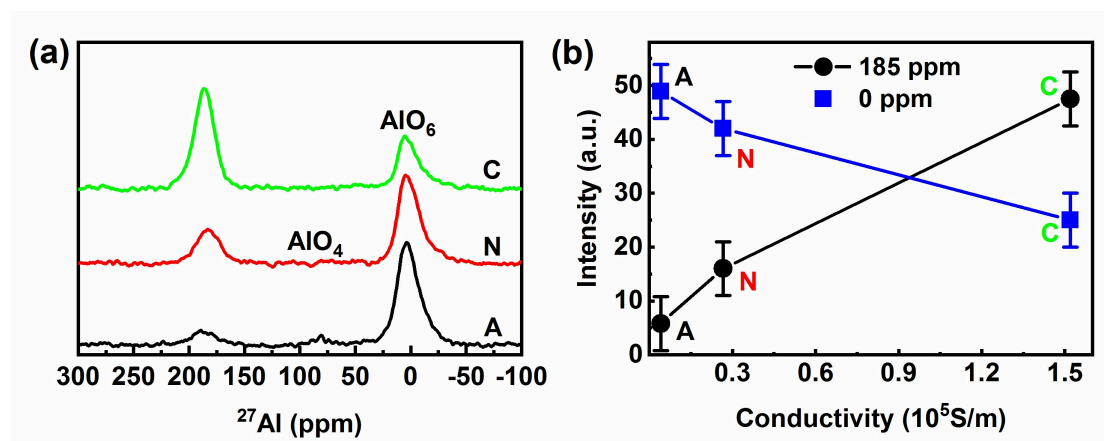


Figure 3.8 (a) ^{27}Al MAS NMR spectra, (b) The peak spectra intensities at 0 and 185 ppm for samples A, N and C

As the doped ceramics exhibit high conductivities, the Knight shift can alter the NMR signals significantly and probably leads to the NMR line at 185 ppm. This was discussed in several reports, but the definite assignment remains a matter of debate. Avadhut et al. investigated Al:ZnO nanoparticles and attributed the broad band around 140 ppm to Knight shift effects^[41]. Straube et al. have also analyzed Al:ZnO by ^{27}Al NMR and attributed the NMR line around 200 ppm to Knight shift induced by conduction electrons^[42]. In a similar report by R. Noriega, on an assembly of Al:ZnO nanowires, they also noticed the existence of a 185 ppm NMR line attributed to interaction between nuclear spin and unpaired spins (paramagnetic species) or to a Knight shift effect from the conduction electrons^[43]. Recently, combining first-principles calculations and ^{27}Al NMR studies of annealed Al:ZnO nanoparticles, Momot et al.^[24] proposed a model to explain the occurrence of the 185 ppm NMR signal. The explanation is based on the realization of energetically favorable complexes associating atomic bonding between Al_{Zn} and Zn_i as illustrated in Fig. 3.7a.

This particular complex gives rise to an extended charge distribution leading to the achieved high conductivity of Al₂O₃ doped ZnO ceramics and ensuring the basis of the Knight shift behind the 185 ppm NMR line. According to Bennett and Carter^[44], the Knight shift is proportional to the Pauli spin susceptibility (χ_p) of conduction electrons which also depends on the electronic density of states at the Fermi level. χ_p can be estimated from the EPR experiments because it is proportional to the integrated EPR signal induced by conduction electrons. This susceptibility is almost constant versus the sample temperature or can show a weak increase with temperature in the same way as it concerns the density of states at the Fermi level. According to the EPR experiments, the integrated EPR line intensity is almost constant versus the temperature (Fig. 3.6c). Thus, the involved spin susceptibility in the samples is Pauli-like. The NMR band centered on 185 ppm can be then assigned to Knight shift or to active electronic defects involved in particular complexes associating (Al_{Zn}-Zn_i). Both origins are possible due to the high conductivity in these doped ceramics as well as the high concentration of paramagnetic electronic defects probed by the EPR study.

It is worth noting that some authors have considered hydrogen as an origin of the shallow donors in ZnO (Hofmann et al.^[45]) and then related to the paramagnetic centres with $g=1.960$. We have also considered this eventuality and performed EPR and NMR investigations on the sample A with the highest concentration of paramagnetic species with $g=1.960(2)$. However, the EPR spectra of sample A reported in Fig. 3.9a were recorded at RT and after annealing at 100°C. The spectra are stable and precise measurements of g -factor gives $g=1.963$. The ¹H-NMR spectra on sample A in Fig. 3.9b did not show any proton signal. Therefore the involvement of hydrogen as an origin of the observed EPR signal is excluded and Zn_i-Al_{Zn} complex can be used as a source of shallow donor defects.

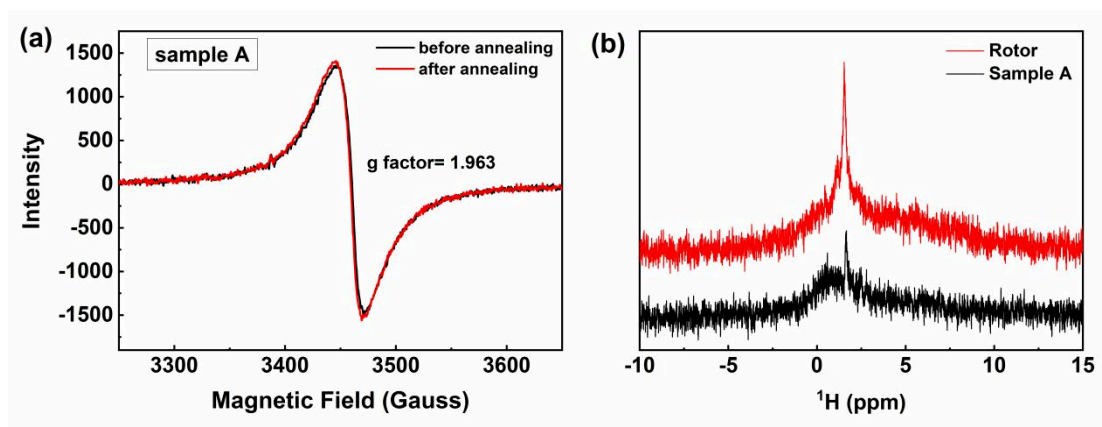


Figure 3.9 (a) EPR signal spectra before and after annealing at 100 °C, (b) ^1H NMR spectra for sample A

3.8 Conclusion

ZnO ceramics were prepared by the solid-state reaction and sintered at 1200 °C under different atmospheres as air (A), N_2 (N) and $\text{N}_2 + \text{CO}$ (C), and the phase composition, morphology and defect composition and distribution of three ceramic samples were studied. The detailed research results are as follows:

1. The electrical conductivity of ZnO ceramics increases in the order of sample A, N, and C, and the sample C prepared under a reducing sintering atmosphere has the highest electrical conductivity $\sigma = 1.5 \times 10^5 \text{ S}\cdot\text{m}^{-1}$.
2. All ceramic samples have a compact structure, containing a good crystalline ZnO wurtzite phase and a small amount of Zn_2TiO_4 spinel phase. The doping of Al_2O_3 , TiO_2 and MgO plays a key role in the crystal characteristics and high electrical conductivity of the ceramics.
3. From Raman studies, active normal modes with a Raman shift of 500 cm^{-1} allowed by the crystalline symmetry were shown as well as additional broad features. Their origin is from silent Raman modes being allowed by the disorder introduced by doping and sintering, which can be attributed to Al defects caused by ion substitution doping of Zn in the host lattice and migration to interstitial positions.

4. The EPR investigations demonstrate the high concentration of unpaired spins associated to electrons from shallow donors or involved in the conduction band. The thermal evolution of the EPR line intensity shows a Pauli-like spin susceptibility which characterizes delocalized electrons.
5. ^{27}Al MAS NMR experiments give precise insights on the local environments of Al ions in the host ZnO grains. Major six-fold and minor four-fold oxygen coordinated were shown from their NMR signal respectively at 0 and 80 ppm. Additionally, an intense NMR signal located at 185 ppm was interpreted as emanating from particular atomic arrangements associating Al_{Zn} and Zn_{i} ions in the first coordination shell, which results in the Knight shift effect.
6. $(\text{Al}_{\text{Zn}}\text{-Zn}_{\text{i}})$ complexes induce an extended charge delocalization which accounts for the high conductivity obtained in sample C ($10^5 \text{ S}\cdot\text{m}^{-1}$) with the suitable positive TCR. This result is promising for possible applications of such optimized ceramics for the working safety of electrical circuits and devices.
7. The ZnO ceramics obtained by sintering under $\text{N}_2 + \text{CO}$ reducing atmosphere have more Al_{Zn} and Zn_{i} , that is, $\text{Al}_{\text{Zn}}\text{-Zn}_{\text{i}}$ complexes, which can generate extra charges ($+1e^-$) to form shallow donor defects and improve the conductivity of ZnO-based ceramics.

3.9 References

- [1] C. H. Seager K. Vanheusden, W. L. Warren, D. R. Tallant, J. A. Voigt. Correlation between photoluminescence and oxygen vacancies in ZnO phosphors. *Applied Physics Letters*[J]. 1996;68(3):403-5.
- [2] A. Janotti, C. Van de Walle. Fundamentals of zinc oxide as a semiconductor. *Rep Prog Phys*[J]. 2009;72(12).
- [3] C. Pan, J. Zhai, Z. Wang. Piezotronics and Piezo-phototronics of third generation semiconductor nanowires. *Chem Rev*[J]. 2019;119(15):9303-59.
- [4] Ming-Wei Wu, Pi-Chuen Tsai, Yi-Chieh Huang. Enhancement of the densification and mechanical properties of aluminum-doped zinc oxide

- ceramics by hot isostatic pressing. *Journal of Alloys and Compounds*[J]. 2015;650:514-9.
- [5] H. S. Huang, H. C. Tung, C. H. Chiu, et al. Highly conductive alumina-added ZnO ceramic target prepared by reduction sintering and its effects on the properties of deposited thin films by direct current magnetron sputtering. *Thin Solid Films*[J]. 2010;518(21):6071-5.
- [6] Pinjun Lan Ye Yang, Muqin Wang, Tiefeng Wei, Ruiqin Tan and Weijie Song. Nearly full-dense and fine-grained AZO:Y ceramics sintered from the corresponding nanoparticles. *Nanoscale Research Letters*[J]. 2012;481(7).
- [7] Meng L, Miyajima S. Optically-rough and physically-flat TCO substrates for superstrate-type thin-film solar cells: sol-gel $Zn_{1-x}Mg_xO$ coating on nanoimprint patterned glass substrates. *SOL Energ Mat Sol C*[J]. 2017;161:38-45.
- [8] Michitaka Ohtaki Toshiki Tsubota, Koichi Eguchi and Hiromichi Arai. Thermoelectric properties of Al-doped ZnO as a promising oxide material for high-temperature thermoelectric conversion. *J Mater Chem*[J]. 1997;7(1):85–90.
- [9] Yoshihiro Inoue, Yoichi Okamoto, Jun Morimoto. Thermoelectric properties of porous zinc oxide ceramics doped with praseodymium. *Journal of Materials Science*[J]. 2007;43(1):368-77.
- [10] M. D. McCluskey, S. J. Jokela. Defects in ZnO. *Journal of Applied Physics*[J]. 2009;106(7):071101.
- [11] L. E. Halliburton, N. C. Giles, N. Y. Garces, et al. Production of native donors in ZnO by annealing at high temperature in Zn vapor. *Applied Physics Letters*[J]. 2005;87(17):172108.
- [12] Zhenying Chen, Fei Li, Xiaowei Chen, et al. Influence of sintering temperatures of ceramic targets on microstructures and photoelectric properties of titanium-doped ZnO nano-films. *Journal of Materials Science: Materials in Electronics*[J]. 2016;28(6):4654-60.

- [13] Zayani Jaafar Othman, Adel Matoussi, Filippo Fabbri, et al. Optical and structural properties of $Zn_{1-x}Mg_xO$ ceramic materials. *Applied Physics A*[J]. 2014;116(3):1501-9.
- [14] Tian T, Cheng L, Xing J, et al. Effects of sintering on the microstructure and electrical properties of ZnO-based thermoelectric materials. *Mater Design*[J]. 2017;132:479-85.
- [15] T. Tian, L. H. Cheng, L. Y. Zheng, et al. Defect engineering for a markedly increased electrical conductivity and power factor in doped ZnO ceramic. *Acta Materialia*[J]. 2016;119:136-44.
- [16] H. W. Park, J. H. Bang, K. N. Hui, et al. Characteristics of NiO–AZO thin films deposited by magnetron co-sputtering in an O_2 atmosphere. *Materials Letters*[J]. 2012;74:30-2.
- [17] Dong Huang, Zhifu Liu, Yongxiang Li, et al. Colossal permittivity and dielectric relaxation of (Li, In) Co-doped ZnO ceramics. *Journal of Alloys and Compounds*[J]. 2017;698:200-6.
- [18] David Bérardan, Céline Byl, Nita Dragoie. Influence of the Preparation Conditions on the Thermoelectric Properties of Al-Doped ZnO. *Journal of the American Ceramic Society*[J]. 2010;93(8):2352-8.
- [19] T. C. Damen, S. P. S. Porto, B. Tell. Raman Effect in Zinc Oxide. *Physical Review*[J]. 1966;142(2):570-4.
- [20] Apu Mondal, S. Pal, A. Sarkar, et al. Raman spectroscopic analysis on Li, N and (Li,N) implanted ZnO. *Materials Science in Semiconductor Processing*[J]. 2018;80:111-7.
- [21] Lv J, Li C. Evidences of V_O , V_{Zn} , and O_i defects as the green luminescence origins in ZnO. *Appl Phys Lett*[J]. 2013;103(23):232114.
- [22] Drouilly C, Krafft JM, Averseng F, et al. ZnO Oxygen Vacancies Formation and Filling Followed by in Situ Photoluminescence and in Situ EPR. *J Phys Chem C*[J]. 2012;116(40):21297-307.

- [23] Neeruganti Obularajugari Gopal Chinthala Praveen Kumar, Ting Chung Wang, Ming-Show Wong, and Shyue Chu Ke. EPR Investigation of TiO₂ Nanoparticles with Temperature-Dependent Properties. *J Phys Chem B*[J]. 2006,110:5223-9.
- [24] A. Momot, M. Amini, G. Reekmans, et al. A novel explanation for the increased conductivity in annealed Al-doped ZnO: an insight into migration of aluminum and displacement of zinc. *Physical chemistry chemical physics : PCCP*[J]. 2017;19(40):27866-77.
- [25] Hai Feng, Zhijian Peng, Xiuli Fu, et al. Effect of TiO₂ doping on microstructural and electrical properties of ZnO-Pr₆O₁₁-based varistor ceramics. *Journal of Alloys and Compounds*[J]. 2010;497(1-2):304-7.
- [26] Yu Zhao, Jue Wang, Scott Huxtable, et al. Role of Sintering Atmosphere and Synthesis Parameters on Electrical Conductivity of ZnO. *Energy Harvesting and Systems*[J]. 2015;2(1-2).
- [27] A. Yu Lyashkov, A. S. Tonkoshkur. Varistor composites with a positive temperature coefficient of resistance. *Technical Physics*[J]. 2011;56(3): 427-8.
- [28] M. K. Deore. Studies on Physical and Electrical Characterization of Al₂O₃-ZnO Composite Material and its Thick Films. *International Journal of Science and Research* [J]. 2013;4(11):2240-5.
- [29] Lee Chow Oleg Lupan, Luis K. Ono, Beatriz Roldan Cuenya, Guangyu Chai, Hani Khallaf, Sanghoon Park and Alfons Schulte. Synthesis and Characterization of Ag- or Sb-Doped ZnO Nanorods by a Facile Hydrothermal Route. *J Phys Chem C*[J]. 2010;114:12401-8.
- [30] Felice Friedrich, M. A. Gluba, N. H. Nickel. Identification of nitrogen and zinc related vibrational modes in ZnO. *Applied Physics Letters*[J]. 2009;95(14):141903.
- [31] Zhang R, Yin P, Wang N, et al. Photoluminescence and Raman scattering of ZnO nanorods. *Solid State Sci*[J]. 2009;11(4):865-9.

- [32] J. Serrano, A. H. Romero, F. J. Manjón, et al. Pressure dependence of the lattice dynamics of ZnO: An ab initio approach. *Physical Review B*[J]. 2004;69(9).
- [33] C. V. Pham, S. Repp, R. Thomann, et al. Charge transfer and surface defect healing within ZnO nanoparticle decorated graphene hybrid materials. *Nanoscale*[J]. 2016;8(18):9682-7.
- [34] Taras Kolodiaznyy, Anthony Petric. Analysis of point defects in polycrystalline BaTiO₃ by electron paramagnetic resonance. *Journal of Physics and Chemistry of Solids*[J]. 2003;64:953-60.
- [35] Nobuya IWAMOTO, Hiroaki HIDAKA, Yukio MAKINO. State of Ti³⁺ ion and Ti³⁺-Ti⁴⁺ redox reaction in reduced sodium silicate glasses. *Journal of Non-Crystalline Solids*[J]. 1983;58:131-41.
- [36] Meyer BK, Hofmann DM, Stehr J, et al. Spectral Identification of Impurities and Native Defects in ZnO. USA: John Wiley and Sons Ltd; 2011.
- [37] Anderson J, Chris G. Native Point Defects and Doping in ZnO. USA: John Wiley and Sons Ltd; 2011.
- [38] J. Sann, J. Stehr, A. Hofstaetter, et al. Zn interstitial related donors in ammonia-treated ZnO powders. *Physical Review B*[J]. 2007;76(19).
- [39] Vlasenko L, Watkins G. Optical detection of electron paramagnetic resonance for intrinsic defects produced in ZnO by 2.5-MeV electron irradiation in situ at 4.2 K. *Phys Rev B* [J]. 2005;72(3).
- [40] C. Schilling, M. Záhres, C. Mayer, et al. Aluminum-doped ZnO nanoparticles: gas-phase synthesis and dopant location. *J Nanopart Res*[J]. 2014;16(7).
- [41] Y. S. Avadhut, J. Weber, E. Hammarberg, et al. Structural investigation of aluminium doped ZnO nanoparticles by solid-state NMR spectroscopy. *Physical chemistry chemical physics : PCCP*[J]. 2012;14(33):11610-25.

- [42] Thomas Straube, Jürgen Linders, Thomas Mayer-Gall, et al. Polyol synthesized aluminum doped zinc oxide nanoparticles - influence of the hydration ratio on crystal growth, dopant incorporation and electrical properties. *Materials Today: Proceedings*[J]. 2017;4:S253-S62.
- [43] Rodrigo Noriega, Jonathan Rivnay, Ludwig Goris, et al. Probing the electrical properties of highly-doped Al:ZnO nanowire ensembles. *Journal of Applied Physics*[J]. 2010;107(7):074312.
- [44] R. E. Watson L. H. Bennett, G. C. Carter. Relevance of Knight Shift Measurements to the Electronic Density of States. *JOURNAL OF RESEARCH of the National Bureau of Standards - A Physics and Chemistry*[J]. 1970;74A(4):569-610.
- [45] D. M. Hofmann, A. Hofstaetter, F. Leiter, et al. Hydrogen: a relevant shallow donor in zinc oxide. *Physical review letters*[J]. 2002;88(4):045504.

Chapter 4

Effects of Al doping concentration and sintering methods on ZnO based ceramics

4.1 Introduction

Pure ZnO ceramics have poor electrical conductivity, donor doping is the common way to increase the electrical conductivity of ZnO as this material exhibits an intrinsic n-type behavior. The doping with elements from the group IIIA of the periodic table (X= B, Al, Ga, In) is suitable to act as donors for ZnO, for increasing carrier concentration and electron mobility to get high conductivity^[1-3]. Among all these group IIIA dopants, Al³⁺ is the most commonly used ion due to its non-toxicity, high abundance, environmentally friendly and low cost. Moreover, the ionic radius of Al³⁺ (54 pm) is smaller than that of Zn²⁺ (74 pm)^[4], a high conductivity can be easily achieved from the increase of carriers concentration owing to the Zn²⁺ substituted by Al³⁺ to create shallow donors Al_{Zn}^[5]. Thus, it seems essential to understand the role of Al₂O₃ and its way of regulating the electrical conductivity in ZnO based ceramics. Former works were devoted to explore the electrical behavior and microstructure of Al₂O₃ doped ZnO. Zhang^[6] reported that the maximum electrical conductivity of Al₂O₃-doped ZnO at room temperature was achieved with 0.25 mol% Al₂O₃. Cai et al.^[7] reported that the electrical conductivity (7×10⁴ S·m⁻¹) at room temperature was increased by more than two orders of magnitude by adding 5 mol% Al₂O₃ in ZnO ceramics compared to undoped ZnO. Maeda et al.^[8] found that 2.5 mol% Al₂O₃ in ZnO ceramics can enhance highly the conductivity due to the increasing of carrier concentration and mobility. Our previous work points out that doping 0.25 mol% Al₂O₃ in ZnO ceramics can increase the carrier concentration and mobility of the ceramics, thereby greatly improving the conductivity^[9]. Although shallow donors Al_{Zn} play a crucial role in increasing the conductivity, other phases induced by doping Al₂O₃, such as spinel phase ZnAl₂O₄ and grain boundaries, may decrease conductivity of ZnO based ceramics. Insulating ZnAl₂O₄ particles with a very low conductivity

coexist around the ZnO grains to hinder the transport of carriers^[7, 10]. The Schottky barrier or electron scattering behavior at the grain boundaries impede electron transport, thereby reducing the conductivity^[11, 12]. Despite many reported works about Al₂O₃ doped ZnO materials, the fundamental analysis of the mechanism behind the large modulation of electrical conductivity remains unachieved for Al₂O₃ doped ZnO ceramics. This is the main ambition of the present work to highlight the key parameters acting on the transport phenomena involved in conductive AZO ceramics. Therefore, the main content of this chapter is to study the conductivity changes of AZO conductive ceramics with different Al₂O₃ doping contents, and analyze the key factors that affect the conductivity during the corresponding process.

In Chapter 3, we discussed the effect of sintering atmosphere on the structural defects of Al₂O₃, TiO₂ and MgO co-doped ZnO ceramics. It has been analyzed that the reducing atmosphere can increase the solid solubility of Al³⁺ ions in ZnO and increase the content of shallow donor Al_{Zn}-Zn_i complexes, thereby greatly improving the electrical conductivity of ZnO ceramics. In addition, this reducing sintering atmosphere decreases the intrinsic acceptor defects at the grain boundaries and thus lowers the Schottky barriers. That leads to an increased carrier mobility across the ZnO-ZnO grain boundaries which increase the conductivity of ZnO ceramics^[13, 14]. Considering these two aspects together, N₂+CO appears as a suitable sintering atmosphere for AZO ceramics with the highest conductivity. Therefore, the work in this chapter uses N₂ + CO as the reducing sintering atmosphere to prepare ZnO-based ceramic samples. In order to maintain the coherence of the research work, other dopants TiO₂ and MgO in Chapter 3 were also selected in this chapter along with an optimal doping amount (0.50 mol% of TiO₂ and 1.00 mol% of MgO). ZnO-based ceramics with different components were prepared by changing the doping ratio of the dopant Al₂O₃. Our main aim consists first, in evaluating the optimal doping amount of Al₂O₃ (0.25 mol%) in ZnO ceramics with the highest conductivity at $1.52 \times 10^5 \text{ S} \cdot \text{m}^{-1}$. Secondly, we focus on an exhaustive analysis of the transport mechanism leading to the changing conductivity in AZO ceramics. In particular, a correlation will be made between the transport mechanism with the stabilized crystalline phases, the microstructure of the ceramics along with precise insight of the defect features consecutive to the doping processes.

Moreover, spark plasma sintering (SPS) shows some advantages like rapid sintering and energy conservation, which has been employed to synthesize various high-performance materials, such as $K_{0.5}Na_{0.5}NbO_3$ (KNN) and $MgAl_2O_4$ spinel (MAS)^[14, 15]. According to previous works dealing with the synthesis of ZnO ceramics via SPS, Ma et al. have obtained high dense and homogeneous Al-doped ZnO ceramics where a high electrical conductivity ($\sigma_{RT} = \sim 7 \times 10^4 \text{ S} \cdot \text{m}^{-1}$) is realized with outstanding thermoelectric performances^[16]. Tian et al. have reported that co-doped ZnO ceramics obtained via SPS exhibit a higher electrical conductivity ($\sigma_{RT} = 2.3 \times 10^5 \text{ S} \cdot \text{m}^{-1}$) with high carrier concentration ($2.6 \times 10^{20} \text{ cm}^{-3}$) and a metal-like phenomenon of positive temperature coefficient of resistance has been observed^[12]. Although it is obvious that SPS method play a crucial role in preparing ZnO-based ceramics with high electrical conductivity, the changes on the microstructure of doped ZnO ceramics under SPS method remain not fully understood. Therefore, the effect of the sintering methods on ZnO-based conductive ceramics is also explored in this chapter. ZnO-based ceramics are prepared by a new spark plasma sintering (SPS) method and a traditional muffle furnace sintering method. The differences in microstructure, morphology, vibration, electrical, and optical properties of the corresponding samples are analyzed to establish the correlation between structure and performance.

4.2 Sample preparation and characterization

In this chapter, the effect of the doping concentration of Al_2O_3 on the co-doped ZnO ceramics (Al, Ti, and Mg) oxides in a reducing atmosphere is mainly studied. In addition, the spark plasma sintering (SPS) method is used to prepare Al_2O_3 doped ZnO ceramics, and the evolution of microstructure and electrical properties are explored in comparison with the reducing atmosphere sintering method.

To investigate the role of Al_2O_3 doping concentration on co-doped ZnO ceramics, (98.5-x) mol% ZnO + 0.50 mol% TiO_2 + 1.00 mol% MgO + x mol% Al_2O_3 (x=0.1, 0.25, 0.4, 0.55), referred as “A1”, “A2”, “A3” and “A4” respectively, were prepared

by using the solid-state reaction method. The ZnO raw material powder and all the dopants were weighed according to the designed ratio, and then uniformly mixed by a 6-hour ball milling. The mixed powder was granulated by adding PVA (polyvinyl alcohol) binder and then pressed into pellets with a diameter of 12 mm. After removing PVA binder by annealing at 500 °C for 5 hours, all pellets were sintered under N₂ + CO at 1200 °C for 2 hours.

In order to explore the effect of SPS sintering method on the structure and properties of Al₂O₃ doped ZnO ceramics, Al-doped ZnO samples with the composition 99.75 mol% ZnO + 0.25 mol% Al₂O₃ were prepared by solid state reaction method. The SPS sintering process was performed in a vacuum atmosphere. Under a pressure of 65 MPa, the temperature was raised to a sintering temperature of 1000 °C for 5 minutes to obtain a ceramic sample, which was named “A-SPS”. As a comparison, a ceramic sample “A ”was prepared by using a traditional muffle furnace sintering method and holding the sintering temperature at 1200 °C for 2 hours in a reducing atmosphere (CO + N₂).

The experimental investigations include the electrical properties such as electrical conductivity, temperature coefficient of resistance, carrier concentration, and mobility of the samples measured by using a four-points probe test equipment and a PPMS-9 integrated physical property measurement system. The morphology of the samples was characterized by SEM or TEM methods. The structural defects and electronic active defect of the samples were investigated with Raman, EPR and NMR spectroscopy methods. The operating procedure and test parameters of these experimental methods are detailed in the Chapter 2. In addition, UV-Visible absorption spectra were recorder by using Hitachi U-4100 spectrophotometer, and the photoluminescence spectra (PL spectrum) were obtained by LabRAM HR Evolution at an excitation wavelength of $\lambda = 325\text{nm}$.

4.3 Conduction features in ZnO ceramics

Fig. 4.1a reports the electrical conductivity (σ) of samples A1, A2, A3 and A4. The value of $8.18 \times 10^4 \text{ S}\cdot\text{m}^{-1}$ was obtained in the sample A1, and reaches a maximum of

$1.52 \times 10^5 \text{ S} \cdot \text{m}^{-1}$ for the sample A2. A gradual decrease is therefore noticed for the samples A3 and A4 with $1.35 \times 10^5 \text{ S} \cdot \text{m}^{-1}$ and $4.18 \times 10^4 \text{ S} \cdot \text{m}^{-1}$ respectively. Fig. 4.1b shows the temperature dependence of the conductivity for these samples with common features such as the positive temperature coefficient of resistance (TCR), which infers metal-like behavior of the samples as reported in the chapter 3.

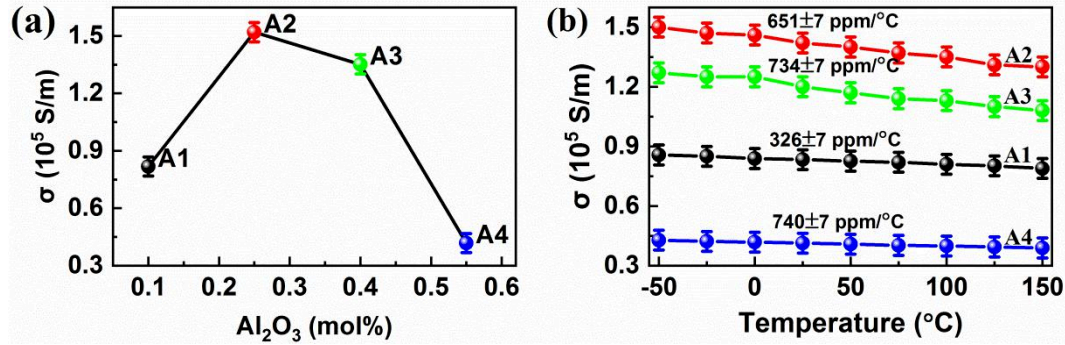


Figure 4.1 (a) Electrical conductivity (σ) and (b) Temperature coefficient of resistance (TCR) for the investigated Ai samples

To understand the electrical transport mechanism, Hall carrier concentration (n) and Hall carrier mobility (μ) were measured by PPMS at room temperature and the results are reported in Fig. 4.2a and Fig. 4.2b respectively. Comparing Fig. 4.1 and Fig. 4.2, the change in σ is coherently consistent with the change in n and μ according to equation 4.1 :

$$\sigma = n e \mu \quad (4.1)$$

However, the main factors affecting the conductivity are related to different Al_2O_3 doping amounts. For A1 and A2 samples, while σ increases dramatically, the relative change of n and μ correspond to 61% and 29% respectively. In consequence, the carrier's density dominates the conduction process of Al_2O_3 with the doping ratio rising from 0.1 mol% to 0.25 mol%. Afterward, σ decreases when the doping amount of Al_2O_3 is further increased to 0.4 mol% as shown for A3 and A4 samples, and the relative variation is 39% and 71% for n and μ . Here, n decreases slightly, while μ exhibits more consistent relationship with the change of σ from A2 to A3 to A4 sample. Thus, carrier mobility is a crucial factor for the conductivity at this stage. It is

then relevant to identify structural defects that affect carrier concentration and mobility, and to explore the causes of the observed behaviors.

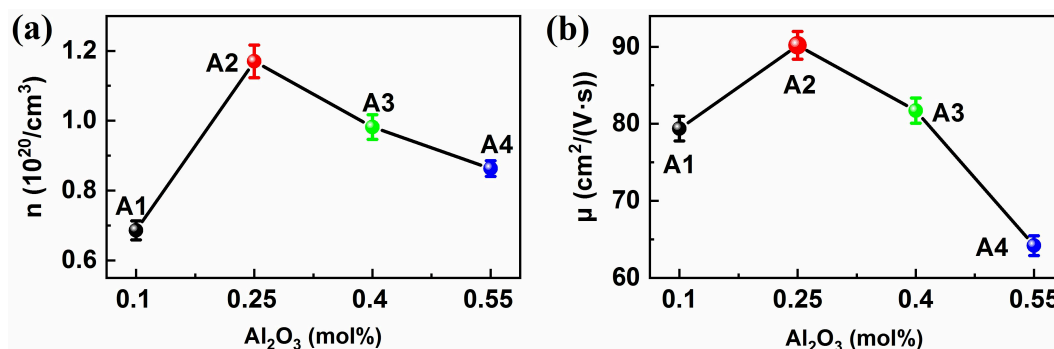


Figure 4.2 (a) Carrier concentration (n) and (b) Carrier mobility (μ) of samples

4.4 Structural and morphology studies

4.4.1 Phase structure analysis

Fig. 4.3 shows the XRD patterns of ZnO doped ceramics with different Al₂O₃ doping ratios. All the patterns point out the main crystalline phase as the hexagonal wurtzite ZnO (JCPDS No. 36-1451). The spinel phases Zn₂TiO₄ and ZnAl₂O₄ are also shown as minor secondary phases. As their content is low, only the main peaks were resolved at 35.3° and 36.8° respectively. These two diffraction lines are related to the same crystallographic plane (113) (Fig. 4.3b). In Fig. 4.3c, the lattice parameters a and c of ZnO show a sharp decrease with doping Al₂O₃ in A1 and A2 samples and then undergo a slight decrease for the samples A3 and A4. This behavior was attributed to the solubility limit of Al₂O₃ which is approximately around 0.25 mol% in ZnO ceramics^[17]. For the same reason of solubility limit, no secondary phases, such as ZnAl₂O₄, were shown in samples A1 and A2 samples. Since the ionic radius of Al³⁺ (0.54 Å) is smaller than that of Zn²⁺ (0.74 Å), the lattice parameters in samples A1 and A2 gradually decrease. With rising the doping ratio, the main peak intensity of ZnAl₂O₄ phase gradually increases in sample A3 and A4 in Fig. 4.3b. As the content of TiO₂ is constant, the amount of Zn₂TiO₄ phase remains the same in all the considered samples. The formation temperature of Zn₂TiO₄ is lower than ZnAl₂O₄,

thus Zn_2TiO_4 is formed in preference to ZnAl_2O_4 during the synthesis process^[18, 19]. Moreover, as Al^{3+} ion (0.54 Å) has a smaller ionic radius than Ti^{4+} ion (0.61 Å), and similar coordination number with Ti^{4+} ion in spinel phase, Al^{3+} can easily substitute Ti^{4+} in Zn_2TiO_4 . Thus the main peak of Zn_2TiO_4 phase shifts slightly to higher 2θ in Fig. 3b and the lattice parameter a of Zn_2TiO_4 decreases in Fig. 4.3d for A1, A2 and A3 with the increasing doping amount of Al_2O_3 , which is in agreement with Zn_2TiO_4 lattice size change. It's worth noting that there is also a solubility limit for Al^{3+} in Zn_2TiO_4 . Indeed, the main peak of Zn_2TiO_4 remains substantially unchanged and the main peak of ZnAl_2O_4 significantly increases for A4 samples. This behavior traduces the formation of ZnAl_2O_4 besides Zn_2TiO_4 with further increase of the Al_2O_3 doping ratio.

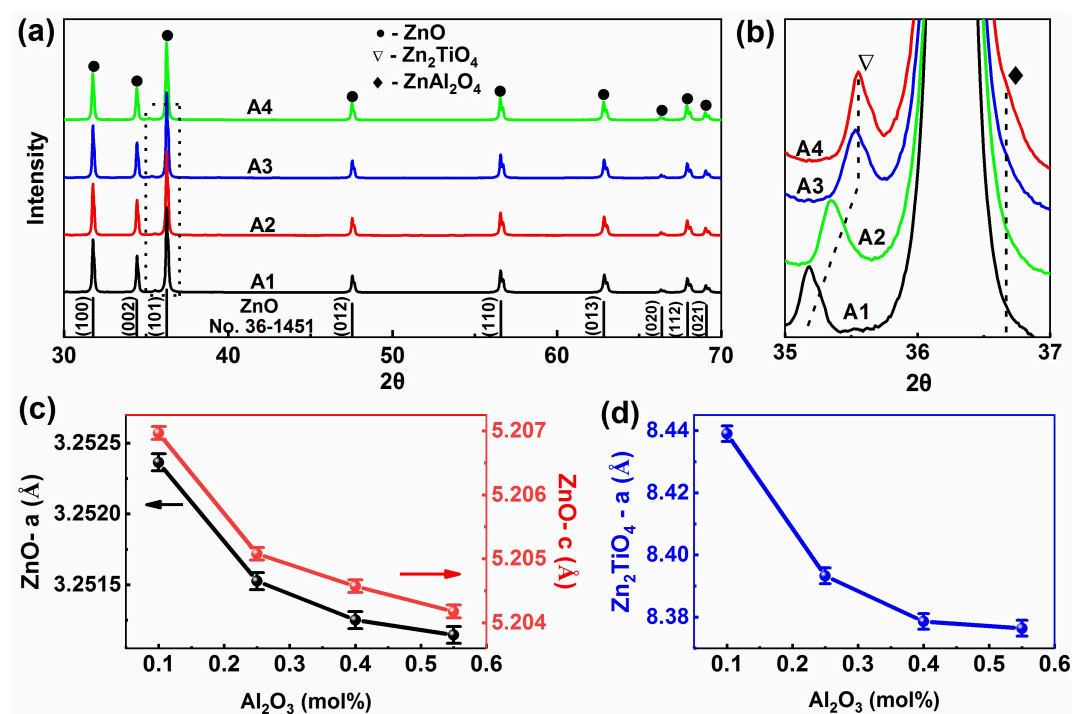


Figure 4.3 (a) XRD patterns of ZnO ceramics with ZnO JCPDS card: No. 36-1451, (b) focus on $2\theta \sim (35^\circ\text{-}37^\circ)$ to highlight the content from spinel phases, (c) (d) Lattice parameters (a and c for ZnO-(c), for Zn_2TiO_4 -(d))

As a donor dopant, Al^{3+} ions substitute to Zn^{2+} in ZnO grains and more carrier electrons are provided to enhance the electrical conductivity. This is illustrated by the electrical behavior in A1 and A2 samples being moderately doped. For higher doping

ratios, Al incorporating into Zn_2TiO_4 or forming spinel phase ZnAl_2O_4 when the doping amount of Al_2O_3 exceeds the solubility limit as in the samples A3 and A4. The spinel phase generated near the grain boundaries and reduced their mobility during the sintering, acting as barriers to weaken the mass transportation and thus prevent the growth of ZnO grains due to the pinning effect. Therefore, it can be preliminarily estimated that sample A2 has the highest electrical conductivity by comprehensive donor defect and the interaction of spinel phase and grain boundaries.

4.4.2 Morphology studies

The SEM images of the ZnO-based ceramic samples are shown in Figure 4.4. Similar features are shown Fig. 4.4a-4.4d and indicate dense microstructures but with different grain sizes. From the energy dispersive X-ray spectroscopy (EDS) analysis depicted in Fig. 4.4e-4.4g, the main phase ZnO shows large grains (Zone A) while spinel phase appears as small dots (Zone B) which are evenly distributed in the samples in Fig. 4.4b, which is consistent with the results of XRD. With the increase of Al_2O_3 content, the grain size gradually decreases from sample A1 to sample A4, indicating that the distribution of spinel phase in ZnO has a pinning effect, controls the growth of ZnO grains, and then increases the number of grain boundaries. In ZnO based ceramics, grain boundaries play an important role in the adjustment of the conductivity. Due to the uneven distribution of defects between grain boundaries and grains, barriers can be formed at the grain boundaries which scatter the electrons to hinder the transport of charge carriers^[20, 21]. Besides, the involved spinel phase ZnAl_2O_4 is an insulator and also scatters electron transport, then limits the effective conductivity of the underlying ZnO ceramics particularly for A3 and A4 samples.

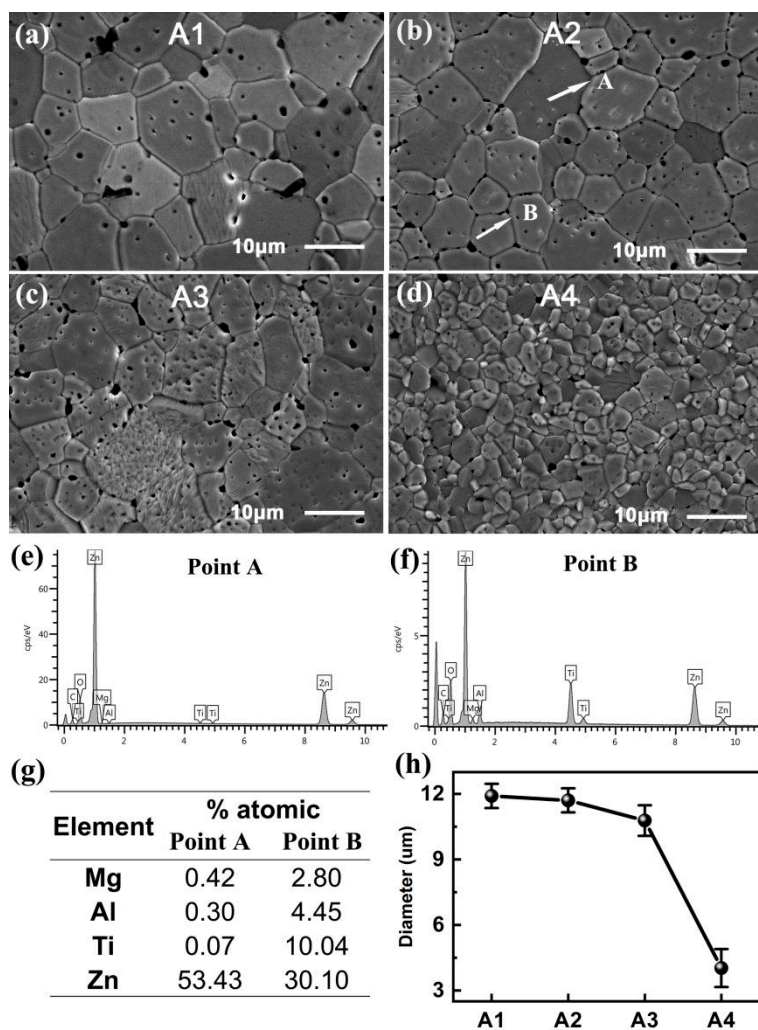


Figure 4.4 SEM images of doped ZnO ceramics (A1-a, A2-b, A3-c, and A4-d), (e) (f) (g) EDS analysis for area 1 and 2 on sample A2, (h) Average diameter of samples

Fig. 4.5 shows the TEM images of ZnO based ceramics (A1, A2, A3 and A4), with an emphasis on the zone of grain boundaries between two grains of ZnO or spinel phase. All these images possess similar features, namely a clear grain boundary with distinct lattice fringes. This fact underlines that two grains are combined very well without thin layer amorphous phases like in ZnO varistors^[22]. In other words, the spinel structure acts as an independent secondary phase particles distributed in ZnO or between adjacent ZnO grains.

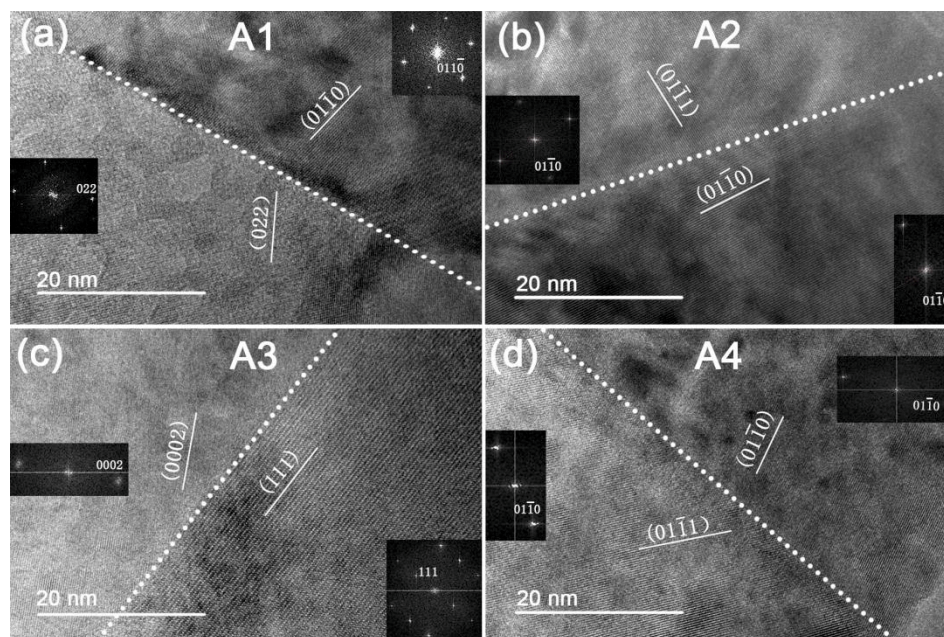


Figure 4.5 TEM images of samples with the corresponding fast Fourier transform (FFT) patterns of neighboring grains

4.5 Vibrational signatures of doped ZnO based ceramics

Raman spectroscopy was applied to investigate microscopic defect structures in ceramics that affect electrical conductivity. The Raman spectra shown in Fig. 4.6 were first normalized to the E_2^{high} peak chosen as a reference and the lines were fitted as shown in all samples. All the Raman modes and their combination modes reported for ZnO wurtzite structure^[2, 23] are related to $E_2^{\text{low}} = 105 \text{ cm}^{-1}$, $E_2^{\text{high}} = 443 \text{ cm}^{-1}$, $A_1(\text{TO}) = 382 \text{ cm}^{-1}$, $A_1(\text{LO}) = 574 \text{ cm}^{-1}$, $E_1(\text{TO}) = 415 \text{ cm}^{-1}$, $E_1(\text{LO}) = 584 \text{ cm}^{-1}$, $2\text{TA} = 208 \text{ cm}^{-1}$, $E_2^{\text{high}} - E_2^{\text{low}} = 340 \text{ cm}^{-1}$, $\text{TO} + \text{LO} = 1090 \text{ cm}^{-1}$ and $2\text{LO} = 1150 \text{ cm}^{-1}$ respectively. The peak at about 735 cm^{-1} is assigned to A_{1g} mode involved in the minor spinel phase Zn_2TiO_4 ^[24]. E_2^{low} mode is related to the vibration of heavy Zn sublattice, whereas the E_2^{high} mode refers to the vibration of oxygen atoms. These two active modes are characteristic signatures of the wurtzite structure ZnO^[25]. No particular shift or broadening was observed in all characteristic peaks. $A_1(\text{TO})$ Raman mode at 382 cm^{-1} is related to oxygen vacancies (V_{O}) in ZnO, which holds the strongest intensity in sample A2 among this four samples. However, V_{O} is a deep donor in ZnO

with transition level at ~ 1.0 eV below the bottom of the conduction band, which means that V_O is not a suitable candidate for improving n-type conductivity^[26]. The Raman mode $A_1(\text{LO})$ at 574 cm^{-1} is associated with interstitial zinc (Zn_i). A broad peak at about 500 cm^{-1} , considered as B_1 mode related to local disordered structures, dominates in sample A2. This broad peak is a characteristic of defects created in the host crystal lattice. In the samples, these defects breaking of local translational symmetry to induce broad peak are mainly Al_{Zn} and Zn_i ^[13, 27].

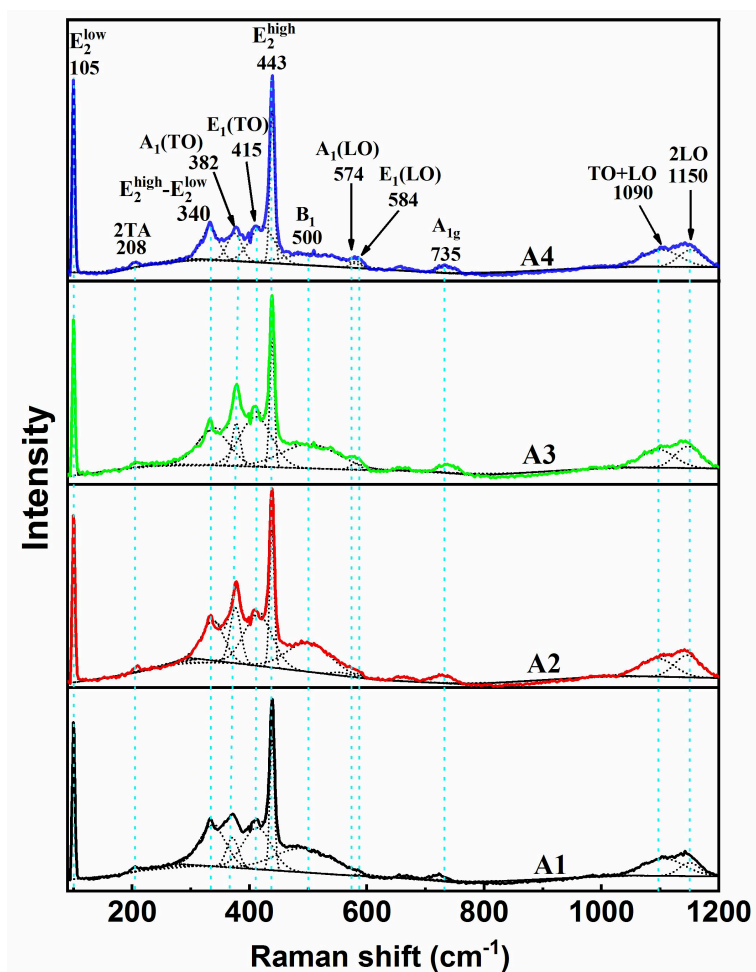


Figure 4.6 Raman spectra of samples

For Al-doped ZnO, Al^{3+} substitutes Zn^{2+} to form Al_{Zn} accompanied by the creation of Zn_i , thus $\text{Al}_{\text{Zn}}\text{-Zn}_i$ complexes are generated^[28]. $\text{Al}_{\text{Zn}}\text{-Zn}_i$ complexes with the charge state +1 has Fermi levels close to the conduction band minimum, which can increase the number of charge carriers and lead to an increasing conductivity. Thus, sample A2

with the strongest intensity of B_1 mode has the highest electrical conductivity. With the doping amount increasing, a larger amount of the secondary phase was produced to improve the overall crystallization, thus the broad peaks at 500 cm^{-1} of A3 and A4 become weaker. Through the Raman study, $\text{Al}_{\text{Zn}}\text{-Zn}_i$ complex is considered to be the main exact factor, rather than Al_{Zn} alone, leading to an increase in carrier concentration and an increase in conductivity when increasing the Al_2O_3 content to 0.25 mol%.

4.6 Local order probing of Al doping ions

Al doping greatly increases the electrical conductivity of ZnO ceramics due to the formation of shallow donors in microstructure. To probe the ^{27}Al nuclei in the ZnO lattice and to further determine their local environments, samples were characterized by solid state NMR. ^{27}Al is a spin 5/2 nucleus and is therefore quadrupolar, thus ^{27}Al nuclei can be probed in this experiment to determine its local environments. As shown in Fig. 4.7a, ^{27}Al MAS NMR characteristic spectra of different ZnO ceramics are obtained and indicate three different environments for Al nuclei in all ZnO based samples corresponding to three lines at 0, 80 and 185 ppm respectively. The sum of intensity of these three lines is proportional to the Al_2O_3 doping amount as shown in Fig 4.7b, confirming that the amount of the total Al in ceramics is increasing. The line at 0 ppm is related to six-fold oxygen coordinated Al and almost proportional to Al_2O_3 doping amount in Fig. 4.7b. The Al nuclei in octahedral interstitial sites of ZnO (Fig. 4.8a) and in Al lattice sites of ZnAl_2O_4 are six-fold oxygen coordination, thus this peak at 0 ppm is associated with the amount of Al in interstitial sites of ZnO and in the lattice Al-site of ZnAl_2O_4 . For samples A1 and A2, the Al_2O_3 doping amount is within the solubility limit, most six-fold oxygen coordinated Al exists in the form of octahedral interstitial sites of ZnO. The amount of ZnAl_2O_4 is gradually increased in A3 and A4 with the further increase of doping amount of Al_2O_3 . At this point, most of the 0-ppm line intensity is provided by the lattice Al-site of ZnAl_2O_4 . Besides, the line at 80 ppm is related to the four-fold oxygen coordinated Al present as substitutional defect (Al_{Zn}) in Zn sites (Fig. 4.8b), with almost the same amount for all samples. This further indicates that although Al substitutes to Zn forming a donor dopant, it does not only exist in the form of Al_{Zn} with four-coordinated oxygen. Moreover, the

line at 185 ppm cannot be related to pure oxygen coordinated Al because it is far out of the usual chemical shift range. The signal was considered as Knight shift effect or active electronic defects from $\text{Al}_{\text{Zn}}\text{-Zn}_i$ complexes shown as Fig. 4.8c. The complexes consist in defect pairs formed by substitutional Al_{Zn} and interstitials Zn_i . This gives rise to extended charge distribution leading to the high achieved conductivity and ensuring the basis of the Knight shift at the 185 ppm NMR line. Therefore, $\text{Al}_{\text{Zn}}\text{-Zn}_i$ complexes can contribute to increase the carrier concentration in ZnO based ceramics and then improve the conductivity.

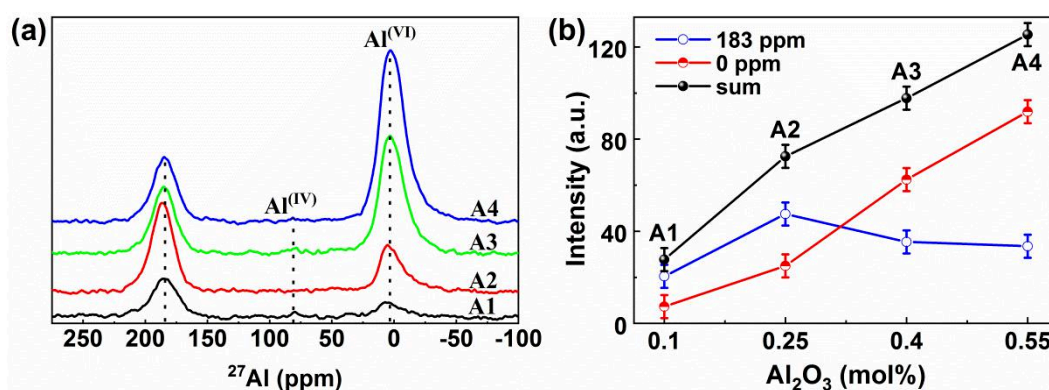


Figure 4.7 (a) ^{27}Al MAS NMR spectra of different samples. (b) The peak spectra intensities at 0 ppm, 185 ppm and the sum for samples

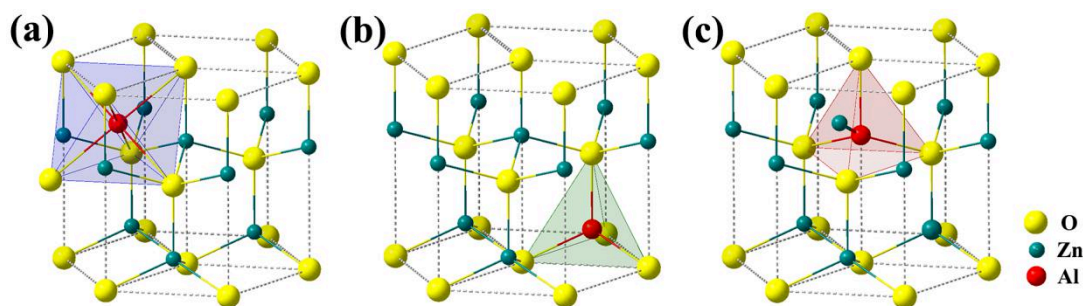


Figure 4.8 Schematic diagram of the environment of Al in ZnO: (a) Interstitial Al^{3+} (Al_i), (b) Substitutional Al^{3+} (Al_{Zn}), (c) Substitutional Al^{3+} - Interstitial Zn^{2+} ($\text{Al}_{\text{Zn}}\text{-Zn}_i$)

Fig. 4.9 shows the relation diagram between electrical conductivity and the intensity of NMR-185ppm line, which shows a proportionality relationship in samples A1, A2 and A3. However, the sample A4 does not comply with this behavior due to wide area of grain boundaries and an insulating ZnAl_2O_4 spinel limiting the conductivity. These

effects overcame the occurrence of extended electronic density around $\text{Al}_{\text{Zn}}\text{-Zn}_i$ complexes. Thus, $\text{Al}_{\text{Zn}}\text{-Zn}_i$ complexes are clearly correlated with the electrical conductivity and account for the 185-ppm line. As shown in Fig. 4.9, the intensity of the 185-ppm peak of sample A2 with the highest conductivity reaches the maximum, which means that compared with other samples, the Knight shift effect of sample A2 is the strongest due to a higher concentration of $\text{Al}_{\text{Zn}}\text{-Zn}_i$ complexes.

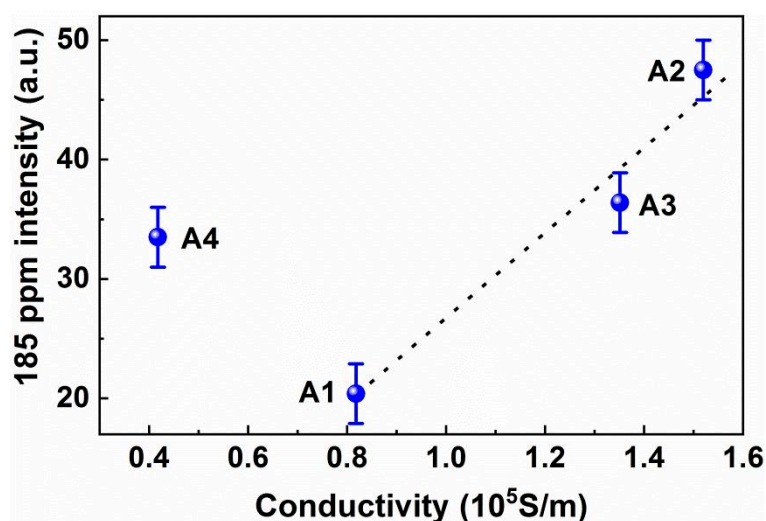


Figure 4.9 Relation between the sample conductivity and the intensity of NMR-185ppm peak

The performed experiments of Al_2O_3 doping amount in ZnO-based ceramics show that the highest conductivity of ZnO ceramics was obtained at the optimal Al_2O_3 doping amount of 0.25 mol%. In addition, the origin of the large change in the ceramic conductivity caused by different Al_2O_3 doping amounts was attributed to the formation of $\text{Al}_{\text{Zn}}\text{-Zn}_i$ complexes. The results show also that the critical role played by ZnO grain boundaries and the insulating spinel phases to limit the electrical conductivity of ZnO-based ceramics. In the same context, the sintering method of the ceramic preparation process influences also the structural features and the electrical performances. Therefore, the next section compares the influence of the main sintering method used in this thesis - Muffle Furnace Sintering and new sintering method - Spark Plasma Sintering on the structural and conduction properties of Al_2O_3 -doped ZnO conductive ceramics.

4.7 Spark Plasma Sintering of Al doped ZnO

Al₂O₃ doped ZnO ceramic samples **A** and **A-SPS** were prepared by the conventional Muffle Furnace Sintering method and the new Spark Plasma Sintering (SPS) method, respectively. The differences in the structure features, microstructures and electrical performances of the ceramics prepared by the two sintering methods are compared. The mechanism of improving the performances of Al₂O₃-doped ZnO high-conductive ceramics by plasma sintering was discussed.

4.7.1 Structural and morphology studies

The XRD patterns of the sample A-SPS and A are shown in Fig. 4.10. The two diffraction patterns exhibit the features of hexagonal wurtzite ZnO (JCPDS No. 36-1451). However, the secondary phase of ZnAl₂O₄ cannot be observed in sample A-SPS, but appears in sample A, indicating that more Al elements are introduced into ZnO host lattice instead of contributing to the spinel phase formation. The vacuum condition during SPS process may provide an environment with low oxygen partial pressure, leading to the further reaction of Al substitution into Zn sites. Moreover, due to the applied high DC current, the rapid diffusion of Al atoms leads to the formation of solid solution instead of the ZnAl₂O₄ spinel phase. Therefore, the SPS method improves the solid solubility of Al in ZnO.

Fig. 4.11 shows the grain morphologies of the polished and thermal etched sample A-SPS and A observed by the scanning electron microscope (SEM). Both samples exhibit the dense structure with few pores. However, there is a great difference in the average grain size, with 1.6 μm for the sample A-SPS and 8.8 μm for the sample A. Spark plasma sintering induces a significant limitation of ZnO grain growth, which is attributed to the rapid sintering process along with a low sintering temperature and pulsed DC current. It is worth noting that the rapid sintering generates a porosity in the sample A-SPS.

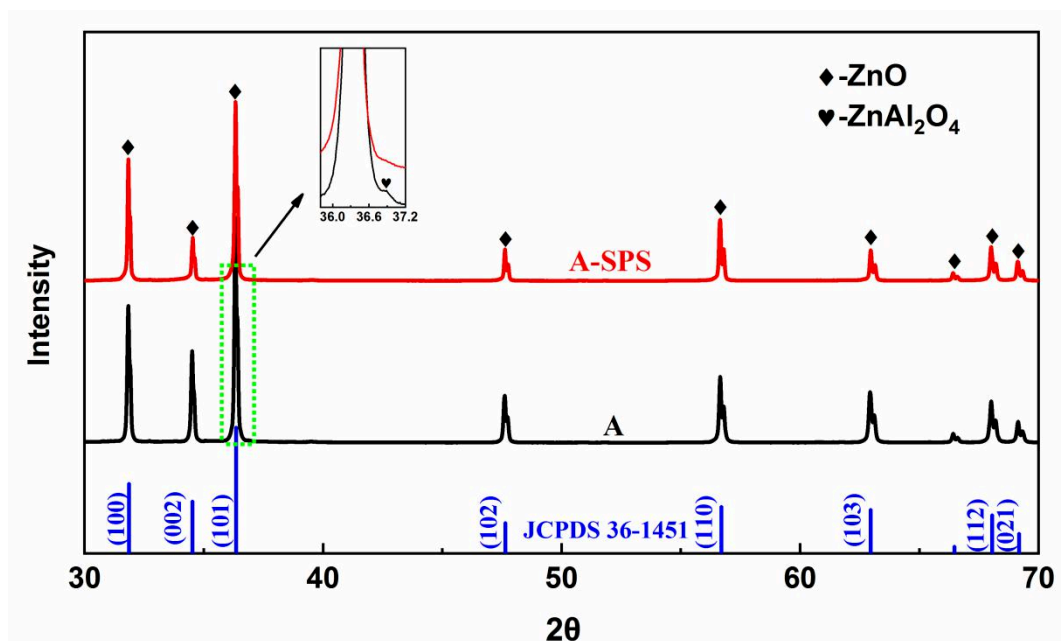


Figure 4.10 XRD patterns of A-SPS and A samples

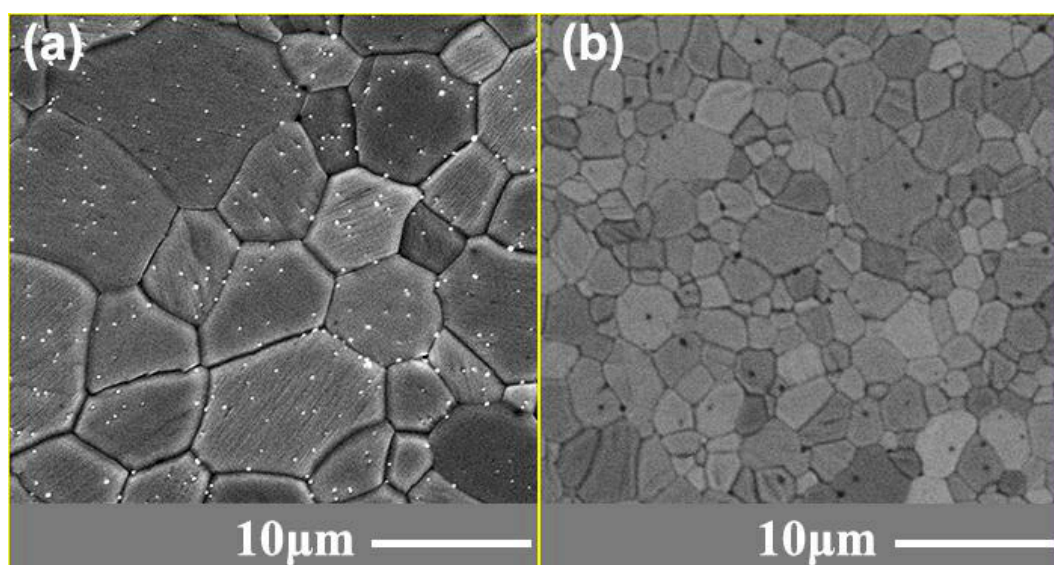
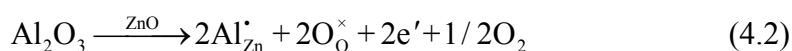


Figure 4.11 SEM images of sample A (a) and A-SPS (b)

4.7.2 Conduction features

The electrical conductivities of the samples A-SPS and A, including the carrier concentrations (n) and hall mobilities (μ), are shown in Fig. 4.12. It is noticed that the sample A-SPS exhibits a higher electrical conductivity ($3.0 \times 10^5 \text{ S} \cdot \text{m}^{-1}$), a higher

carrier concentration ($1.3 \times 10^{21} \text{ cm}^{-3}$) but a lower hall mobility ($14.3 \text{ cm}^2 \cdot \text{V}^{-1} \cdot \text{s}^{-1}$), compared with the sample A. This phenomenon indicates that the increase of the conductivity of the sample A-SPS is mainly related to the increase of the carrier concentration. The increase of the Al incorporation concentration in ZnO by using SPS method can provide more charge carriers according to the following reaction (Equation. 4.2):



However, the lower hall mobility is related to the smaller grain size obtained by SPS, the smaller grain size means more grain boundaries, and the high quantity of grain boundaries hinder the electronic transport. Therefore, according to the relation $\sigma = ne\mu$, it can be concluded that the higher electrical conductivity of the sample A-SPS originates from the significant increase in charge carrier's concentration.

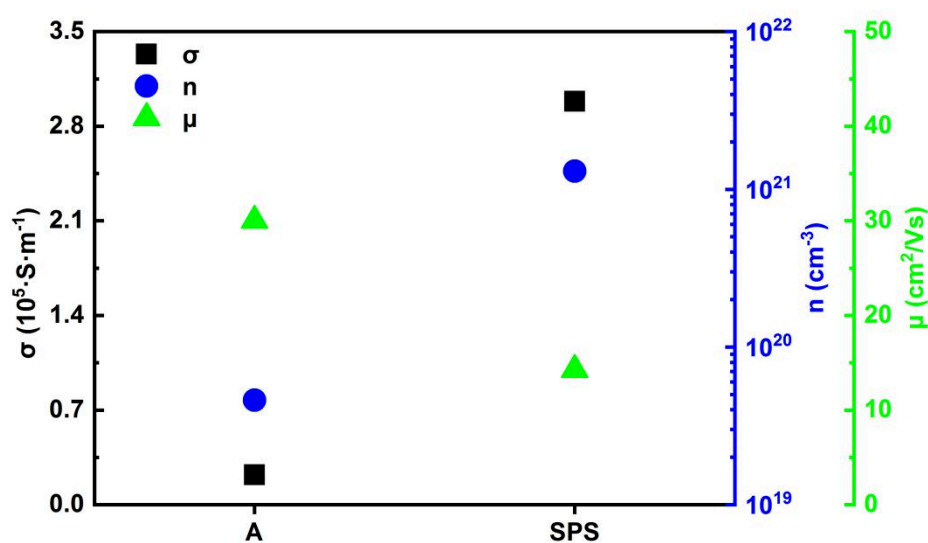


Figure 4.12 Electrical conduction properties for A-SPS and A samples

4.7.3 Raman spectra studies

The difference in the lattice vibration characteristics between samples A-SPS and A can be detected by Raman spectroscopy. Figure 4.13 shows the room temperature

Raman spectra of samples A-SPS and A measured in the range of 100 to 1200 cm^{-1} . Compared to the sample A, A-SPS shows some significant changes in Raman spectra. The E_2^{high} peak, which is sensitive to the crystalline quality, exhibits a slight shift and decrease in intensity, indicating that more structural defects in sample A-SPS are induced into the ZnO lattice^[29]. The B_1 peak, which is silent in a perfect crystalline structure but can be activated in a disordered structure, shows an obvious increase of its intensity as a consequence of the occurrence of structural distortion. These two Raman modes point out the effect of disorder and structural defects induced by the Al substitution into Zn sites. Moreover, the $A_1(\text{LO})$ and $E_1(\text{LO})$ modes, which correlate with intrinsic defects in host lattice, like oxygen vacancy (V_{O}) and zinc interstitial (Zn_{i}), have a vanishing intensity. That means that the larger amount of intrinsic defects with expected lattice disorder suppressed these two modes^[30, 31]. These features can finally manifest that, under the SPS condition, further incorporation of Al elements and further formation of intrinsic defects enhance the structural distortion in ZnO lattice.

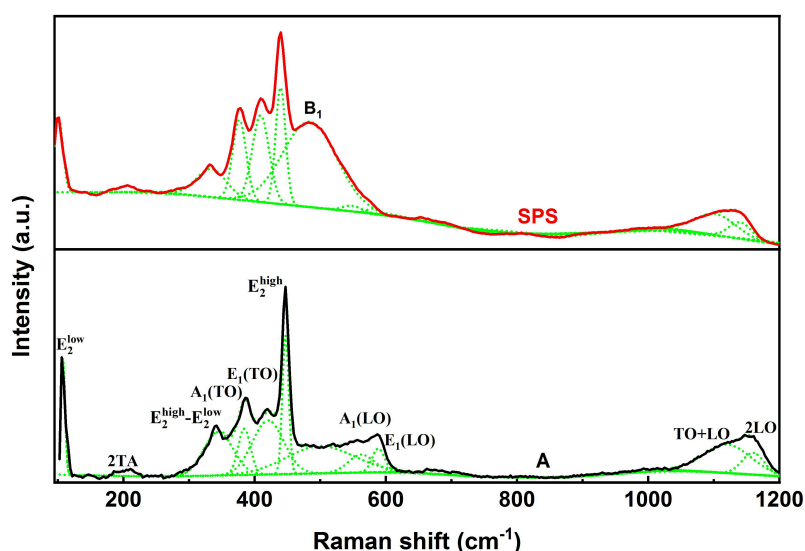


Figure 4.13 Raman spectra for sample A-SPS and A

4.7.4 UV-Vis Absorption spectra and Photoluminescence studies

It is well established that the optical absorption or emission processes reflect the

features of the electronic structure and charge recombination processes. Optical methods are then relevant to compare informations on the electronic properties between A-SPS and A samples. The differences in UV-vis absorption spectra between sample A-SPS and A are shown in Fig. 4.14. Both samples exhibit the similar optical absorption behavior in the wavelength range from 200 - 1200 nm. A sharp decrease is shown on the absorbance spectra at shoulder peak near 385 nm, which is related to the optical band gap. Compared with sample A, the absorption edge of the sample A-SPS exhibits a slight blue shift, indicating the broadening of optical band gap. More details can be displayed by the relation between the absorption coefficient α and the photon energy $h\nu$ by using the Tauc plot given by the equation. 4.3^[32].

$$\alpha h\nu = B(h\nu - E_g)^n \quad (4.3)$$

Here, B is a constant, E_g is the band gap and n depends on the type of transition. Thus, $n = 0.5$ for the allowed direct transition type, 1.5 for forbidden direct transition type, 2 for indirect transition type and 3 for forbidden indirect transition type. With the allowed direct band transition type in wurtzite ZnO ($n=0.5$), the Tauc plots curves are shown in the inset of Fig. 4.14. From the intersection, the optical band gap is found to be 3.38 eV and 3.34 eV, for A-SPS and A sample respectively. The blue shift and the increase in optical band gap is attributed to the Burstein-Moss effect^[33], which implies that there are more free electrons occupying the bottom of the conduction band in sample A-SPS than that in sample A, in agreement with further incorporation of Al in the A-SPS lattice. Furthermore, the absorption in the visible and IR region is more strong for the sample A-SPS compared to the sample A. This effect is considered to be related to electronic states within the band gap induced by Al impurities^[33]. Such allowed electronic states are easily promoted in the conduction band with a higher concentration in the sample A-SPS, compared to the sample A. Therefore, further incorporation of Al elements inducing a higher carrier concentration are proved in the absorption study in agreement with XRD and electrical conduction results.

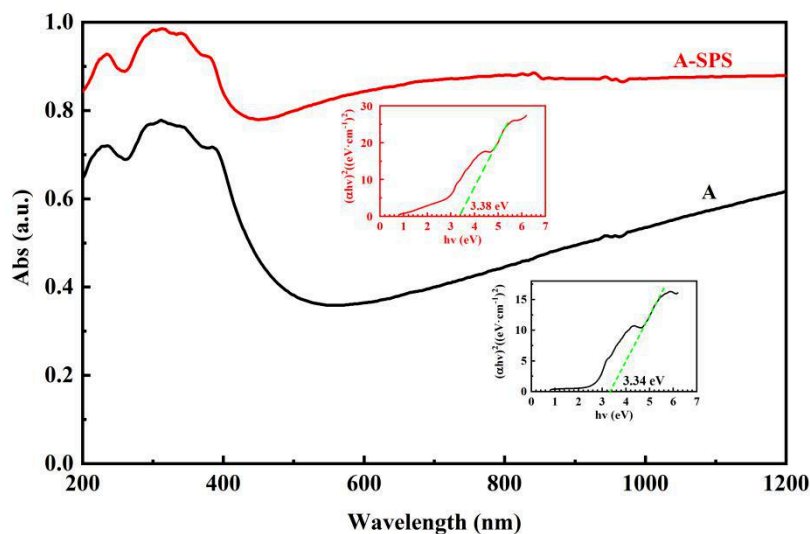


Figure 4.14 UV-vis absorption spectra for sample A-SPS and A, the inset shows curves between $(ah\nu)^2$ versus $h\nu$

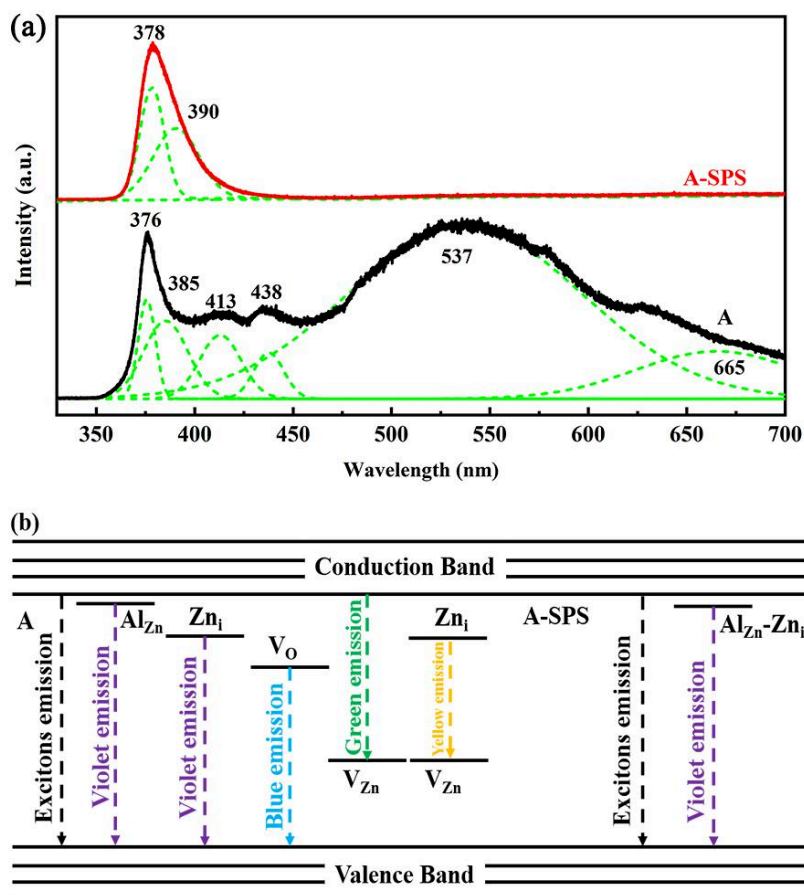


Figure 4.15 (a) Photoluminescence spectra for sample A-SPS and A, (b) Energy level diagram of the defects corresponding to the spectra

Photoluminescence (PL) spectroscopy for both samples A-SPS and A have been

measured at room temperature with the excitation light of 325 nm and the spectra are presented in Fig. 4.15a. For both samples, PL spectra consist in two emission bands, one is related to UV emission and the other one is related to deep level emission. The UV emission peak located at around 375 nm, originates from the transition of excitons and is named near band edge (NBE) emission. In visible region, deep level emission is attributed to the intrinsic structural defects, like zinc interstitials (Zn_i) or oxygen vacancies (V_O) as donor defects and zinc vacancies (V_{Zn}) or oxygen interstitials (O_i) as acceptor defects. These defects can become luminescent centers after suitable excitation. As shown for sample A, the peak at 389 nm is due to the shallow donor Al_{Zn} level according to DFT calculation. The violet emission located at 413 nm is considered to be related to electron transition from Zn_i level to the top of valence band (VB)^[34]. Then, the transition from a single ionized V_O level to the top of VB is responsible for the blue emission at 435 nm^[35]. A broad green emission is found at 535 nm, which is generally attributed to the transition from the bottom of conduction band (CB) to some deep acceptor level like V_{Zn} and O_i ^[36, 37]. Due to the high formation energy of O_i , it is more likely that V_{Zn} acts as the luminescence center^[38]. At 665 nm, the yellow emission peak is assigned the transition from the donor Zn_i level to the deep acceptor level V_{Zn} . However, for the sample A-SPS, the PL spectrum becomes simple with the disappearance of the green emission peak. To some extent, the intensity of the emission peak corresponds to the concentrations of defects. Therefore, the vanishing of the green emission implies evidently a lower concentration of the intrinsic acceptor defects. Moreover, for the asymmetrical UV emission peak, it is thought to be the combination of two emission peaks: one from NBE emission while the other from the shallow donor levels which are very close to the conduction band^[39]. Such shallow donor levels are considered to be related with Al impurities^[33]. Noted that the peaks represented Zn_i and V_O have been almost disappeared and it is inconsistent with the results that intrinsic donor defects suppress the $A_1(LO)$ and $E_1(LO)$ modes in Raman spectra. Therefore, these donor defects may combine with Al-doped defects as defect complexes, which corresponds to the

shallow donor level. $\text{Al}_{\text{Zn}}\text{-Zn}_i$ complexes in co-doped ZnO ceramics are associated with the high conduction properties by EPR and NMR results in the former result. Hence, it is rational to consider that $\text{Al}_{\text{Zn}}\text{-Zn}_i$ complexes radiate violet emission in the PL spectra. The corresponding diagrams of the luminescence emission for sample A-SPS and A are shown in Fig. 4.15b. From this diagram, it is clear that the $\text{Al}_{\text{Zn}}\text{-Zn}_i$ complexes act as the only donor to provide electrons to the conduction band and its level is slightly closer to the conduction band than Al_{Zn} level, which implies that it can associate with the obtained huge electrical conductivity. To summarize, these changes in PL spectra between sample A-SPS and A support that, $\text{Al}_{\text{Zn}}\text{-Zn}_i$ complexes appear with the increased Al doping concentration and finally enhance the electrical conduction properties by using SPS method.

4.8 Conclusion

1. When the content of dopant Al_2O_3 increases from 0.1 mol% to 0.55 mol%, the electrical conductivity of ZnO ceramics increases first followed by an upward decrease due to the solubility limit. An optimal Al_2O_3 about 0.25 mol% ensure the highest conductivity up to $1.52 \times 10^5 \text{ S}\cdot\text{m}^{-1}$ in Al doped ZnO-based ceramics.
2. The solid solubility of Al_2O_3 in ZnO was evaluated to 0.25 mol%. As the doping amount of Al_2O_3 increases, the substitution of Al ions in the ZnO lattice is privileged. For moderate doping ratios exceeding the solubility limit, the incorporation of Al begins to be effective in Zn_2TiO_4 lattice. For higher doping ratios the excess Al ions will react with ZnO to form a ZnAl_2O_4 spinel phase distributed between ZnO grains. The spinel phase acts as a pinning to limit the growth of ZnO grains, thereby increasing the number of grain boundaries.
3. Raman, EPR and NMR experiments have confirmed that shallow donor $\text{Al}_{\text{Zn}}\text{-Zn}_i$ complexes are involved with highly delocalized electronic charge density distributions leading to high conductivity. Grain boundaries in ZnO ceramics and insulating ZnAl_2O_4 spinels overcome the charge carrier transport limiting drastically the carrier mobility and the network conductivity.
4. Al-doped ZnO ceramics have been synthesized by SPS and conventional

sintering method respectively. SPS is revealed as an effective method to highly enhance the conduction properties of ZnO-based ceramics. XRD and SEM results reveal that SPS annealed doped ZnO ceramics are characterized by a higher solid solubility of Al in ZnO and smaller grains. The corresponding ceramics exhibit a higher electrical conductivity ($\sigma_{RT} = 3.0 \times 10^5 \text{ S}\cdot\text{m}^{-1}$) due to carrier concentration as high as ($1.3 \times 10^{21} \text{ cm}^{-3}$). From Raman studies, the variety of E_2^{high} peak and the higher intensity of activated B_1 mode point out the existence of structural distortions with the Al impurities and more disordered structure in the SPS annealed samples. UV-vis absorption spectra show the broadening of optical band gap induced by Al incorporation in the host lattices. Photoluminescence spectra are analyzed coherently by the involvement of $\text{Al}_{\text{Zn}}\text{-Zn}_i$ complexes with a higher concentration when the Al doping ratios increase. These results reflect also the changes in the microstructure of Al-doped ZnO ceramics with more Al incorporation into ZnO host lattice by using the SPS method which also induces the highest achieved conductivity in Al doped ZnO-based ceramics.

4.9 Reference

- [1] Diana T. Alvarez-Ruiz, Feridoon Azough, David Hernandez-Maldonado, et al. Enhancement of Electrical Conduction and Phonon Scattering in $\text{Ga}_2\text{O}_3(\text{ZnO})_9\text{-In}_2\text{O}_3(\text{ZnO})_9$ Compounds by Modification of Interfaces at the Nanoscale. *Journal of Electronic Materials*[J]. 2018;48(4):1818-26.
- [2] M.S. Jang, M.K. Ryu, M.H. Yoon, et al. A study on the Raman spectra of Al-doped and Ga-doped ZnO ceramics. *Current Applied Physics*[J]. 2009;9:651-7.
- [3] Vladimir I. Brinzari, Alexandr I. Cocemasov, Denis L. Nika, et al. Ultra-low thermal conductivity of nanogranular indium tin oxide films deposited by spray pyrolysis. *Applied Physics Letters*[J]. 2017;110(7).
- [4] Hequn Dai, Hao Xu, Yongning Zhou, et al. Electrochemical Characteristics of Al_2O_3 -Doped ZnO Films by Magnetron Sputtering. *The Journal of Physical Chemistry C*[J]. 2012;16(1):1519-25

- [5] T. Tian, L. H. Cheng, L. Y. Zheng, et al. Defect engineering for a markedly increased electrical conductivity and power factor in doped ZnO ceramic. *Acta Materialia*[J]. 2016;119:136-44.
- [6] Yongheng Zhang, Juan Han. Microstructure and temperature coefficient of resistivity for ZnO ceramics doped with Al₂O₃. *Materials Letters*[J]. 2006; 60:2522–5.
- [7] K. Cai, E. Müller, C. Drašar, et al. Preparation and thermoelectric properties of Al-doped ZnO ceramics. *Mater Sci Eng B-Adv*[J]. 2003;104(1-2):45-8.
- [8] H. Maeda, Y. Nakao, K. Tsuchida, et al. Thermoelectric Properties of ZnO-Al₂O₃ Ceramics. 17th International Conference on Thermoelectrics[J]. 1998.
- [9] Qianying Sun, Tian Tian, Laoying Zheng, et al. Electronic active defects and local order in doped ZnO ceramics inferred from EPR and ²⁷Al NMR investigations. *Journal of the European Ceramic Society*[J]. 2019;39(10): 3070-6.
- [10] H. Kaga, Y. Kinemuchi, H. Yihnaz, et al. Orientation dependence of transport property and microstructural characterization of Al-doped ZnO ceramics. *Acta Materialia*[J]. 2007;55(14):4753-7.
- [11] T. Tian, L. Zheng, X. Ruan, et al. Disorder-induced localization in doped ZnO by different sintering atmosphere. *Ceram Int*[J]. 2018.
- [12] Tian T, Cheng L, Xing J, et al. Effects of sintering on the microstructure and electrical properties of ZnO-based thermoelectric materials. *Mater Design*[J]. 2017;132:479-85.
- [13] Q. Sun, T. Tian, L. Zheng, et al. Electronic active defects and local order in doped ZnO ceramics inferred from EPR and ²⁷Al NMR investigations. *J Eur Ceram Soc*[J]. 2019;39(10):3070-6.
- [14] Micka Bah, Fabien Giovannelli, Frédéric Schoenstein, et al. High electromechanical performance with spark plasma sintering of undoped K_{0.5}Na_{0.5}NbO₃ ceramics. *Ceramics International*[J]. 2014;40(5):7473-80.

- [15] Annika Pille, Hugo Spiridigliozzi, Mohamed Amamra, et al. Morphology and luminescence of MgAl_2O_4 ceramics obtained via spark plasma sintering. *Ceramics International*[J]. 2019;45(7):8305-12.
- [16] N. Ma, J. F. Li, B. P. Zhang, et al. Microstructure and thermoelectric properties of $\text{Zn}_{1-x}\text{Al}_x\text{O}$ ceramics fabricated by spark plasma sintering. *Journal of Physics and Chemistry of Solids*[J]. 2010;71(9):1344-9.
- [17] Keita SHIROUZU, Takahiro OHKUSA, Mikinori HOTTA, et al. Distributuon and solubtily limit of Al in Al_2O_3 -doped ZnO sintered body. *Journal of the Ceramic Society of Japan*[J]. 2007;115(4):254-8.
- [18] E. N. Bunting. Phase Equilibria in the System $\text{ZnO-Al}_2\text{O}_3$. *Journal of research of the National Bureau of Standards* [J]. 1932;8:279-87.
- [19] F. H. Dulin, D. E. Rase. Phase Equilibria in the System ZnO-TiO_2 . *Journal of the American Ceramic Society*[J]. 1960;43:125-31.
- [20] Minge Chen, Qian Liu, Jianfeng Zhu, et al. Effect of ZnAl_2O_4 content on the microstructure and electrical properties of ZnO-based compound conductive ceramics. *Journal of Alloys and Compounds*[J]. 2018;750: 213-9.
- [21] T. K. GUPTA, W. G. CARLSON. A grain-boundary defect model for instability/stability of a ZnO varistor. *JOURNAL OF MATERIALS SCIENCE*[J]. 1985;20:3487-500.
- [22] Kei-Ichiro Kobayashi, Osamu Wada, Masahiro Kobayashi, et al. Continuous existence of Bismuth at grain boundaries of Zinc Oxide varistor without intergranular phase. *J Am Ceram Soc*[J]. 1998;81(8): 2071-76.
- [23] J. Serrano, A. H. Romero, F. J. Manjón, et al. Pressure dependence of the lattice dynamics of ZnO: Anab initioapproach. *Physical Review B*[J]. 2004;69(9).
- [24] Liang Li, Shuohui Gao, Tian Cui, et al. Temperature-dependent optical phonon behaviour of a spinel Zn_2TiO_4 single crystal grown by the optical

- floating zone method in argon atmosphere. RSC Advances[J]. 2017;7(56): 35477-81.
- [25] Luyolo Ntozakhe Raymond Taziwa, Edson Meyer. Structural, Morphological and Raman scattering studies of Carbon doped ZnO nanoparticles fabricated by PSP technique. Journal of Nanoscience & Nanotechnology Research[J]. 2017;1(1:3).
- [26] Anderson Janotti, Chris G. Van de Walle. Oxygen vacancies in ZnO. Applied Physics Letters[J]. 2005;87(12):122102.
- [27] S. D. Shinde, S. K. Date, A. V. Deshmukh, et al. Role of Al doping in structural, microstructural, electrical and optical characteristics of as-deposited and annealed ZnO thin films. RSC Adv[J]. 2015;5(31): 24178-87.
- [28] A. Momot, M. Amini, G. Reekmans, et al. A novel explanation for the increased conductivity in annealed Al-doped ZnO: an insight into migration of aluminum and displacement of zinc. Physical chemistry chemical physics : PCCP[J]. 2017;19(40):27866-77.
- [29] Santanu Das, Sukhen Das, Soumyaditya Sutradhar. Effect of Gd³⁺ and Al³⁺ on optical and dielectric properties of ZnO nanoparticle prepared by two-step hydrothermal method. Ceramics International[J]. 2017;43(9): 6932-41.
- [30] Chundong Li, Jinpeng Lv, Zhiqiang Liang, et al. Study on the optical absorption and green emission of ZnO phosphors by varying Al doping contents. Optical Materials[J]. 2013;35(3):586-9.
- [31] Harish Kumar Yadav, K. Sreenivas, R. S. Katiyar, et al. Defect induced activation of Raman silent modes in rf co-sputtered Mn doped ZnO thin films. Journal of Physics D: Applied Physics[J]. 2007;40(19):6005-9.
- [32] N. Rajeswari Yogamalar, A. Chandra Bose. Absorption-emission study of hydrothermally grown Al:ZnO nanostructures. Journal of Alloys and Compounds[J]. 2011;509(34):8493-500.

- [33] A. Slassi, S. Naji, A. Benyoussef, et al. On the transparent conducting oxide Al doped ZnO: First Principles and Boltzmann equations study. *Journal of Alloys and Compounds*[J]. 2014;605:118-23.
- [34] Linhua Xu, Gaige Zheng, Hongyan Wu, et al. Strong ultraviolet and violet emissions from ZnO/TiO₂ multilayer thin films. *Optical Materials*[J]. 2013;35(8):1582-6.
- [35] X. Y. Ma, Z. Wang, J. W. Song, et al. Optical properties of ZnO and Mn-doped ZnO nanocrystals fabrication by vapor phase transport processes. *Nano-Micro Letters*[J]. 2010;1(1).
- [36] Haibo Zeng, Guotao Duan, Yue Li, et al. Blue Luminescence of ZnO Nanoparticles Based on Non-Equilibrium Processes: Defect Origins and Emission Controls. *Advanced Functional Materials*[J]. 2010;20(4):561-72.
- [37] Yinyan Gong, Tamar Andelman, Gertrude F. Neumark, et al. Origin of defect-related green emission from ZnO nanoparticles: effect of surface modification. *Nanoscale Research Letters*[J]. 2007;2(6):297-302.
- [38] A. Janotti, C. G. Van de Walle. Native point defects in ZnO. *Physical Review B*[J]. 2007;76(16).
- [39] S. L. Bai, T. Guo, Y. B. Zhao, et al. Mechanism enhancing gas sensing and first-principle calculations of Al-doped ZnO nanostructures. *J Mater Chem A*[J]. 2013;1(37):11335-42.

Chapter 5

Effects of selective doping or co-doping on (Al, Ti, Mg) oxide on ZnO based ceramics

5.1 Introduction

The fundamental and application researches on ZnO-based conductive ceramics attract the interest of a wide scientific community due to the versatile properties required for current or emerging technologies. High-performance ZnO conductive ceramics can be obtained by selecting appropriate dopants and adopting appropriate preparation processes. For ZnO conductive ceramics, a high conductivity is the most important parameter. In addition, the structural density, temperature stability, non-linear coefficient and power density of the ceramics are also important properties that affect the potential application of ZnO conductive ceramics. In Chapters 3 and 4, we have synthesized Al, Ti, and Mg co-doped ZnO ceramics, and obtained a high conductivity up to $1.52 \times 10^5 \text{ S} \cdot \text{m}^{-1}$ at room temperature. We have proved that Al_2O_3 is an efficient dopant for improving the conductivity of ZnO-based ceramics. The ionic radius of Al^{3+} is much smaller than that of Zn^{2+} , thus Al ions can form stable substitutional or interstitial doping in the ZnO host structure. Al^{3+} ions substitute Zn^{2+} ions to form donor centers, which can increase the concentration of charge carriers and the conductivity. Therefore, Al_2O_3 can be selected to achieve high conductivity of ZnO ceramics^[1, 2]. However, in addition to Al_2O_3 , other doping oxides such as TiO_2 and MgO were used. Their choice is motivated by their role on the structure, morphology and thermal behavior of the underlying ZnO-based ceramics. Besides, their association with Al_2O_3 is also relevant concern with regard to the electrical properties induced by Al ions in the host networks.

For TiO_2 doping, it can be expected that a similar role of Al^{3+} can be ensured by Ti^{4+} ions which can also act as donors to improve the conductivity of Ti doped ZnO materials^[3]. However, due to the low solubility of Ti^{4+} ions in ZnO, a spinel structure

as Zn_2TiO_4 can easily be formed^[4]. This secondary phase can increase the densification of the ceramics, control the grain size as well as the chemical composition features at the grain boundaries^[5, 6]. TiTi^{4+} ions are required to adjust the temperature coefficient of resistance of ZnO-based ceramics^[7]. Concerning MgO doping, the electrical features are no longer improved due to Mg^{2+} ions with similar size and valence as Zn^{2+} ions. However, an increase in the band gap and a decrease in AC conductivity in the $\text{Mg}_x\text{Zn}_{1-x}\text{O}$ thin films were previously reported in the literatures. This indicates that MgO affects the long-range order and defect morphology of the structure^[8, 9]. In addition, even limited, MgO contributes to a small increase in the electrical conductivity of ZnO conductive ceramics and increases the temperature coefficient of resistance from negative values to positive values^[10, 11]. Taking into account the different valence states and solubility of the three ions (Al, Ti, and Mg) in the host ZnO lattice, systematic studies with selective doping or co-doping by one, two or three elements were carried out in this work to analyze the roles of doping elements and their combination on the structure and electrical behavior. In particular, the present contribution is devoted to co-doping effects of the three selected ions on the local and long range order of co-doped ZnO ceramics with an emphasis on the related electrical behavior.

In this chapter, X-ray diffraction, scanning electron microscopy (SEM), and Raman spectroscopy are used to study the structure and morphology. Meanwhile, solid-state nuclear magnetic resonance (NMR) spectroscopy and electron paramagnetic resonance (EPR) spectroscopy are used to shed light on the local environment and defects type. The experimental investigations and their analyses point out the different location of the doping ions in the host ZnO lattice as substitutional, interstitial sites or vacancies and their incidence on the physical response. The mechanism leading to a drastic increase of the electrical conductivity by Al doping is discussed based on particular defect structures acting as shallow donors in the host ZnO based ceramics.

5.2 Sample preparation and characterization

The traditional solid-phase reaction method was used to prepare ZnO-based ceramic samples by single-doping or co-doping with Al_2O_3 , TiO_2 , and MgO according to the experimental scheme in Table 5.1. The objective is to explore the effects of Al, Ti and

Mg elements on the structure and electrical properties of ZnO-based conductive ceramics. Preparation parameters consist in the sintering temperature fixed at 1200 °C with a time duration of 2 hours under air as the sintering atmosphere. The nomenclature of samples is chosen according to whether the corresponding Al, Ti, and Mg elements are used as doping elements (Table 5.1). Thus, the considered samples are hereafter referred as ZnO, ZnO: Al, ZnO: Ti, ZnO: Mg, ZnO: AlMg, ZnO: TiMg, ZnO: AlTi, and ZnO: AlTiMg.

Table 5.1 Initial composition of the investigated doped ZnO based ceramics

Samples	ZnO (mol %)	Al₂O₃ (mol %)	TiO₂ (mol %)	MgO (mol %)
ZnO	100.00	-	-	-
ZnO:Al	99.75	0.25	-	-
ZnO:Ti	99.50	-	0.50	-
ZnO:Mg	99.00	-	-	1.00
ZnO:AlMg	98.75	0.25	-	1.00
ZnO:TiMg	98.50	-	0.50	1.00
ZnO:AlTi	99.25	0.25	0.50	-
ZnO:AlTiMg	98.25	0.25	0.50	1.00

XRD, SEM, Raman spectroscopy, EPR, and NMR experimental equipment were used to characterize the phase structure, surface morphology, defect structure, and local microstructure of doped ceramic samples. The electrical properties such as conductivity, carrier concentration and mobility were obtained by using the Pro4 four-point probe test system and the PPMS-9 comprehensive physical property measurement system. The detailed experimental parameters and the operation process are detailed in the Chapter 2.

5.3 Structural studies

The XRD patterns of the different doped ceramics are shown in Fig. 5.1. The main XRD lines are ascribed to the wurtzite structure of ZnO in agreement with the

reference JCPDS No. 36-1451. There are also secondary phases as seen by their additional XRD lines emanating from spinel phases or solid solutions which are formed in co-doped ceramics. In order to obtain accurate crystallographic information of the corresponding phases, the features of the involved crystalline structures such as the full width at half-maximum (FWHM) and lattice parameters of phases were determined by using a Rietveld refinement of the highest diffraction intensity peaks of the ZnO main phase and the spinel second phase in XRD patterns. Fig. 5.2a-c report the results related to FWHMs of the (110) diffraction peak at $2\theta=36.2^\circ$ of the wurtzite ZnO structure and the corresponding lattice parameters. Fig. 5.2d shows the evolution of the FWHMs of the main diffraction line (113) at $2\theta=35.5^\circ$ and the lattice parameter of the identified secondary spinel phases.

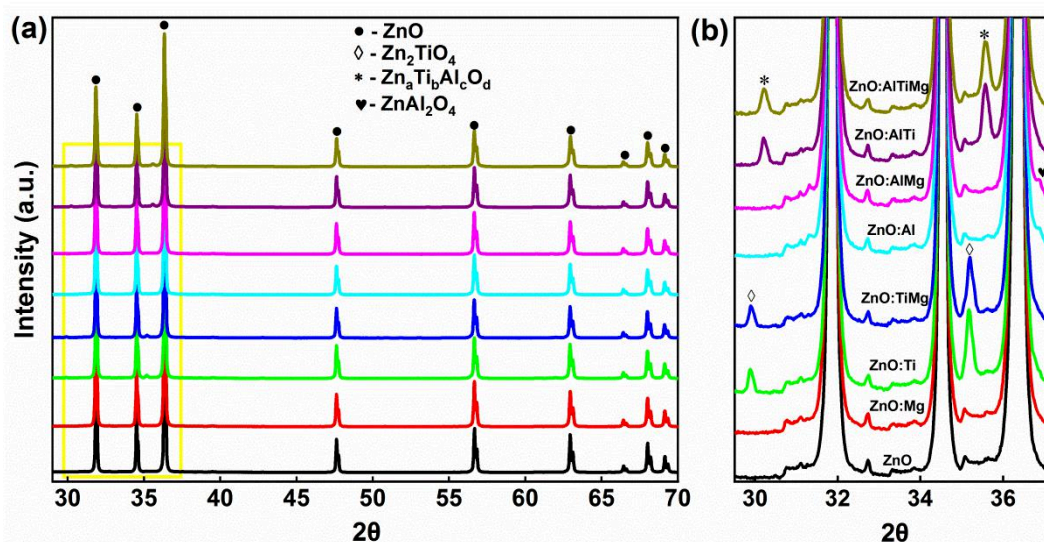


Figure 5.1 (a) XRD patterns of as-synthesized samples, (b) The enlarged figure highlights the behavior of the spinel phase diffraction lines

As shown in Fig. 5.1, in TiO₂ doped samples (ZnO: Ti and ZnO: TiMg), the spinel phase is characterized by the diffraction line at $2\theta = 35.5^\circ$ is Zn₂TiO₄ (JCPDS No. 25-1164). Due to the different coordination number and ionic radii of Ti and Zn, only a small amount of Ti can be dissolved in ZnO grains. In this experiment, the doping ratio of Ti exceeds its solubility limit in ZnO^[28], thus Zn₂TiO₄ is formed in the samples ZnO: Ti and ZnO: TiMg. In addition, Fig. 5.2b and Fig. 5.2c show a lattice

expansion for samples ZnO:Ti and ZnO:TiMg which may result from an incorporation of Ti ions in the host ZnO lattice. In Al doped samples (ZnO:Al, ZnO:AlMg), an additional weak diffraction line was resolved at $2\theta = 36.3^\circ$ (Fig. 1b) and assigned to the ZnAl_2O_4 spinel phase. This phase is induced by doping ratio of Al (0.25 mol%) which exceeds the solubility limit, which is less than (< 0.25 mol%) in ZnO ceramics sintered under $\text{N}_2 + \text{CO}$ ^[12, 13]. The change of the lattice parameters as inferred from Fig. 5.2b and 5.2c, indicates that Zn ions are substituted by Al in the host ZnO lattice.

For co-doped Ti and Al samples (ZnO:AlTi, ZnO:AlTiMg), a net shift is seen for the diffraction peaks of the spinel phase at $2\theta=35.5^\circ$ (Fig.1b). We tentatively attributed this evolution to a mixed spinel phase as $\text{Zn}_a\text{Ti}_b\text{Al}_c\text{O}_d$, which possesses the same crystal structure and lattice parameters as $\text{Zn}_2\text{Ti}_3\text{O}_8$ according to the identification based on database of X'Pert High Score. The Al substitution in Ti sites of the spinel phase may account for the shorter lattice parameters and induce a disorder in this secondary phase as illustrated from the increase of FWHMs (Fig. 5.2d). The increase of the lattice parameters of ZnO induced by Ti doping seems to be counterbalanced by Al co-doping as shown in Fig. 5.2b and 5.2c. Indeed, as the ionic radius Al^{3+} is smaller than that of Ti^{4+} and Zn^{2+} , Al rather tends to substitute Zn or Ti rather than forming an Al spinel phase such as ZnAl_2O_4 which was not observed in the ZnO:AlTi and ZnO:AlTiMg samples. The different ionic radii (0.74 Å for Zn^{2+} , 0.54 Å for Al^{3+} and 0.67 Å for Ti^{3+} , 0.61 Å for Ti^{4+}) induce strains in the host lattice. In addition, the difference in the valence states of the doping ions, their local environment and the induced oxygen vacancies increase the disorder. This is illustrated in Fig. 5.2a: the FWHMs of samples ZnO:Ti, ZnO:TiMg, ZnO:Al, ZnO:AlMg, ZnO:AlTi and particularly of particularly the triple doped ZnO:AlTiMg are significantly higher than those of samples ZnO and ZnO:Mg.

Finally, it is worth noting that no diffraction peak related to MgO was detected on XRD patterns, and Mg doping has no significant influence on the lattice parameter of

ZnO. This is explained by the compatibility of the ionic radius and the valence state between Mg and Zn along with the high solubility limit (2 mol %) of Mg^{2+} in ZnO ceramics^[14].

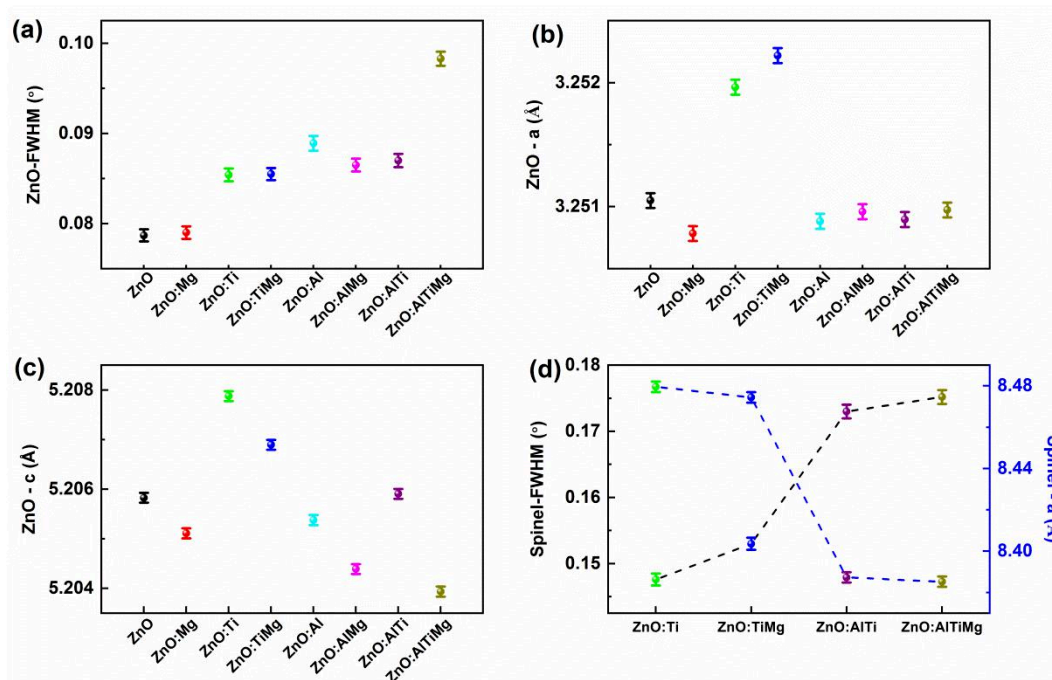


Figure 5.2 (a) The FWHMs of ZnO (101) peak. (b), (c) The lattice parameters a and c of ZnO, (d) The FWHMs of spinel phase (113) peak and its lattice parameter a obtained by Rietveld refinement

5.4 Morphology studies

In order to define the location of the secondary crystalline phases as coexisting structures inside ZnO grains or segregated at the grain boundaries, SEM investigations were carried out on the co-doped ZnO ceramics and the resulting SEM images are shown in Fig. 5.3.

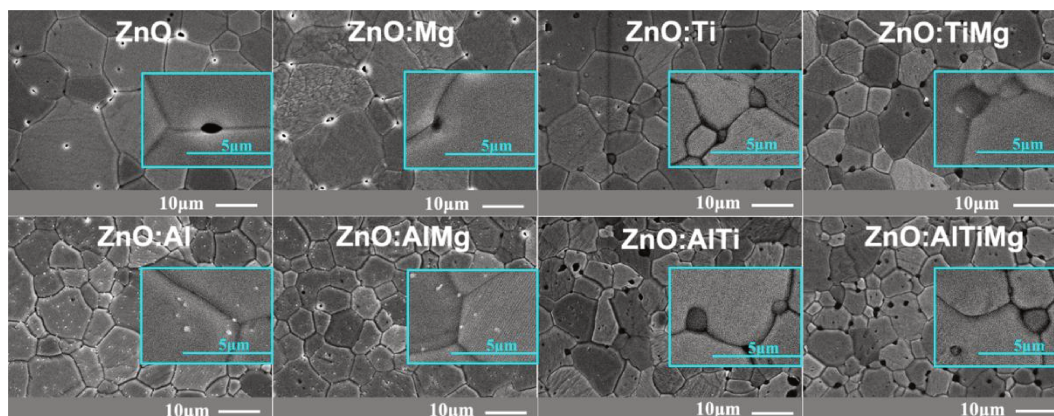


Figure 5.3 SEM images of co-doped ZnO based ceramics

In the SEM images in Fig. 5.3, the observed pores with bright edges on samples ZnO and Mg indicate that pure and Mg doped ZnO ceramics possess less compact network. For the four samples containing Ti (ZnO:Ti, ZnO:TiMg, ZnO:AlTi and ZnO:AlTiMg), there are some small dark spots around the ZnO particles. They may correspond to the secondary spinel phase observed by XRD, with a particular contribution of Ti based structures because of the low solubility limit of Ti in ZnO ceramics. Moreover, the secondary phase as $ZnAl_2O_4$ is noticed as the small white spots only in samples ZnO:Al and ZnO:AlMg. Fig. 5.4 shows the average grain size as calculated by Image J software from the SEM images. Samples ZnO and ZnO:Mg present a similar microstructure due to the compatibility of Mg and Zn ions. For ZnO:Al, ZnO:AlMg, ZnO:Ti, ZnO:TiMg, ZnO:AlTi, ZnO:AlTiMg samples, the average grain size is smaller compared to ZnO and ZnO:Mg samples. Therefore, it can be concluded that secondary phases generated by Al or Ti inhibits the grain growth. Based on the SEM images and XRD analysis, spinel phases as Zn_2TiO_4 , $ZnAl_2O_4$ or $Zn_aTi_bAl_cO_d$ were stabilized in Ti, Al and (Ti, Al) doped ZnO ceramics respectively. The inhibitive trend is due to the pinning effect of these spinel phases when they are located at the grain boundaries or at the triple junctions of doped ZnO ceramics as shown in Fig. 5.4.

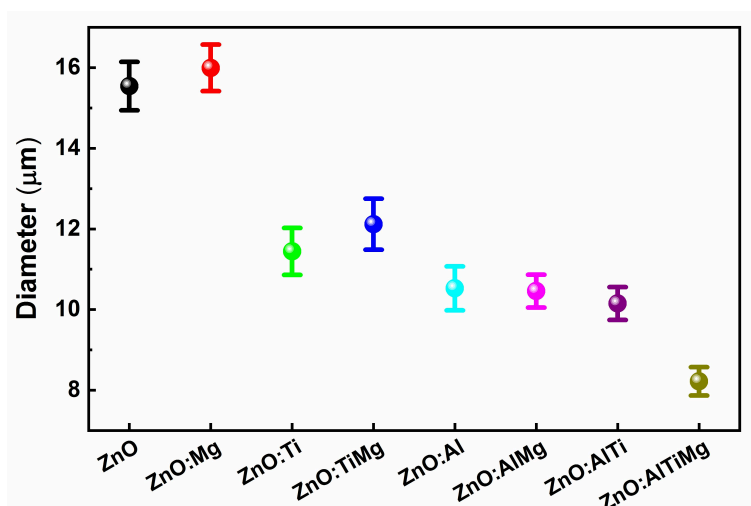


Figure 5.4 Average grain sizes of co-doped ZnO based ceramics

5.5 Conduction features in ZnO ceramics

Beyond the influence of the co-doping process on the microstructure and crystalline features, the electrical conductivity varies in a large extent from 10^{-4} to 10^4 $\text{S}\cdot\text{m}^{-1}$ as function of the nature of the doping elements (Fig. 5.5). Hall experiment was also applied to show the influence of doping on overall carrier concentration (n) and carrier mobility (μ), the results are shown in Fig. 5.6. Co-doped ZnO based ceramics with Al doping or co-doping (ZnO:Al, ZnO:AlMg, ZnO:AlTi, ZnO:AlTiMg) show the highest conductivities. As an example, a conductivity 2.6×10^4 $\text{S}\cdot\text{m}^{-1}$ was obtained in the sample ZnO:AlMg; i.e. in the order of 10^5 times that of pure or of other doping elements such as Ti or Mg without Al. Besides, samples ZnO:Al, ZnO:AlMg, ZnO:AlTi and ZnO:AlTiMg have quite higher carrier concentration and carrier mobility. Thus, the mechanism of the high electrical conductivity by Al^{3+} ion doping lies in the reinforcement of the n-type nature of ZnO from the involved shallow donors^[15] and the increased mobility of them. Oppositely, Mg or Ti doping alone don't modify significantly the carrier concentration, carrier mobility and electrical conductivity compared to pure ZnO. On one hand, the compatibility of charge and radius size between Mg and Zn ions did not affect the charge carriers. On the other hand, the insulating secondary phases induced by Ti doping limit the conductivity

which remains in the same order of magnitude as in pure ZnO.

The understanding of the doping effect on the electrical behavior requires a deep insight in the modification of the local environment hosting the doping ions. In this aim, experimental studies by Raman and local order techniques such as EPR and NMR were applied to evaluate the local distortions and the features of the electronic active centres induced by doping.

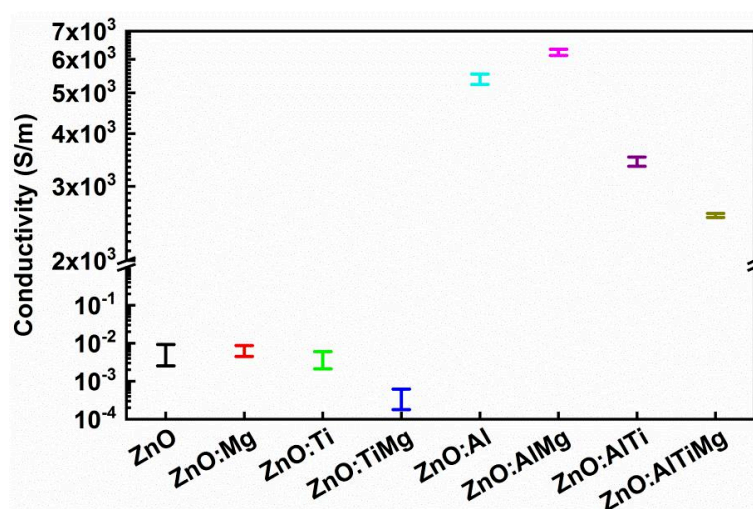


Figure 5.5 Electrical conductivity of ZnO ceramic samples

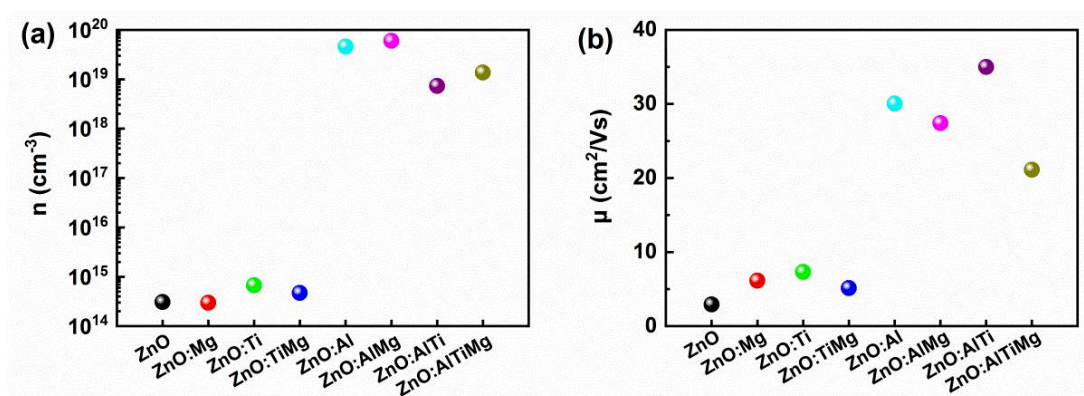


Figure 5.6 (a) The carrier concentration (n) and (b) carrier mobility (μ) of samples

5.6 Vibrational signatures of doped ZnO based ceramics

Raman spectroscopy is a sensitive tool to investigate the crystallinity, the structural

disorder, and the local distortions induced by different types of defects which account for the high conductivity in ZnO doped ceramics. The formation of some defects is an important factor for the high conductivity of ZnO-doped ceramics, so it is necessary to perform Raman spectroscopy testing on eight ZnO-based ceramics with different doping compositions. The wurtzite ZnO belongs to the C_{6v}^{4} ($P6_3mc$) space group with two formula units per primitive cell. The group theory predicts 12 phonon branches (9 optical and 3 acoustic modes) at the center of the Brillouin zone. Acoustic modes are generally not observed by Raman in bulk samples because of the inverse dependence of the frequency to the particle size^[16]. According to group theory prediction, the optical modes of ZnO at the center of the Brillouin zone (BZ) can be represented by the irreducible representation: $\Gamma_{opt}=A_1+2B_1+E_1+2E_2$. In contrast to B_1 modes being Raman silent modes, A_1 and E_1 modes are both Raman and infrared active, and the E_2 mode is only Raman active. Strong electrostatic forces split the polar A_1 and E_1 branches into longitudinal optical (LO) and transverse optical (TO) modes such as $A_1(LO)$, $A_1(TO)$ and $E_1(LO)$, $E_1(TO)$ ^[17]. The nonpolar E_2 consists of two modes, namely, E_2^{high} at high frequency and mainly associated with oxygen displacement characterizing the wurtzite lattice, and the low frequency E_2^{low} mainly associated to the Zn sub-lattice^[18].

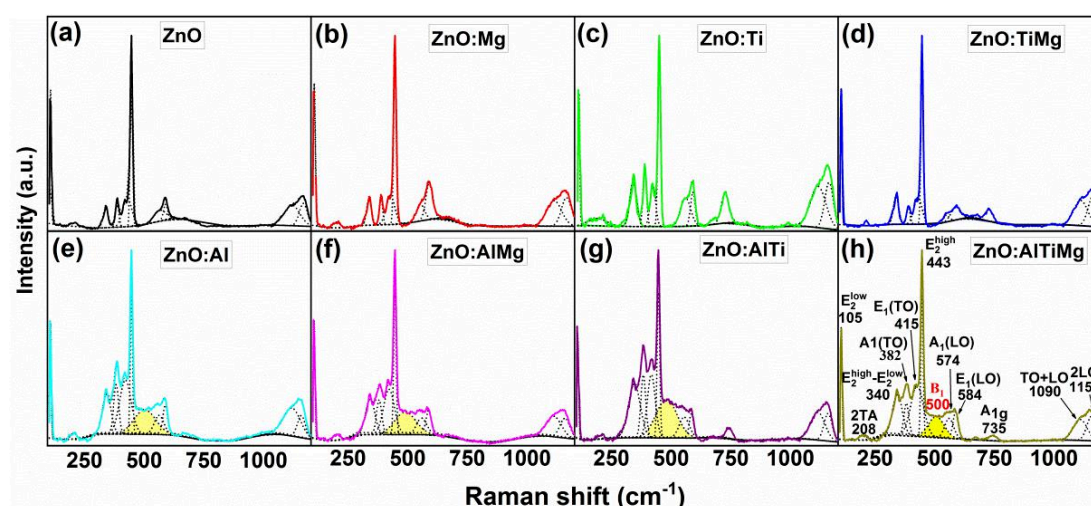


Figure 5.7 Raman spectra of ZnO based ceramics

For the assignment of the Raman spectra, the modes were first normalized according

to the E_2^{high} peak at Fig. 5.7. Raman spectra of doped-ZnO ceramics exhibit a combination of both first- and second-order modes. Those associated to Raman modes^[19, 20] were observed at $E_2^{\text{high}}=443\text{ cm}^{-1}$, $E_2^{\text{low}}=105\text{ cm}^{-1}$, $A_1(\text{TO})=382\text{ cm}^{-1}$, $A_1(\text{LO})=574\text{ cm}^{-1}$, $E_1(\text{TO})=415\text{ cm}^{-1}$, $E_1(\text{LO})=584\text{ cm}^{-1}$ and $2\text{TA}=208\text{ cm}^{-1}$, $E_2^{\text{high}}-E_2^{\text{low}}=340\text{ cm}^{-1}$, $\text{TO}+\text{LO}=1090\text{ cm}^{-1}$, $2\text{LO}=1150\text{ cm}^{-1}$. A weak Raman peak located at 735 cm^{-1} for samples doped by Ti was assigned to the A_{1g} mode involved in the titanium zinc spinel phase in TiO_2 doped samples ($\text{ZnO}:\text{Ti}$, $\text{ZnO}:\text{TiMg}$, $\text{ZnO}:\text{AlTi}$, $\text{ZnO}:\text{AlTiMg}$). The Raman bands detected at 574 cm^{-1} and 584 cm^{-1} in all eight samples correspond to $A_1(\text{LO})$ and $E_1(\text{LO})$ modes associated to structural disorder or lattice defects such as oxygen vacancies, Zn interstitials and their combination as suggested from the strong dependence of these bands on the oxygen stoichiometry^[19, 21]. Besides, in contrast to other doping ions, Al doped samples ($\text{ZnO}:\text{Al}$, $\text{ZnO}:\text{AlMg}$, $\text{ZnO}:\text{AlTi}$, $\text{ZnO}:\text{AlTiMg}$) show singular broad Raman features (B_1 mode, Raman silent for perfect ZnO crystal) around 500 cm^{-1} . These features can be associated to Raman modes being activated by disorder effects in doped ZnO materials^[22] with an enhanced effect in Al doped ZnO ceramics. The above structural disorder in Al doped ceramics is accompanied by the high electrical conductivity compared to pure ZnO sample. Particular electronic configurations are involved and can be probed by using EPR and NMR.

EPR and NMR are local probe techniques able to give precise assignment on the coordination of defined chemical elements such as paramagnetic doping ions or electronic active centres by EPR and local order of Al and Zn ions by NMR. A net correlation was pointed out between the conductivity and the experimental signatures by EPR and NMR techniques of particular local structures hosting the doping Al and giving rise to electronic active defects. This helps to shed light on the mechanism leading to enhanced electrical conductivities in Al doped ZnO based ceramics, and explain why Ti and Mg have little effect on the conductive properties of ZnO-based ceramics.

5.7 Electronic active defects probed by EPR

EPR spectra and their related parameters (line width ΔH , integrated intensity I_{EPR} , g-factor) are depicted in Fig. 5.8. All spectra consist in a Lorentzian derivative line shape with different line widths and a resonance position characterized by g-factor in the ranges 1.957-1.961 which can be related to the same species of paramagnetic centres. The EPR spectra are characterized by different integrated intensities and quite different line widths depending on the doping nature as hereafter outlined.

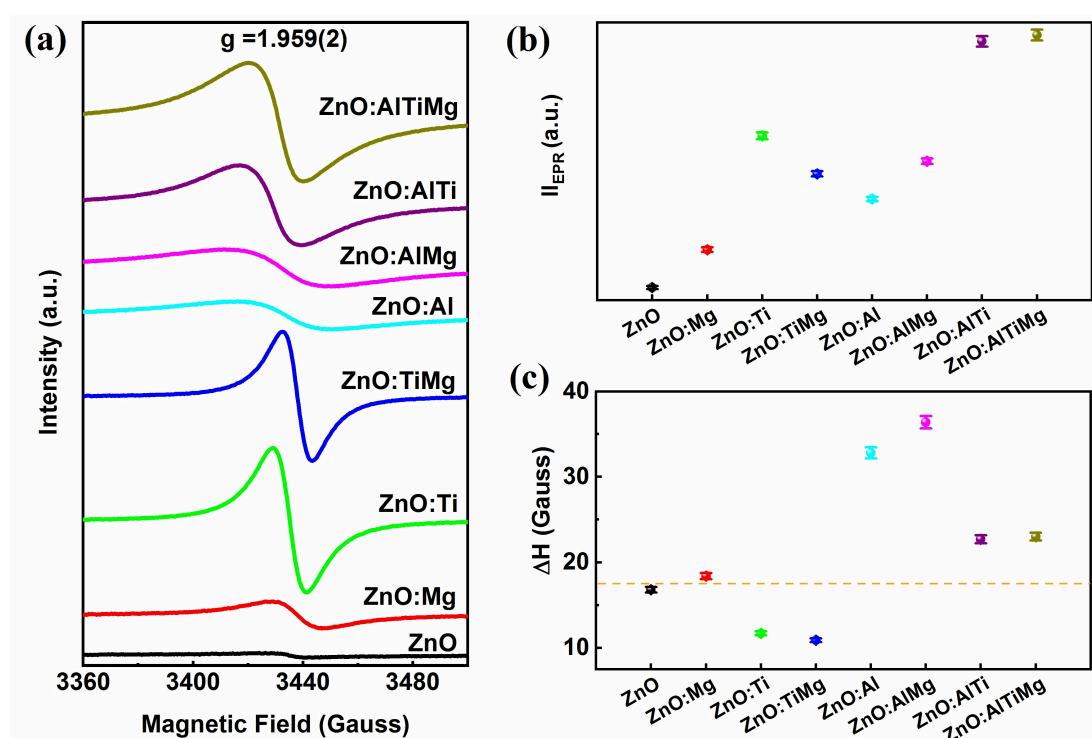


Figure 5.8 (a) EPR spectra of samples at room temperature, (b) and (c) EPR integrated intensity and linewidth, respectively, for different co-doped ZnO based ceramics

Mg doped ZnO sample (ZnO:Mg) shows a significant EPR signal but with the lowest intensity compared to other doping elements. As discussed in the structural studies section, Mg fits to the crystalline sites of Zn due to the similar ionic radii and the same valence state. We may therefore expect the same kind of defects as in pure ZnO. Thus, oxygen vacancies (V_O)^[23, 24], zinc vacancies (V_{Zn})^[25] or interstitial zinc (Zn_i)^[26] can be considered. The corresponding defect energy levels^[27-29] involved within the

ZnO band gap are qualitatively depicted in Fig. 5.9. However, as discussed by Look *et al.*^[30], V_{Zn} possesses the features of an acceptor in contrast to the shallow donor Zn_i . The V_O centres, are thermodynamically unstable even if they act as deep donors. They also require high temperatures or UV radiation to be activated^[31, 32]. Thus, we may assign the native paramagnetic centers in sample ZnO:Mg to Zn_i species with Landé g -factor=1.960. The increase of EPR signal intensity compared to pure ZnO can be explained by the incorporation of Mg in ZnO lattice. The doped structure is expected to favor the migration of Zn ions to interstitial positions during the process of sintering at high temperatures. The sample ZnO and ZnO:Mg have the same paramagnetic substance (Zn_i), but the ZnO:Mg sample has a higher concentration, so the linewidth of the corresponding characteristic EPR line is basically same and the integrated intensity is increased.

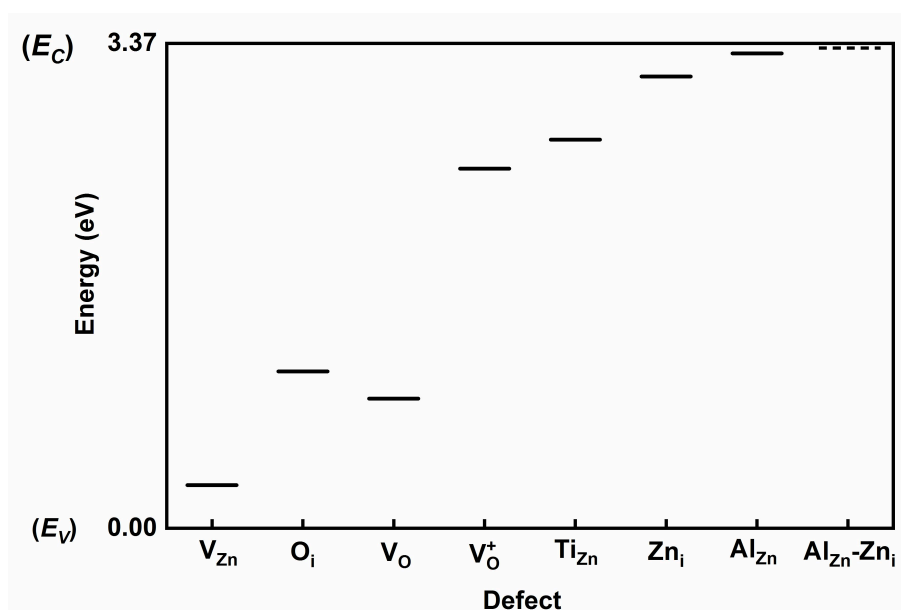


Figure 5.9 Qualitative plot of energy levels for defects involved in (Al, Ti) doped ZnO samples

Al doped ZnO samples (ZnO:Al, ZnO:AlMg) give rise to EPR signals located at g -factor=1.961 with a higher intensity and a broad line-shape compared to Mg doped sample. The increase in the EPR line intensity can be related to the substitutional Al ions (Al_{Zn}) which favor the formation of interstitial Zn (Zn_i) as also shown for Mg

doping. Thus, the shallow donors (Al_{Zn} , Zn_i) centres account for the same origin of the paramagnetic species in Al doped ZnO. The co-doping by addition of Mg (sample ZnO:AlMg) doesn't change the line-shape of the EPR signal but increases the integrated line intensity (Fig. 5.8), which is corroborated by an increase of the interstitial sites Zn_i by substitutional Mg doping. Moreover, the high conductivity induced in Al doped samples is caused by delocalized electrons emanating from the shallow donors Al_{Zn} (Fig. 5.9). The net effect on the EPR signals consists in the huge broadening shown in Fig. 5.8. The mechanism is based on the Korringa relaxation mechanism as discussed in the chapter 3^[1, 21]. Ti doped ZnO samples (ZnO:Ti, ZnO:TiMg) show the EPR signal with the highest integrated intensity and the lowest line width compared to other mono-doped samples. As the EPR line position leads to g -factor = 1.958, we expect the origin of the EPR signal as related to Ti^{3+} . Mg co-doping in the ZnO:TiMg sample leads to the same g -factor and the same line width as reported in Ti doped sample. The effect of Zn_i caused by Mg doping is much weaker than that of Ti^{3+} caused by Ti doping, thus the EPR spectra peaks formed by ZnO: TiMg samples and ZnO: Ti samples are similar. The expected origin of the paramagnetic centers in samples ZnO:Ti and ZnO:TiMg are the reduced Ti^{3+} ions. Their involvement in the above samples can be favored by the oxygen vacancies as discussed in reference⁴⁹.

Finally, ZnO:AlTi and ZnO:AlTiMg samples give rise to EPR signals consistent with superimposed contributions already discussed in Al and Ti doped samples. In particular, Al doping favors an enhanced electrical conductivity by promoting electrons in the conduction band of the ZnO structure. Fig. 5.10 correlates the evolution of the EPR line width with the electrical conductivity. The increase of the line width with the conductivity is coherently attributed to the conduction electrons inducing relaxation of the paramagnetic centres by Korringa relaxation^[33]. This result underlines the involvement of conduction electrons by Al doping while Ti doping creates reduced Ti^{3+} ions with the features of deep donors limiting the charge delocalization.

To sum up, Al doping improves the concentration of charge carriers by promoting electrons in the conduction band of ZnO. Ti doping favors the occurrence of paramagnetic species as reduced Ti^{3+} ions. For the electrical conductivity, Ti^{3+} ions do not induce higher conductivity in ZnO based ceramics due to their deep donor nature. Moreover, spinel phases (Zn_2TiO_4 or $Zn_aTi_bAl_cO_d$) are easily formed by Ti doping and further inhibit any improvement of electrical conductivity in the host ZnO ceramics (Fig. 5.10).

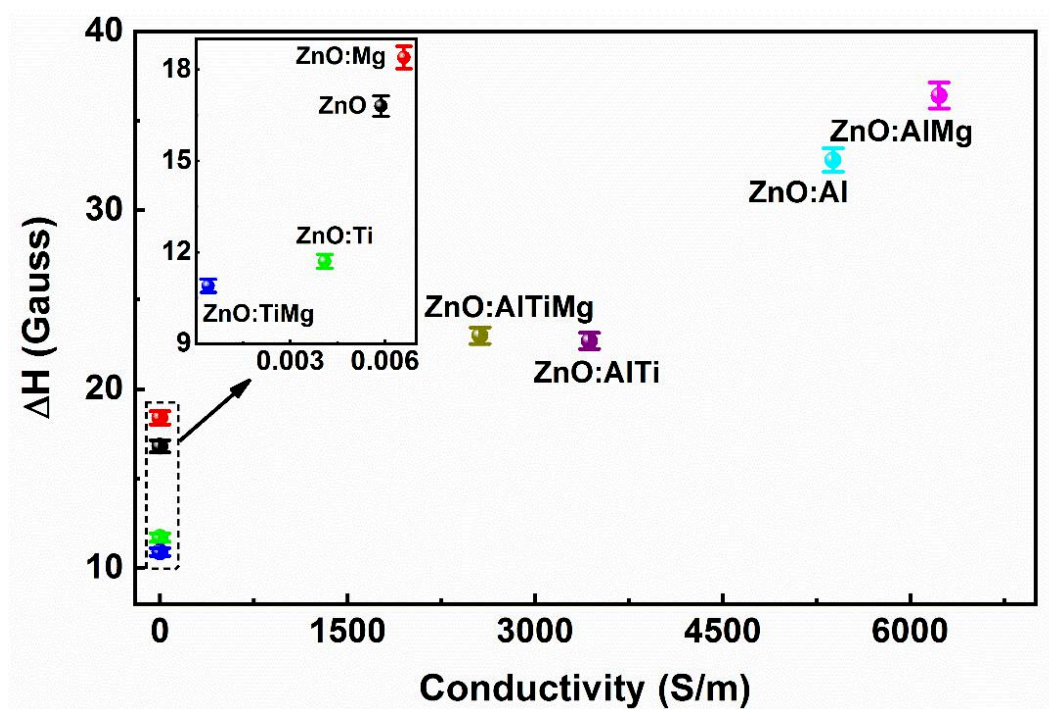


Figure 5.10 EPR spectra line width versus the electrical conductivity in samples

5.8 Local order probing of Al and Zn ions

Solid state NMR experiments were carried out in order to characterize the local environment of Zn ions in eight samples and the local environment of Al ions in four Al-doped samples. The central transition region of MAS spectra of the ^{27}Al dopant is shown in Fig. 5.11a. As already outlined in our previous work, there are two well defined, distinct signals that are not dispersed, showing that the synthesis method leads to a doping with two well defined Al environments. Moreover, there is a Al(VI) signal of Al in octahedral (AlO_6) coordination, but the (diamagnetic) Al(IV) signal of

Al in tetrahedral (AlO_4) coordination, usually at 70-80 ppm^[34] is absent. Instead, there is a signal at the unusual frequency of about 185 ppm. The deviation from the normal range has been attributed to a Knight shift caused by the conduction electrons, which stems from aluminum in $\text{Al}_{\text{Zn}}\text{-Zn}_i$ complexes where Al substitutes Zn, and Zn migrates to an interstitial position. The intensity of this signal has been found in our previous study to be correlated to the conductivity as both changed in the same way as a function of the sintering atmosphere. The conductive electrons in the high conductive sample act on the tetra-coordinated Al to cause a Knight shift effect, which causes the Al (IV) peak to be invisible, and a Knight shift peak at 185 ppm appears. The conduction electrons do not extend to the octacoordinated Al, so no shift of the Al (VI) peak at 0 ppm is observed.

The central transitions of static ^{67}Zn spectra are shown in Fig. 5.11b. The spectrum of pure ZnO exhibits the typical quadrupolar pattern with a quadrupolar coupling of $n_Q = 361$ kHz, a low asymmetry ($h_Q = 0.06$) and a chemical shift of 238 ppm, consistent with previous works^[35]. While Mg doping does not have a visible influence on the Zn spectra, Ti doping leads to a slight broadening of the singularities. This confirms the above finding that Ti, in contrast to Mg, induces some disorder in the crystal. Al doping has, as seen for the samples ZnO:Al, ZnO:AlTi, and ZnO:AlTiMg, a larger impact on the signal. It is not only more broadened, almost making the quadrupolar features invisible, but also induces a significant shift (1.5 kHz/ 80 ppm). A straightforward explanation is the connection with conduction electrons, similarly as observed for the Al signal at 185 ppm. We thus see a sign of the delocalization of these electrons over at least a major part of the crystal, therefore the signal in the NMR spectra of the samples ZnO: Al, ZnO: AlTi and ZnO: AlTiMg are broadened.

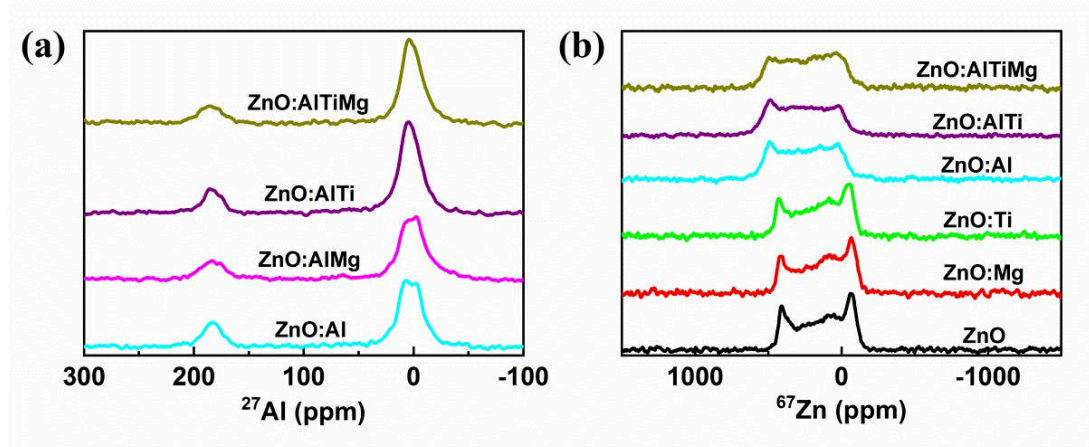


Figure 5.11 (a) ^{27}Al MAS NMR spectra of samples doped by Al_2O_3 (b) ^{67}Zn static NMR spectra of samples ZnO, ZnO:Mg, ZnO:Ti, ZnO:Al, ZnO:AlTi, and ZnO:AlTiMg.

5.9 Conclusion

Based on the single-doped or multi-doped systems of Al_2O_3 , TiO_2 , and MgO in ZnO conductive ceramics, the effects of local disorder and electronic activity defects on the properties of ZnO-based ceramics are studied in this chapter. ZnO-based ceramics with different components are synthesized by changing the doping ratio of Al, Ti, and Mg ions. Different doping combinations will greatly change the electrical conductivity, phase composition, microstructure and defect states in ZnO-based ceramics. This work contributes to understand the respective effects of doping elements in a single doping co-doping process. The origin of the high conductivity is also discussed based on the respective roles of doping elements and the secondary phases which coexist with the major phase based on wurtzite ZnO structures. The main achievement of this work is hereafter summarized.

1. All the considered doped or co-doped ZnO-based ceramic possess good crystalline quality with the major wurtzite-structured ZnO phase. Besides, Al, Ti, and (Al, Ti) co-doped samples have ZnAl_2O_4 , Zn_2TiO_4 , and $\text{Zn}_a\text{Ti}_b\text{Al}_c\text{O}_d$ spinel phases, respectively, which affect the microstructure and the density of grain boundaries which alter the electrical conductivity.

2. In contrast to other doping elements (Ti and Mg), Al-doped ceramics show the highest conductivity. The electrical behavior depends critically on the electronic defects caused by doping with particular local environments which characterized by complementary Raman, EPR and NMR methods.
3. In the ZnO-based ceramics doped with TiO₂, the involved Ti³⁺ ions are deep donor defects with limited charge delocalization and then no particular effect is expected on the electrical conductivity of the ZnO-based ceramics.
4. For ZnO-based ceramics doped with MgO, due to the compatibility of the valence and radii of Mg and Zn ions, the charge carriers is not affected and then no improvement occurs on the conductivity.
5. ZnO ceramics doped with Al₂O₃ exhibit higher electrical conductivity due to a high charge carrier induced by the incorporation of Al in the host ZnO lattice. Raman investigations indicates that the activation of the B₁ mode which is silent in perfect crystalline structure, results from an increase in the disorder of the ZnO structure, which is caused by defects such as Zn_i. In ²⁷Al NMR, the NMR peak of the Al-doped sample at 185 ppm is induced by the Knight shift effect resulting from delocalized electron density on Al_{Zn}-Zn_i complexes. These electronic active defects ensure the necessary charge carriers leading to the high conductivity in Al doped ZnO-based ceramics.

5.10 Reference

- [1] Q. Sun, G. Li, T. Tian, et al. Controllable microstructure tailoring for regulating conductivity in Al-doped ZnO ceramics. *J Eur Ceram Soc*[J]. 2020;40(2):349-54.
- [2] Qianying Sun, Tian Tian, Laoying Zheng, et al. Electronic active defects and local order in doped ZnO ceramics inferred from EPR and ²⁷Al NMR investigations. *J Eur Ceram Soc*[J]. 2019;39(10):3070-6.
- [3] Wang Y, Song J, Zheng W, et al. Experimental and theoretical analysis of H and Ti co-doped ZnO transparent conductive films. *Ceram Int*[J]. 2017; 43(7):5396-402.

- [4] Park K, Ko K. Effect of TiO₂ on high-temperature thermoelectric properties of ZnO. *J Alloy Compd*[J]. 2007;430:200-4.
- [5] T. Tian, L. Cheng, L. Zheng, et al. Defect engineering for a markedly increased electrical conductivity and power factor in doped ZnO ceramic. *Acta Mater*[J]. 2016;119:136-44.
- [6] T. Tian, L. H. Cheng, J. J. Xing, et al. Effects of sintering on the microstructure and electrical properties of ZnO-based thermoelectric materials. *Materials & Design*[J]. 2017;132:479-85.
- [7] Hai Feng, Zhijian Peng, Xiuli Fu, et al. Effect of TiO₂ doping on microstructural and electrical properties of ZnO-Pr₆O₁₁-based varistor ceramics. *Journal of Alloys and Compounds*[J]. 2010;497(1-2):304-7.
- [8] Shukla A, Kaushik V, Prasher D. Growth and characterization of Mg_xZn_{1-x}O thin films by aerosol-assisted chemical vapor deposition (AACVD). *Electron Mater Lett*[J]. 2014;10(1):61-5.
- [9] Othman Zr, Hafef O, Matoussi A, et al. AC conductivity and structural properties of Mg-doped ZnO ceramic. *Appl Phys A*[J]. 2015;121(2):625-34.
- [10] Tanaka S Shoji M, Shirakawa S. Effect of Al₂O₃, MgO and SiO₂ additives on electrical resistivity and sintering property of ZnO ceramics. *Journal of the Ceramic Society of Japan* [J]. 2000;108(1):89-93
- [11] J Zhu, J Wang, Y Zhou, et al. Major effects on microstructure and electrical properties of ZnO-based linear resistance ceramics with MgO changes. *J Mater Sci: Mater Electron*[J]. 2014;25: 2273-8.
- [12] K Shirouzu, T Ohkasa, M Hotta, et al. Distributuon and solubility limit of Al in Al₂O₃-doped ZnO sintered body. *J Ceram Soc Japn*[J]. 2007;115(4):254-8.
- [13] Wang N, Xin H, Li D, et al. High temperature thermoelectric properties of Nb-doped ZnO ceramics. *J Phys Chem Solids*[J]. 2013;74(12):1811-5.
- [14] Segnit E, Holland A. Mg solid solubility limits in ZnO ceramics. *J Am*

- Ceram Soc[J]. 1965;48(8):409-13.
- [15] Han J, Mantas P, Senos A. Effect of Al and Mn doping on the electrical conductivity of ZnO. *J Eur Ceram Soc*[J]. 2001;21:1883-6.
- [16] Yadav H, Sreenivas K, Gupta V, et al. Structural studies and Raman spectroscopy of forbidden zone boundary phonons in Ni-doped ZnO ceramics. *J Raman Spectrosc*[J]. 2009;40(4):381-6.
- [17] C. A. Arguello, D. L. Rousseau, S. P. S. Porto. First-Order Raman Effect in Wurtzite-Type Crystals. *Phys Rev*[J]. 1969;181(3):1351-63.
- [18] Zhang R, Yin P, Wang N, et al. Photoluminescence and Raman scattering of ZnO nanorods. *Solid State Sci*[J]. 2009;11(4):865-9.
- [19] Cuscó R, Alarcón-Lladó E, Ibáñez J, et al. Temperature dependence of Raman scattering in ZnO. *Phys Rev B*[J]. 2007;75(16).
- [20] Thandavan T, Gani S, San W, et al. Enhanced photoluminescence and Raman properties of Al-Doped ZnO nanostructures prepared using thermal chemical vapor deposition of methanol assisted with heated brass. *PloS one*[J]. 2015;10(3):1-18.
- [21] Q. Sun, T. Tian, L. Zheng, et al. Electronic active defects and local order in doped ZnO ceramics inferred from EPR and ^{27}Al NMR investigations. *J Eur Ceram Soc*[J]. 2019;39(10):3070-6.
- [22] Serrano J, Manjón F, Romero A, et al. Phonon dispersion relations of zinc oxide: Inelastic neutron scattering and ab initio calculations. *Phys Rev B* [J]. 2010;81(17):174304.
- [23] Djurišić A, Choy W, Roy V, et al. Photoluminescence and electron paramagnetic resonance of ZnO tetrapod structures. *Adv Funct Mater*[J]. 2004;14(9):856-64.
- [24] Drouilly C, Krafft JM, Averseng F, et al. ZnO Oxygen Vacancies Formation and Filling Followed by in Situ Photoluminescence and in Situ EPR. *J Phys Chem C*[J]. 2012;116(40):21297-307.

- [25] Anderson J, Chris G. Native Point Defects and Doping in ZnO. USA: John Wiley and Sons Ltd; 2011.
- [26] Lv J, Li C. Evidences of V_O , V_{Zn} , and O_i defects as the green luminescence origins in ZnO. *Appl Phys Lett*[J]. 2013;103(23):232114.
- [27] M. Diaconu, H. Schmidt, H. Hochmuth, et al. Deep defects generated in n-conducting ZnO:TM thin films. *Solid State Communications*[J]. 2006; 137(8):417-21.
- [28] M. D. McCluskey, S. J. Jokela. Defects in ZnO. *Journal of Applied Physics*[J]. 2009;106(7):071101.
- [29] S. Vempati, J. Mitra, P. Dawson. One-step synthesis of ZnO nanosheets: a blue-white fluorophore. *Nanoscale Res Lett*[J]. 2012;7(1):470.
- [30] Look D.C, Hemsley J. W, Sizelove J. R. Residual Native Shallow Donor in ZnO. *Physical review letters*[J]. 1999;82(12):2552-5.
- [31] Anderson Janotti, Chris G. Van de Walle. Native point defects in ZnO. *Physical Review B*[J]. 2007;76(16).
- [32] Meyer BK, Hofmann DM, Stehr J, et al. Spectral Identification of Impurities and Native Defects in ZnO. USA: John Wiley and Sons Ltd; 2011.
- [33] Kassiba A, Bednarski W, Pud A, et al. Hybrid Core–Shell Nanocomposites Based on Silicon Carbide Nanoparticles Functionalized by Conducting Polyaniline: Electron Paramagnetic Resonance Investigations. *J Phys Chem C*[J]. 2007;111(31):11544-51.
- [34] C. Schilling, M. Záhres, C. Mayer, et al. Aluminum-doped ZnO nanoparticles: gas-phase synthesis and dopant location. *J Nanopart Res*[J]. 2014;16(7).
- [35] Roberts N, Wang R, Sleight A, et al. ^{27}Al and ^{69}Ga impurity nuclear magnetic resonance in ZnO:Al and ZnO:Ga. *Phys Rev B*[J]. 1998;57(10): 5734-41.

Chapter 6

Investigation of the local order and $\text{Al}_{\text{Zn}}\text{-Zn}_i$ defect complexes on the high conductivity in (Al, Ti, Mg) oxide co-doped ZnO ceramics

6.1 Introduction

The electrical conductivity of ZnO-based ceramics is related to many factors including intrinsic defects such as oxygen vacancy (V_O), interstitial zinc (Zn_i), and extrinsic defects introduced by crystallinity, grain boundaries, and doping, etc.^[1-3]. A wide set of investigations have pointed out that the n-type donor defects such as Al_{Zn} formed by Al_2O_3 doping in ZnO^[4-6]. However, A. Momot^[7] concluded that $\text{Al}_{\text{Zn}}\text{-Zn}_i$ complexes constitute the shallow donors leading to the achieved high conductivity of Al: ZnO nano-powder by using Raman, NMR and the conductivity measurements and first-principles calculations. The above authors pointed out that the Al ions in the interstitial position migrate to the lattice position of Zn and generate interstitial Zn (Zn_i), forming a complex of Al_{Zn} and Zn_i . This particular defect structure increases the number of charge carriers and thus improves the conductivity. In the previous chapters, we prepared ZnO ceramics doped with Al_2O_3 , TiO_2 and MgO , leading to a high conductivity ($1.52 \times 10^5 \text{ S}\cdot\text{m}^{-1}$) for sintering in a reducing atmosphere. The effects of the three doping elements, sintering atmospheres, and sintering methods on the phase structure, micromorphology, defect characteristics, and electrical properties of ZnO-based ceramics were also studied. The relationships between the corresponding properties and structures were revealed. Thus, it was shown that the reducing sintering atmosphere of $\text{N}_2 + \text{CO}$ can decrease the Schottky barrier at the grain boundary by reducing the intrinsic acceptor defect at the grain boundary in ZnO ceramics, thereby increasing the carrier mobility. At the same time, the reducing sintering atmosphere can also increase the solid solubility of Al ions which favors high charge carrier concentrations. Therefore, the increase in the carrier mobility and

the concentration together lead to an increase in the conductivity. In addition, Al_2O_3 doping represents the key dopant for increasing the conductivity of ZnO-based ceramics. The analysis of chapter 5 has shown that Al^{3+} ions contribute to the formation of shallow donors as $Al_{Zn}-Zn_i$ complexes which provide a high charge carrier concentration. This leads to the Knight shift effect observed on the NMR spectra which is consistent with the involvement of $Al_{Zn}-Zn_i$ complexes in the high conductivity of ZnO ceramics^[8, 9].

However, in the NMR spectrum of ZnO:Al nanoparticle powder studied by A. Momot and the NMR spectrum obtained from the test of ZnO-based ceramics in our research, the NMR lines associated with tetra-coordinated Al at 80 ppm are very different: the intensity of this NMR line of nanoparticle powder is much higher than the corresponding NMR line intensity of the ceramics in our work, thus we expect the defects distribution is different between Al doped ZnO ceramics and nanoparticles. In addition, in the work of the former three chapters, we focused on the defect structure of ZnO ceramics without in-depth analysis of the environmental structure of Al and the formation process of $Al_{Zn}-Zn_i$ complexes in ZnO. In order to further explore these issues, it is necessary to analyze the influence of the surface structure state of ZnO powder and establish its relationship with ZnO-based ceramic materials.

Thus, the main objective of the present work deals with the correlation between the microstructures of the ceramics and tiny particles samples and the NMR and EPR signatures of the involved active electronic defects. Therefore, the ZnO based ceramics were crushed to particles with different sizes from about 100 microns down to 0.2 microns scaled by using manual grinding or mechanical by high energy ball milling process. The manually ground particles reflect the properties of ceramics, while the ball milled particles are made of very tiny ZnO particles, and therefore have more surface states. The relation between the defects structure and the local electrical conductivity will be searched by investigating the evolution of the aluminum environment as function of the particle sizes. The approach is thought to ensure consistent understanding of the correlation between the defect structures, the microstructures and the electrical conductivity in the underlying ZnO based samples.

6.2 Sample preparation and characterization

ZnO based ceramics ($\text{ZnO} + 0.25 \text{ mol\% Al}_2\text{O}_3 + 0.50 \text{ mol\% TiO}_2 + 1.00 \text{ mol\% MgO}$) were synthesized by the conventional solid-state reaction method. ZnO ceramic pellets, with 12 mm diameter and 1mm thickness, were obtained by sintering them at 1200 °C for 2 hours in N_2+CO , referred as ‘C’. To compare the properties of the initial ceramic to particles with different sizes, manual and ball milling grindings were performed. Microparticle ceramics in the particle range 10 μm -100 μm were obtained by manual grinding, referred as ‘M’, and smaller size particles about 0.2 μm were obtained by mechanical ball milling for 4 hours, named ‘B’, with microparticles’ characteristics.

The I-V curve of ZnO ceramic samples is measured by self-assembly resistance test equipment. The morphology of ceramic samples and powder samples is measured by SEM and TEM. The particle size distribution of powder samples is evaluated by a Mastersizer 3000 laser particle size analyzer. The structural characteristics of defects are characterized by Raman, EPR, and NMR. The corresponding experimental parameters are detailed in the Chapter 2.

6.3 Morphology and size analysis of particles

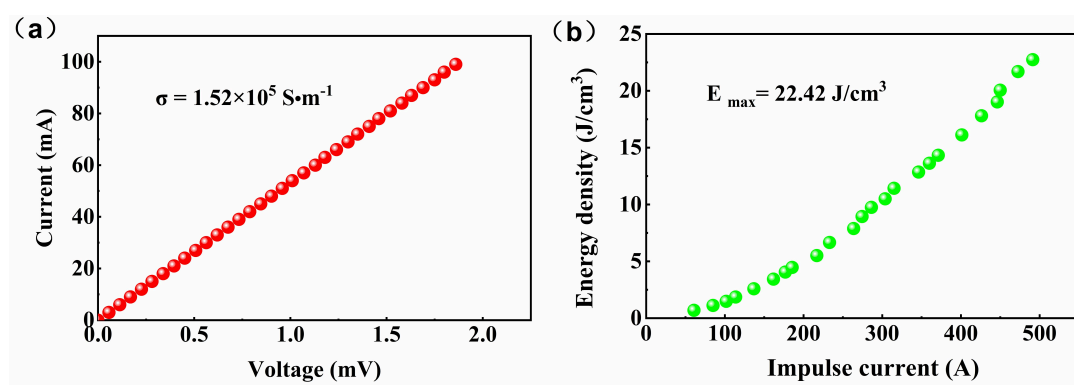


Figure 6.1 (a) I-V curve and (b) Energy density vs. impulse current of as-synthesized ZnO ceramic

The I-V curve of ZnO ceramic shown in Fig. 6.1a, shows a linear characteristic within

the measured current range (0-100 mA). The achieved electrical conductivity in bulk ZnO ceramics is as high as ($1.52 \times 10^5 \text{ S} \cdot \text{m}^{-1}$). A pulse lightning strike experiment was carried out on this ceramic sample, and the curve of energy density with impact current is shown in Figure 6.1b. The maximum energy density ($22.42 \text{ J} \cdot \text{cm}^{-3}$) was obtained when the ceramic was broken down. Therefore, the ceramic sample C has very good electrical properties.

The ceramic pellets were crushed into different size particles to investigate the role of local order and electronic defects in ZnO. SEM images in Fig. 6.2 show the microstructures of ceramic and particles and the distributions of the particle sizes of samples **M** and **B**. The schematic microstructures and specific surfaces of the samples are depicted in Fig. 6.3. For sample **M**, the grain sizes in the range (10-100 μm) are larger than the grain ($\sim 10 \mu\text{m}$) involved in ZnO ceramics indicating the low grinding efficiency which does not impact too much the initial grains structure. Thereafter, the properties of ZnO ceramics will be coherently obtained on the sample **M**. For the sample **B**, the particles' sizes distributed in the range (0.2-2 μm) are smaller than for the initial ZnO grains ($\sim 10 \mu\text{m}$). As a consequence, ZnO grains sizes are well reduced after ball milling as indicated by TEM image inserted in Fig. 6.2c and the obtained particles in the sample **B** show increased specific surface. The resulting samples must reflect the defects concentration and the local order states in finely divided ZnO ceramics. Therefore, the structural properties between ceramics and powder could be indirectly deduced from comparing the properties of samples **M** and **B**.

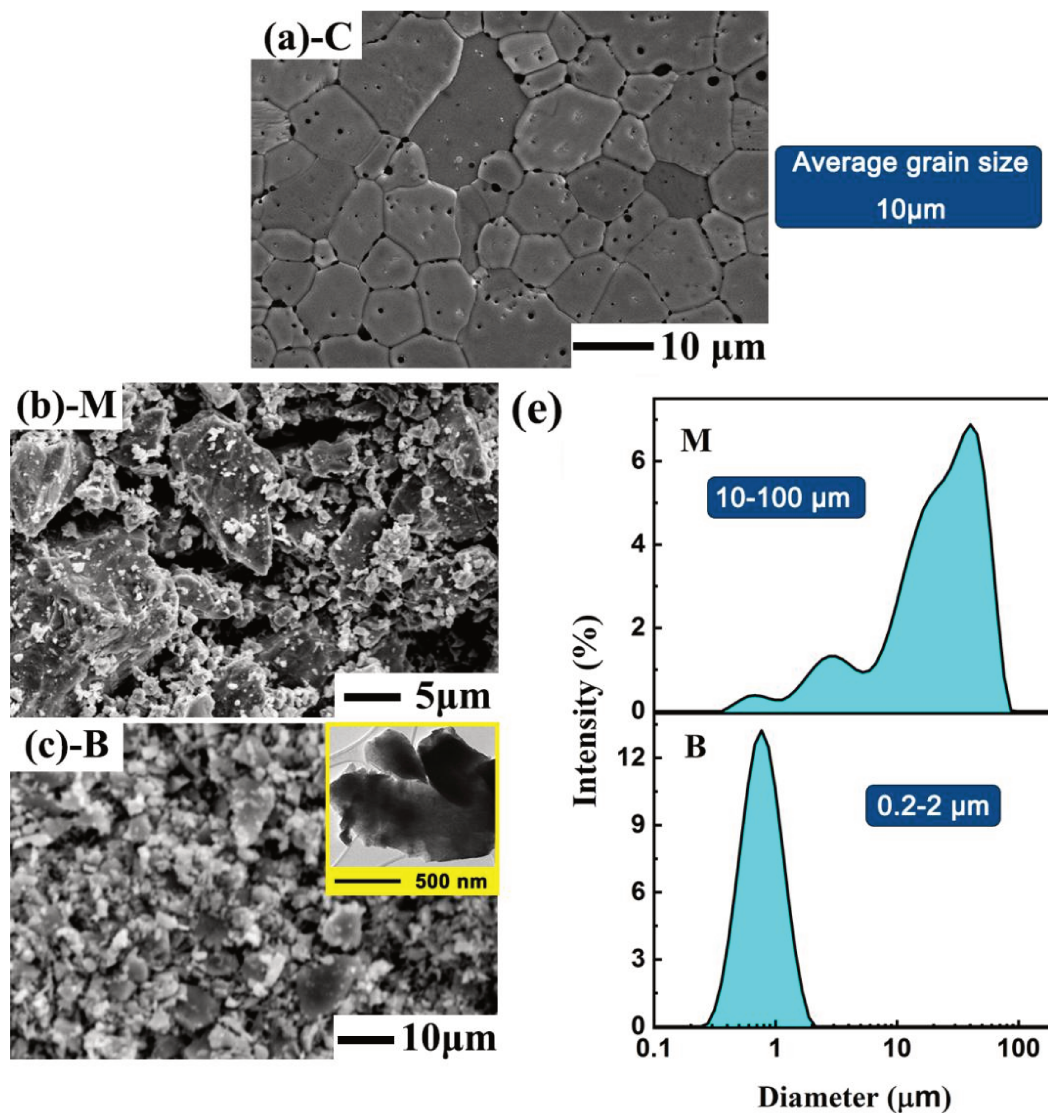


Figure 6.2 Size and size distribution of samples M and B

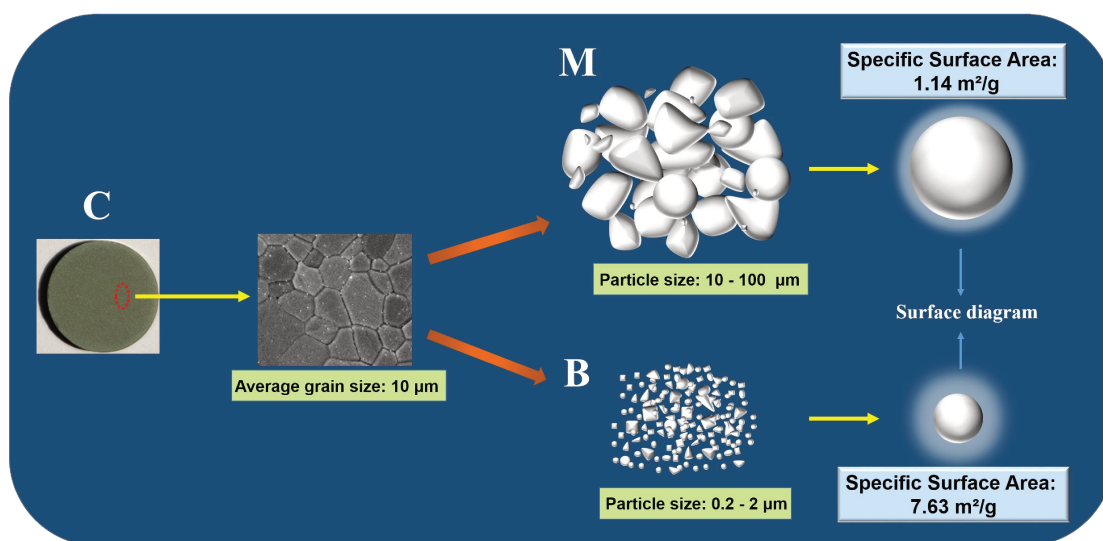


Figure 6.3 The schematic diagram of the crushed particles

6.4 Structural studies

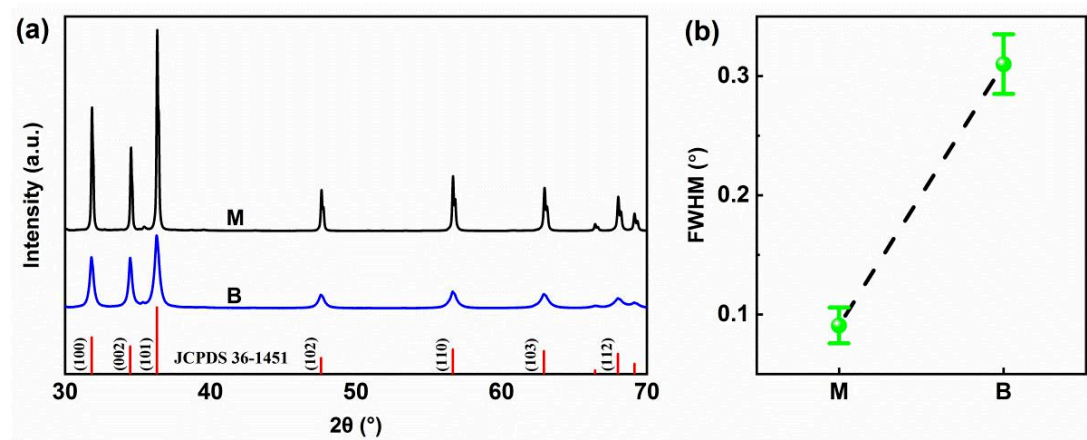


Figure 6.4 (a) X-ray diffraction patterns, (b) FWHM of (101) peak for samples M and B

XRD patterns reported in Fig. 6.4 show that the main phase in both samples **M** and **B** is wurtzite ZnO (JCPDS No. 36-1451). For the sample **B**, the intensity of all XRD diffraction lines is lowered along with an increase of the full width at half maximum (FWHM) of for (101) line. This behavior is related to the low crystalline quality of the **B** sample caused by the ball milling. Indeed, this mechanical ball milling process contributes to lower the particle sizes and increases the structural disorder, which can also be reflected from the Raman results. As shown in Fig. 6.5, Raman spectra were reported with a normalization of the intensity of the active Raman modes according to the E_2^{high} peak. Similar features of the lineshape related to E_2^{high} mode is attributed to the local structural disorder and reduced the translational symmetry^[10] and these features depend on particle sizes. As reported in Fig. 6.5, the more pronounced band around 500 cm^{-1} shown in sample **B** is assigned to the activation of B_1 mode by structural disorder^[11]. As discussed in our former work^[9] the disorder consists in increasing Zn interstitials (Zn_i), which is lower after ball milling. Meanwhile, the decrease of $A_1(\text{TO})$ mode at 382 cm^{-1} related to oxygen vacancies (V_O)^[12] indicates that the ratio of V_O is decreased by ball milling. Zn_i and V_O defects are mainly distributed in the grain boundaries of ZnO ceramics^[13] both of them are decreased by the ball milling process due to damage of the grain boundaries. A further

comprehensive analysis is carried out below by using the local probe methods such as EPR and NMR experiments.

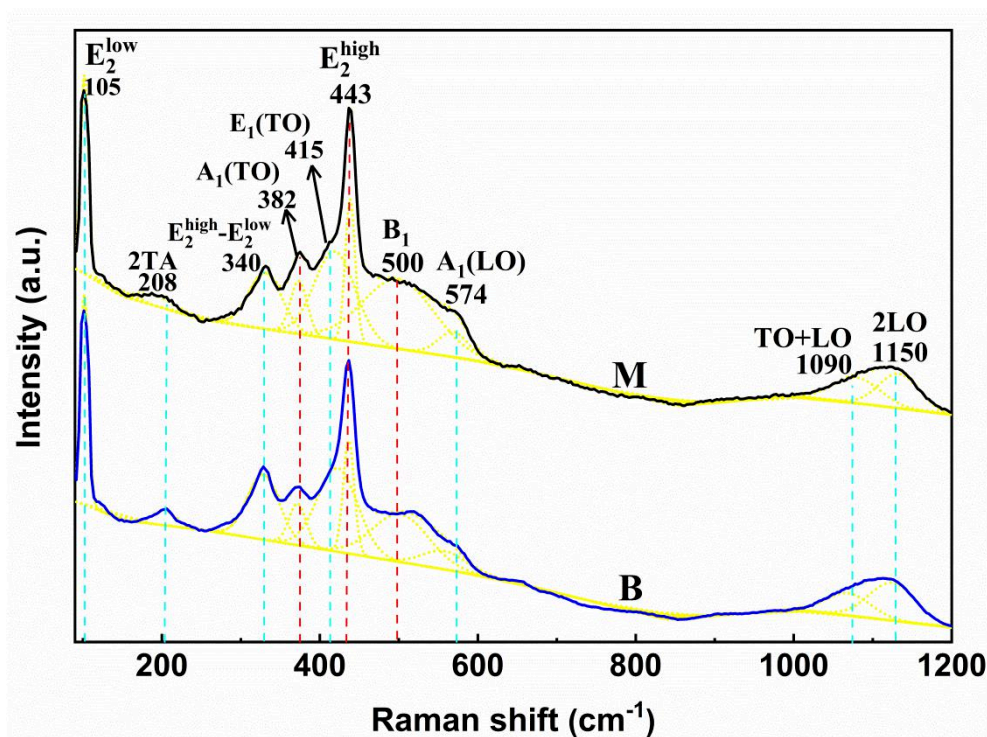


Figure 6.5 Raman spectra for samples M and B

6.5 Electronic active defects probed by EPR

In Fig. 6.6a, the single resonance line with the g factor at 1.960(2) is a characteristic of an EPR fingerprint related to Zn_i ^[4]. The EPR signature in the sample **M** where the conductivity remains important is highly different from that of sample **B** with limited charge carriers due to smaller particles. In this case, the space reduction may decrease drastically the mobility of charge carriers as demonstrated in other families of semiconductors^[14]. As the EPR line width is correlated with the electrical conductivity, the sample **M** is more conductive than sample **B** (Fig. 6.6b). The thermal evolutions depicted in the range 160K-300 K (Fig. 6.6b and 6.6c) shows the EPR line width (ΔH) and the integrated line intensity (Π_{EPR}) defined as $\Pi_{\text{EPR}} \sim I_{\text{EPR}} * (\Delta H)^2$ with I_{EPR} the line intensity. Π_{EPR} follows the well-known Curie law involved for localized and non-interacting paramagnetic centers, which is the characteristic of the sample **B**. The

observed thermal behavior shows a nearly stationary Π_{EPR} for the sample **M**, suggesting the existence of Pauli-like spin susceptibility induced by delocalized electrons. Moreover, ΔH in the sample **B** remains constant when increasing the temperature while a linear increase is observed for ΔH in sample **M** as it may occur when conduction electrons contribute to the relaxation of the paramagnetic species, which is Korringa relaxation. The thermal behaviors of the spectral parameters is consistent with a high density of conduction electrons leading to the involvement of Pauli spin susceptibility in the integrated line intensity and to the particular relaxation mechanism evidenced by EPR line width. The fact that the sample **M** shows less paramagnetic species concentration (Fig. 6.6c) can be understood by a high mobility and short relaxation times which limit their contribution to the EPR signal. Thus the intensity of the EPR line may reflect only the localized paramagnetic species in the the sample **M**. The low concentration of paramagnetic species in large sized particles (sample **M**) compared to the smaller one (sample **B**) is coherent with a higher mobility of paramagnetic species in large domains limiting their effective concentration probed by EPR. Thus, the EPR studies of different size samples may inform on the correlation between the paramagnetic species features and the confinement effect which occurs in small sized particles. The decrease in the mobility in sample **B** particles may be due to the confinement of charges and to the backscattering which occurs on the particle boundaries as outlined in a nanostructured system by Richter and Schmuttenmaer^[15]. Therefore, some defects and boundaries in the surface area of sample **B**, as a scattering region, have an effect to inhibit carrier transport and to decrease conductivity.

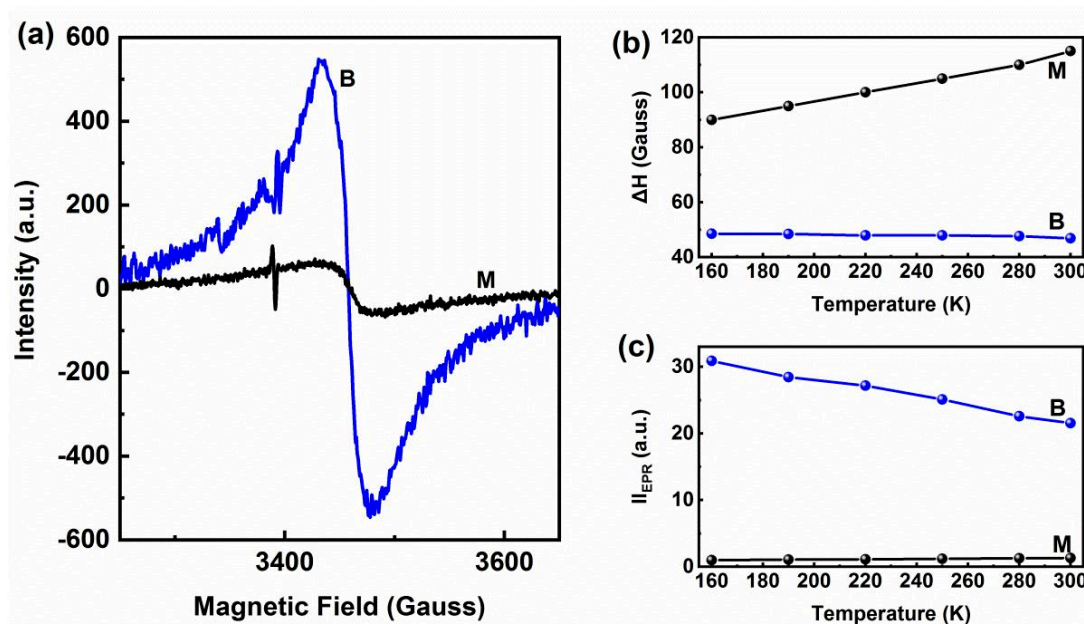


Figure 6.6 (a) EPR spectra and thermal evolution of linewidth (ΔH)-(b) and integrated intensity (I_{EPR})-(c) for samples M and B

6.6 Local environment probing of Al ions

In order to characterize the size effects on the NMR signals as it was done for the EPR experiments, we compared the NMR spectra of the samples **M** and **B**. For the environment of ^{27}Al , there are three different coordinated Al in ZnO from the NMR analysis in Fig. 6.7. The six-coordinated Al (Al^{VI}) is associated to the NMR line at 5 ppm, while the four-coordinated Al (Al^{IV}) gives rise to the 80 ppm line. In addition, the NMR line at 185 ppm is accounted by the Knight Shift (KS) effect related to $\text{Al}_{\text{Zn}}\text{-Zn}_i$ complexes. The intensity of NMR lines shows different strengths depending on the considered samples M and B. With the particle size reduction, the NMR line related to Al(KS) decreases drastically while the NMR line for Al^{IV} increases simultaneously; the NMR line for Al^{VI} remains almost the same. Al doping tends to substitute Zn by Al ions in the lattice to form Al_{Zn} in ZnO, while an extended charge delocalization occurs from $\text{Al}_{\text{Zn}}\text{-Zn}_i$ complexes^[9]. Therefore the representative NMR line of Al_{Zn} is marked by the KS effect leading to the 185 ppm line rather than Al^{IV} line at 0 ppm in sample **M**. Besides, in the sample **B**, the low conductivity limits the

KS effect and favors the appearance of Al^{IV} line which rises at 80 ppm. This line growth occurs in detriment of the line affected by Knight Shift (KS) effect as illustrated in Fig. 6.8. The tiny particles of the sample **B**, with higher specific surface area favor the limitation of the extended electronic delocalization around the $\text{Al}_{\text{Zn}}\text{-Zn}_i$ complexes. The density of such defects is expected to decrease with an increased surface area of the **B** sample as sketched in Fig. 6.8. The net effect from this reorganization by ball milling consists in a weaker KS effect. From the analysis of Raman, EPR and NMR spectra, we may speculate that $\text{Al}_{\text{Zn}}\text{-Zn}_i$ complexes induce strong Knight Shift effect in the highly conductive Al doped bulk ZnO. Confinement effect and lowering density of the electronic active $\text{Al}_{\text{Zn}}\text{-Zn}_i$ complexes in finely divided the sample **B** overcome the conductivity and allow a clear evidence of the four coordinated Al in ZnO grains.

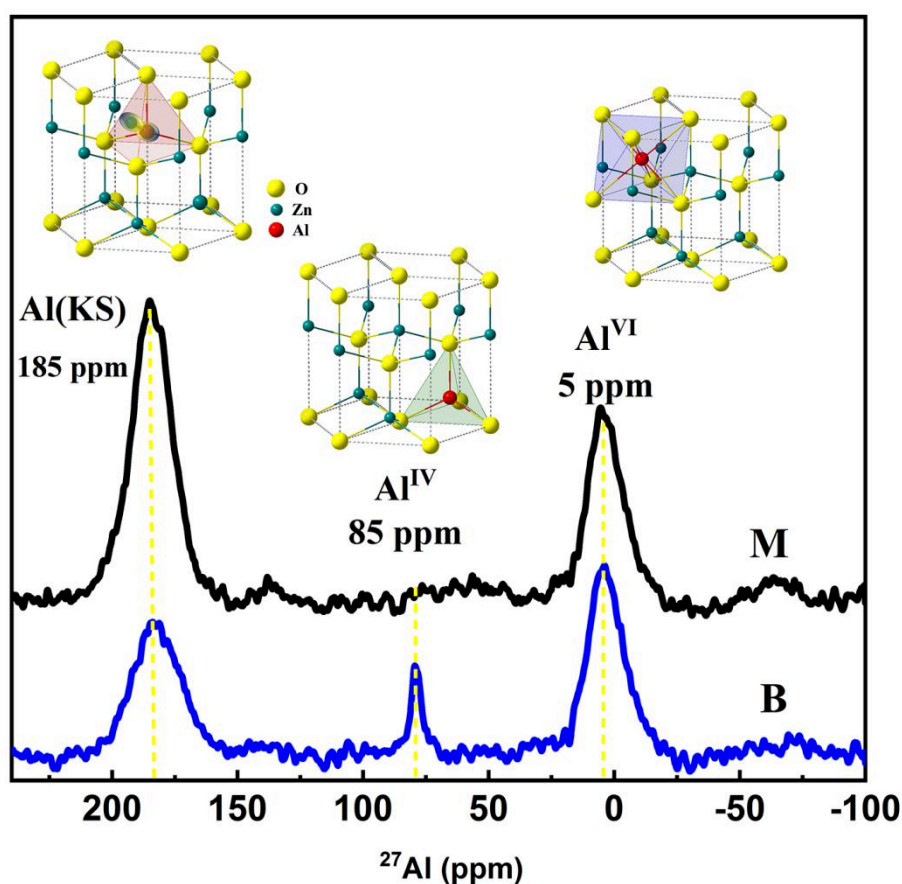


Figure 6.7 ^{27}Al MAS NMR spectra of samples M and B

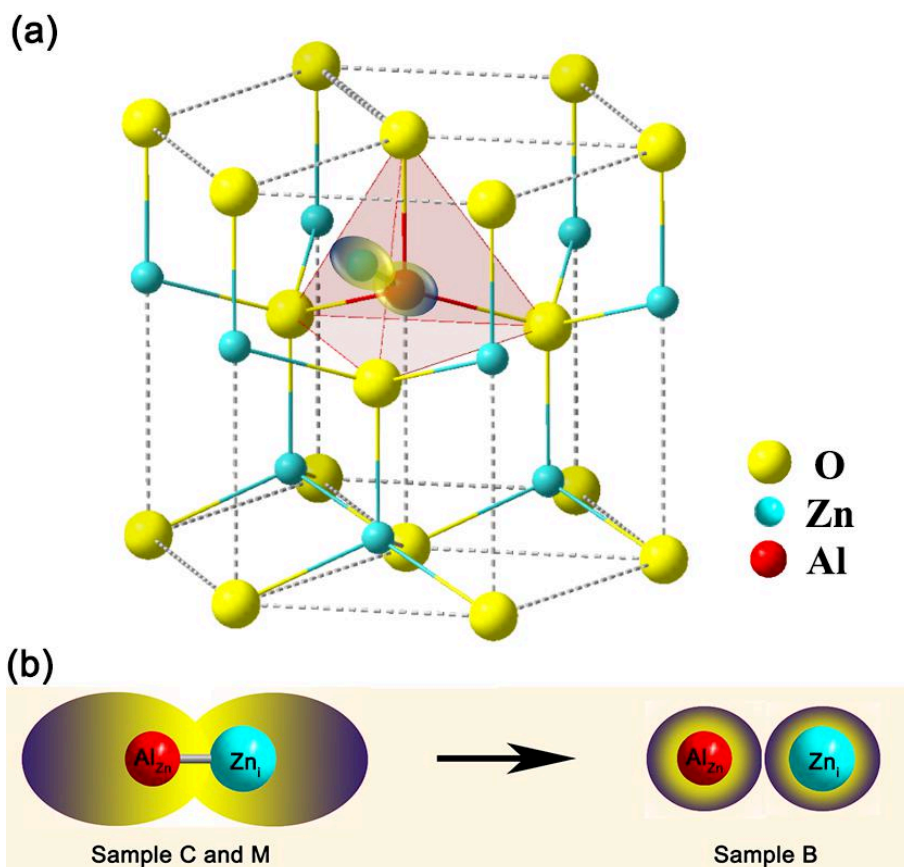


Figure 6.8 (a) Schematic diagram of substitutional Al^{3+} - interstitial Zn^{2+} ($\text{Al}_{\text{Zn}}\text{-Zn}_i$) in ZnO. (b) The KS effect evolution and the environment of $\text{Al}_{\text{Zn}}\text{-Zn}_i$ complex and Al_{Zn} , Zn_i for samples.

6.7 Conclusion

1. In order to further explore the coordination environment of Al and study the correlation between defects ($\text{Al}_{\text{Zn}}\text{-Zn}_i$ complex, Al_{Zn} and Zn_i), local disorder, and electrical conductivity, ZnO ceramics were finely divided by manual grinding and ball milling. Particles with different sizes reflect the characteristics of ZnO ceramics and ultra-fine powders, respectively. The broadening and the intensity decrease of the ZnO characteristic (101) peak in the XRD diffraction patterns and the broadening of the ZnO characteristic E_2^{high} peak in the Raman spectra confirm that ball milling increases the local disorder in the ZnO ceramics.
2. According to the conduction behavior, large sized particles favor the formation of $\text{Al}_{\text{Zn}}\text{-Zn}_i$ complexes with extended electronic density leading to high electrical

conductivity up to $10^5 \text{ S}\cdot\text{m}^{-1}$ as also involved in bulk ceramics. Oppositely, low particles sizes with higher specific surfaces did not show a high density of $Al_{Zn}-Zn_i$ complexes and then the electrical conductivity is quite low.

3. From the NMR spectra analysis, the four oxygen-coordinated Al_{Zn} develops in the ZnO ultrafine particles after ball milling, but not in the ZnO ceramic particles. The Knight shift effect induced in highly conducting ZnO ceramic particles lead to a particular NMR line at 185 ppm far from any known oxygen coordinated ^{27}Al while the four oxygen coordinated Al being almost disappeared. The formation of small particles by ball milling overcame the stability of $Al_{Zn}-Zn_i$ complexes and the involvement of the related electronic distribution. This fact limits the conductivity and the KS effect leading to resolved NMR line associated to four oxygen coordinated ^{27}Al .
4. The involved defects structures were pointed out by EPR spectroscopy as function of ZnO grain sizes. The EPR signal assigned to Zn_i defects is characterized by different line intensities and widths depending on the microstructures features. The low line integrated intensity reflects the low concentration of paramagnetic defects in the highly conducting system with higher density of $Al_{Zn}-Zn_i$ complexes. The easy delocalization of charge carriers in high particle sizes limits their contribution to the EPR signal. Oppositely, the less conducting tiny particles sample shows a higher concentration of paramagnetic centres due to less effect from the conduction electrons on the relaxation mechanism which alter the EPR line.
5. The performed experiments dealing with the structural and local order analysis of the doping element coordination and electronic defects contribute to consistent analysis of the correlation between the microstructures and the electrical behavior in Al doped ZnO structures.

6.8 Reference

- [1] Q. Sun, G. Li, T. Tian, et al. Co - doping effects of (Al, Ti, Mg) on the microstructure and electrical behavior of ZnO based ceramics. *J Am Ceram*

- Soc[J]. 2020;103:3194–204.
- [2] H. Kaga, Y. Kinemuchi, H. Yilmaz, et al. Orientation dependence of transport property and microstructural characterization of Al-doped ZnO ceramics. *Acta Mater*[J]. 2007;55(14):4753-7.
- [3] Y. Jing, N. Luo, S. Wu, et al. Remarkably improved electrical conductivity of ZnO ceramics by cold sintering and post-heat-treatment. *Ceram Int*[J]. 2018;44(16):20570-4.
- [4] S. Hartner, M. Ali, C. Schulz, et al. Electrical properties of aluminum-doped zinc oxide (AZO) nanoparticles synthesized by chemical vapor synthesis. *Nanotechnology*[J]. 2009;20(44):445701.
- [5] A. Sedky, A. Al- Sawalha, A. Yassin. Enhancement of electrical conductivity by Al-doped ZnO ceramic varistors. *Physica B*[J]. 2009;404(20):3519-24.
- [6] K. Cai, E. Müller, C. Drašar, et al. Preparation and thermoelectric properties of Al-doped ZnO ceramics. *Mater Sci Eng B-Adv*[J]. 2003;104(1-2):45-8.
- [7] A. Momot, M. Amini, G. Reekmans, et al. A novel explanation for the increased conductivity in annealed Al-doped ZnO: an insight into migration of aluminum and displacement of zinc. *Physical chemistry chemical physics : PCCP*[J]. 2017;19(40):27866-77.
- [8] Q. Sun, G. Li, T. Tian, et al. Controllable microstructure tailoring for regulating conductivity in Al-doped ZnO ceramics. *J Eur Ceram Soc*[J]. 2020;40(2):349-54.
- [9] Q. Sun, T. Tian, L. Zheng, et al. Electronic active defects and local order in doped ZnO ceramics inferred from EPR and ²⁷Al NMR investigations. *J Eur Ceram Soc*[J]. 2019;39(10):3070-6.
- [10] T. Tian, L. Zheng, X. Ruan, et al. Disorder-induced localization in doped ZnO by different sintering atmosphere. *Ceram Int*[J]. 2018.
- [11] S. Sharma, R. Bayikadi, P. Swaminathan. Spark plasma sintering route to synthesize aluminium doped zinc oxide. *RSC Adv*[J]. 2016;6(89):86586-96.

- [12] S. Olive-Méndez, C. Santillán-Rodríguez, R. González-Valenzuela, et al. Role of vanadium ions, oxygen vacancies, and interstitial zinc in room temperature ferromagnetism on ZnO-V₂O₅ nanoparticles. *Nanoscale Res Lett*[J]. 2014;9(1):169.
- [13] Raphael Lucas de Sousa e Silva, A. Franco. Effect of porosity on dielectric properties of ZnO ceramics. *Journal of the European Ceramic Society*[J]. 2020;40(4):1307-11.
- [14] B. Alberding, A. Biacchi, A. Hight Walker, et al. Charge carrier dynamics and mobility determined by time-resolved terahertz spectroscopy on films of nano-to-micrometer-sized colloidal Tin(II) monosulfide. *J Phys Chem C*[J]. 2016;120(28):15395-406.
- [15] C. Richter, C. Schmuttenmaer. Exciton-like trap states limit electron mobility in TiO₂ nanotubes. *Nature nanotechnology*[J]. 2010;5(11):769-72

Chapter 7

General Conclusions and Perspectives

7.1 General Conclusions

The research works developed in the frame of this thesis were devoted to the preparation and characterization of ZnO-based conducting ceramics doped with Al₂O₃, TiO₂ and MgO. By adjusting the sintering atmosphere, sintering method and doping ratios, ZnO-based ceramics with ultra-high electrical conductivity were realized. In a first step, the effects of three sintering atmospheres (air, N₂, CO + N₂) on the structure and electrical properties of doped ZnO ceramics were investigated. The highest conductivities were obtained by using (CO + N₂) reducing atmosphere and deep analyses of the conduction mechanisms were performed. Secondly, the effects of Al₂O₃ on the phase structure, micromorphology, defect types and electrical properties of ZnO-based ceramics were systematically studied by changing the doping ratio of Al₂O₃. ZnO ceramics with different electrical conductivity were obtained with different Al₂O₃ doping ratios. The correlation was drawn between the structural modifications due to substitutional Al ions and the electrical properties of ZnO ceramics. In addition, the traditional muffle furnace solid-state sintering method and the new spark plasma sintering (SPS) method were used. The structure, morphology and electrical properties of the ceramics were compared for the two approaches and deep insight was drawn on the high conductivity achieved by the SPS sintering method. Then, through selective single-doping or co-doping of Al₂O₃, TiO₂, and MgO dopants, the effects of these three dopants on the phase structure, micro-morphology, lattice vibration characteristics, and types of electron-active defects of ZnO-based ceramics were systematically studied and the electrical properties analyzed. Finally, finely divided ZnO ceramics with different sizes were realized by manual grinding

and ball milling in the aim to analyze the effect on the electrical conductivity and the transport mechanism. Thus, we correlated the structure and the morphology of two samples with different grain sizes with the evolution of the coordination environment of Al and the types of defects that improve the conduction properties.

Based on the above research contributions, we summarize below the main relevant highlights on the role of doping, sintering atmospheres and microstructure to realize highly conducting ZnO-based ceramics:

1. ZnO ceramics doped Al₂O₃, TiO₂, and MgO were prepared by the solid-phase reaction method in air, N₂, and CO + N₂ sintering atmospheres with the aim to achieve the fabrication of dense ceramics with good crystal quality. Wurtzite ZnO phase and a small amount of secondary Zn₂TiO₄ spinel phase were contained in the ceramics. Moreover, the solid solubility of Ti in ZnO ceramics obtained by sintering gradually increased with the reducing nature of the used atmosphere. This effects is accompanied by the decrease of the spinel phase and thus weakens the pinning effect and favors the grain size growth of ZnO ceramics. The electrical conductivity increases when using air, N₂ and CO + N₂ as the sintering atmosphere. Thus, the highest conductivity $\sigma = 1.5 \times 10^5 \text{ S}\cdot\text{m}^{-1}$ was realized ZnO ceramic prepared under the CO + N₂ reducing atmosphere. From Raman studies, the appearance of Raman peaks around 500 cm⁻¹ indicates the disordered structures. This disorder is caused by the defects (Al_{Zn} and Zn_i) being consecutive to Al₂O₃ doping along with the sintering under CO + N₂ reducing atmosphere. In this case, EPR studies shows the occurrence of high concentrations of unpaired spins associated with shallow donor defects consisting in (Al_{Zn}, Zn_i) complexes. These defects, favored by the sintering under reducing atmosphere, ensure the charge carriers contributing to the enhanced in the corresponding ceramics with conductivity in the order of 10⁻⁵ S·cm⁻¹. In parallel, ²⁷Al-NMR spectra are characterized by an intense peak at 185 ppm which cannot be associated to any oxygen coordinated sites. The origin of this NMR line is caused by the Knight shift induced by the above mentioned charge carriers. In summary, ZnO ceramics sintered in a N₂ + CO reducing atmosphere induce the formation of Al_{Zn} and Zn_i, that is, Al_{Zn}-Zn_i complexes with a high concentration. As a main effect,

delocalized electronic densities are created in the underlying lattice which further enhance the electrical conductivity of ZnO-based ceramics.

2. By adjusting the Al₂O₃ doping ratio to 0.25 mol% used with a fixed ratio of TiO₂ and MgO and sintering in a N₂ + CO reducing atmosphere to realize co-doped ZnO ceramics, the best conductivity ($1.52 \times 10^5 \text{ S}\cdot\text{m}^{-1}$). The solid solubility of Al in ZnO is indeed well improved under N₂ + CO reducing sintering atmosphere. However, when the doping amount of Al₂O₃ exceeds the solid solubility, the generated ZnAl₂O₄ spinel phase acts as a pinning to limit the growth of ZnO grains and increase the number of grain boundaries. The insulating secondary spinel phase ZnAl₂O₄ can scatter electrons, reduce the carrier mobility, and then decrease the conductivity. Raman, EPR and NMR experiments have confirmed that the shallow donors as Al_{Zn}-Zn_i complexes induce highly delocalized electronic charge density distribution when doped with an appropriate amount of Al₂O₃.
3. Al₂O₃ doped ZnO ceramics were synthesized by two approaches, namely, the traditional muffle furnace sintering method and the novel spark plasma sintering (SPS) method. Exhaustive investigations were performed to correlate the microstructure with the electrical conductivity of the ceramics. The improved electrical performances were obtained by the SPS method due to the high higher charge carrier concentration which overcame the effect of a low mobility in such ceramics. Indeed, the rapid sintering process of SPS method induces a significant reduction in the ZnO grain size, and then a large increase in the number of grain boundaries. Such a microstructure contributes to an enhanced scattering of electrons, which reduces the carrier mobility in the ceramics. For the high charge carrier concentration, it can be justified by the improvement of the solid solubility of Al in ZnO by SPS method and an increased density of shallow donor defects such as the Al_{Zn}-Zn_i complexes.
4. Systematic studies were developed in the aim to identify the role of doping oxides Al₂O₃, TiO₂, and MgO on the physical features of ZnO based ceramics. This includes the doping effects on the phase structure, micromorphology, microstructure, electronic active defects and electrical properties of ZnO-based ceramics, and the relationship between structure and properties. Al, Ti, and Mg

single-doped and co-doped ZnO ceramics were fabricated by solid state reaction and sintered under air leading to good crystalline quality with the wurtzite ZnO structure. Due to the high solid solubility of Mg in ZnO, Mg does not introduce any second phase in contrast to Al, Ti, and (Al, Ti) doped ceramics where secondary phases, such as ZnAl_2O_4 , Zn_2TiO_4 , and $\text{Zn}_a\text{Ti}_b\text{Al}_c\text{O}_d$ spinel, were observed. The main effect of such spinel phases is to increase the density of grain boundaries in the major host ZnO-based ceramics. As consequence, a lowering of the conductivity was shown due to the insulating nature of spinel phases and the grain boundaries acting as barrier for the conduction channels. The Ti^{3+} ions generated in TiO_2 doped ZnO ceramics are deep donor defects and limit the charge delocalization and then no particular improvement was induced on the electrical conductivity. Similarly, for MgO doping, the same valence state and ion radius of Mg^{2+} and Zn^{2+} ions does not cause any noticeable change of the charge carriers; the electrical conductivity of Mg-doped ZnO ceramics remain low. Compared to Ti and Mg cases, Al-doped ceramics generate the highest achieved electrical conductivity. This behavior is induced by the large charge carrier concentration favored by Al doping. From structural consideration, the Raman mode B_1 , which is non-active in a perfect wurtzite structure, became well resolved in Raman spectra in Al-doped ceramics. This mode originates from defects such as Zn_i , which contribute to an increase of the disorder in the ZnO structure. From local order characterization, the ^{27}Al NMR line at the chemical shift 185 ppm of Al-doped ZnO ceramics is caused by the Knight shift induced by the conduction electrons of particular structural defects such as $\text{Al}_{\text{Zn}}\text{-Zn}_i$ complexes. Due to delocalized electron density around these defects, they contribute efficiently to the electronic properties and improve the conductivity of Al-doped ZnO ceramics. Meanwhile, ^{67}Zn NMR spectra show modification on the local environments of Zn nuclei in Al-doped ZnO ceramics in agreement with the conclusion from Raman studies which show the activation of B_1 modes by Zn_i defects.

5. The microstructure defined by the morphology of grains and the density of grain boundaries play critical role in the electrical properties of the doped ZnO ceramics. In this context, an experimental approach was developed on grounded

ceramics to form powders with different grain sizes where the grain boundary distributions are also modified. Thus, particles with different sizes were prepared by manual grinding and also by high energy ball milling technique. The microstructures of different powders were then investigated on two representative samples from each preparation method. Thus, for the manually grounded powder, an average particle size is quite larger compared to the grains involved in the bulk ceramic. For the finely divided powder by using ball milling, the average particle size which was found quite smaller than the grain sizes in the bulk ZnO ceramic. For the grain boundary distributions, the two considered powders reflect the characteristics of bulk ZnO ceramics and ultrafine ZnO powders. From structural investigations, the broadening of the (101) characteristic peak of ZnO in the XRD pattern and the broad bands of the characteristic modes of ZnO structure in the Raman spectrum confirmed that ball milling favors the formation of a local disorder in ZnO. The EPR signal assigned to Zn_i defects is characterized by different line intensities and widths depending on the microstructures features. The easy delocalization of charge carriers in as in bulk ZnO limits their contribution to the EPR signal and then the effective concentration of paramagnetic species is low. Oppositely, the higher concentration of paramagnetic species probed by EPR in the ultrafine ZnO powder is due to the low mobility of the charge carriers by the particle boundaries. In the NMR spectra, the four-coordinated Al_{Zn} appears only in the ZnO ultrafine powder, but not in the large sized ZnO ceramic particles. This result indicates that in addition to the defects of Al_{Zn} - Zn_i complexes, a part of Al ions exists in ZnO as Al_{Zn} defects in the ball milling particles. According to the conduction behavior, large sized particles favor the formation of Al_{Zn} - Zn_i complexes with extended electronic density leading to high electrical conductivity up to $10^5 \text{ S}\cdot\text{m}^{-1}$ as also involved in bulk ceramics. In ZnO ultrafine particles, the Knight shift effect is limited due to the low conductivity in the underlying network and then the 185 ppm NMR line exhibits lower intensity as observed experimentally.

7.2 Perspectives

These thesis works contributed to exhaustive studies of physical properties and their

analysis in Al_2O_3 , TiO_2 and MgO-doped ZnO-based conducting ceramics. However, some directions of studies are worthy of interest and able to bring complementary insights on the considered systems as outlined below:

1. The performed analysis identifies the structural characteristics and the charge carriers features that affect the electrical conductivity of ZnO ceramics. Although, the donor defect $\text{Al}_{\text{Zn}}\text{-Zn}_i$ complexes located in ZnO grains contribute efficiently to the electrical conductivity, the structure of grain boundaries requires deep insights. On the other hand, the structure of defect types and defect distributions in ZnO grains and at the grain boundaries affect the transport process in the ceramics. In relation with such aspects, the fabrication and studies of finely divided powders up to nanostructured particles are relevant to understand the role of grain boundaries and surface effects on the electronic transport features.
2. In this thesis, exhaustive structural studies and their analysis in ZnO-based ceramics prepared by different approaches (solid state solution, SPS sintering) have been performed. This includes phase structure identification, vibrational features correlated with the disorder induced by doping, electronic active defects, and defects environment, etc. However, few insights were devoted to the electrical performances and limitations by analyzing their linearity, power density, inductance, capacitance, in the aim to explore the potential workable processes.
3. From the carried out studies, it is undeniable that the structures of defects structural or electronic active centres introduced by doping or intrinsically induced by the fabrication processes are key parameters acting on the crystalline quality, structural defects, disorder and on the electronic properties. The carried out investigations and analysis have contributed to understand the main trend correlating the structural features, doping and the achieved properties. However, modelling of the defect structures and their simulation by dedicated numerical approaches are highly relevant to characterize quantitatively the processes leading to the high conductivity of these systems by defect engineering. This theoretical and numerical approach was tentatively initiated during the present thesis works but deserves detailed studies.

List of Figures

Figure 1.1	(a) The wurtzite ZnO structure, (b) The wurtzite ZnO unit cell.....	5
Figure 1.2	(a) Band structure and (b) Partial density of states (PDOS) for ZnO.....	5
Figure 1.3	Schematic diagram of the microstructure of ZnO conductive ceramics...	7
Figure 1.4	ZnO grain boundary structure: (a) conductive ceramic, (b) varistor.....	8
Figure 1.5	Schematic diagram of ZnO grain boundary barrier.....	9
Figure 1.6	Schematic of the pinning effect of spinel on grain growth.....	11
Figure 1.7	Schematic diagram of (a) Model of percolation conductivity, (b) Schematic of equivalent circuit of ZnO conductive ceramics.....	12
Figure 1.8	Resistivity versus temperature for typical metals-(a) and typical semiconductors-(b).....	14
Figure 1.9	Current versus voltage curve of ZnO varistors.....	15
Figure 1.10	Schematic diagram of the electronic energy levels of main defects involved in ZnO.....	17
Figure 2.1	The experimental process image of the thesis.....	43
Figure 2.2	Schematic comparison of (a) two-point and (b) four-point method.....	45
Figure 2.3	Schematic diagram of self-assembly test resistance measurement equipment.....	46
Figure 2.4	(a) Pro4 four-point probe test system, (b) Four probe head.....	47
Figure 2.5	Schematic diagram of the Hall effect principle (a) Carriers are electrons (N-type) (b) Carriers are holes (P-type).....	48
Figure 2.6	Schematic diagram of material-electron interaction.....	51
Figure 2.7	Scanning electron microscope.....	51

Figure 2.8	Transmission electron microscope.....	52
Figure 2.9	Schematic diagram of Bragg diffraction.....	53
Figure 2.10	PANalytical-Empyrean X-ray diffractometer.....	54
Figure 2.11	(a) Molecular scattering energy level diagram (b) Scattering spectrum diagram.....	56
Figure 2.12	XploRA Raman spectrometer from HORIBA Company.....	57
Figure 2.13	Schematic of Electron Paramagnetic Resonance, the magnetic field is swept and induces splitting of the energy of spin states. At the resonance conditions, absorption of microwave power with fixed frequency provokes a transition between the spin states. The EPR line is the derivative of the microwave absorption curve.....	58
Figure 2.14	Electron paramagnetic resonance spectrometer.....	59
Figure 2.15	Schematic diagram of NMR spectrometer.....	60
Figure 2.16	NMR spectrometer.....	61
Figure 3.1	XRD patterns of ZnO-doped ceramics (A, N, C).....	66
Figure 3.2	SEM images of doped ZnO ceramics (A - (a), N - (b), C - (c)). (d) and (e) : atomic ratios involved in the zones 1 and 2 of sample A by EDS analysis, (f) : average grain size.....	68
Figure 3.3	(a) Electrical conductivity of ZnO based ceramics (A, N, C) at room temperature and (b) (TCR) coefficients in the temperature range -50 °C to +150 °C.....	70
Figure 3.4	(a) Raman spectra and (b) the enlarged region from 300 to 600 cm ⁻¹ for the undoped ZnO (Z) and for samples A, N and C.....	71
Figure 3.5	(a) EPR spectra in doped ZnO based ceramics. (b) Variation of the EPR signal features, line width and integrated intensity, versus the macroscopic electrical conductivity, (c) Thermal evolution of the EPR line integrated intensity and (d) Thermal evolution of the EPR line width	

	for samples.....	75
Figure 3.6	Local host sites for Al doping (red spheres-O, green spheres-Zn, blue spheres-Al): (a) Substitutional Al^{3+} - Interstitial Zn^{2+} ($\text{Al}_{\text{Zn}}\text{-Zn}_i$), (b) Interstitial Al^{3+} (Al_i), (c) Substitutional Al^{3+} (Al_{Zn}).....	75
Figure 3.7	(a) ^{27}Al MAS NMR spectra, (b) The peak spectra intensities at 0 and 185 ppm for samples A, N and C.....	77
Figure 3.8	(a) EPR signal spectra before and after annealing at 100 °C, (b) ^1H NMR spectra for sample A.....	79
Figure 4.1	(a) Electrical conductivity (σ) and (b) Temperature coefficient of resistance (TCR) for the investigated Ai samples.....	90
Figure 4.2	(a) Carrier concentration (n) and (b) Carrier mobility (μ) of samples....	91
Figure 4.3	(a) XRD patterns of ZnO ceramics with ZnO JCPDS card: No. 36-1451, (b) focus on $2\theta \sim (35^\circ\text{-}37^\circ)$ to highlight the content from spinel phases, (c) (d) Lattice parameters (a and c for ZnO-(c), for Zn_2TiO_4 -(d)).....	92
Figure 4.4	SEM images of doped ZnO ceramics (A1-a, A2-b, A3-c, and A4-d), (e) (f) (g) EDS analysis for area 1 and 2 on sample A2, (h) Average diameter of samples.....	94
Figure 4.5	TEM images of samples with the corresponding fast Fourier transform (FFT) patterns of neighboring grains.....	95
Figure 4.6	Raman spectra of samples.....	96
Figure 4.7	(a) ^{27}Al MAS NMR spectra of different samples. (b) The peak spectra intensities at 0 ppm, 185 ppm and the sum for samples.....	98
Figure 4.8	Schematic diagram of the environment of Al in ZnO: (a) Interstitial Al^{3+} (Al_i), (b) Substitutional Al^{3+} (Al_{Zn}), (c) Substitutional Al^{3+} - Interstitial Zn^{2+} ($\text{Al}_{\text{Zn}}\text{-Zn}_i$).....	98
Figure 4.9	Relation between the sample conductivity and the intensity of NMR-185ppm peak.....	99

Figure 4.10	XRD patterns of A-SPS and A samples.....	101
Figure 4.11	SEM images of sample A (a) and A-SPS (b).....	101
Figure 4.12	Electrical conduction properties for A-SPS and A samples.....	102
Figure 4.13	Raman spectra for sample A-SPS and A.....	103
Figure 4.14	UV-vis absorption spectra for sample A-SPS and A, the inset shows curves between $(\alpha h\nu)^2$ versus $h\nu$	105
Figure 4.15	(a) Photoluminescence spectra for sample A-SPS and A, (b) Energy level diagram of the defects corresponding to the spectra.....	105
Figure 5.1	(a) XRD patterns of as-synthesized samples, (b) The enlarged figure highlights the behavior of the spinel phase diffraction lines.....	116
Figure 5.2	(a) The FWHMs of ZnO (101) peak. (b), (c) The lattice parameters a and c of ZnO, (d) The FWHMs of spinel phase (113) peak and its lattice parameter a obtained by Rietveld refinement.....	118
Figure 5.3	SEM images of co-doped ZnO based ceramics.....	119
Figure 5.4	Average grain sizes of co-doped ZnO based ceramics.....	120
Figure 5.5	Electrical conductivity of ZnO ceramic sampes.....	121
Figure 5.6	(a)The carrier concentration (n) and (b) carrier mobility (μ) of samples.....	121
Figure 5.7	Raman spectra of ZnO based ceramics.....	122
Figure 5.8	(a) EPR spectra of samples at room temperature, (b) and (c) EPR integrated intensity and linewidth, respectively, for different co-doped ZnO based ceramics.....	124
Figure 5.9	Qualitative plot of energy levels for defects involved in (Al, Ti) doped ZnO samples.....	125
Figure 5.10	EPR spectra line width versus the electrical conductivity in samples..	127
Figure 5.11	(a) ^{27}Al MAS NMR spectra of samples doped by Al_2O_3 (b) ^{67}Zn static NMR spectra of samples ZnO, ZnO:Mg, ZnO:Ti, ZnO:Al, ZnO:AlTi,	

	and ZnO:AlTiMg.....	129
Figure 6.1	(a) I-V curve and (b) Energy density vs. impulse current of as-synthesized ZnO ceramic.....	136
Figure 6.2	Size and size distribution of samples M and B.....	138
Figure 6.3	The schematic diagram of the crushed particles.....	138
Figure 6.4	(a) X-ray diffraction patterns, (b) FWHM of (101) peak for samples M and B.....	139
Figure 6.5	Raman spectra for samples M and B.....	140
Figure 6.6	(a) EPR spectra and thermal evolution of linewidth (ΔH)-(b) and integrated intensity (I_{EPR})-(c) for samples M and B.....	142
Figure 6.7	^{27}Al MAS NMR spectra of samples M and B.....	143
Figure 6.8	(a) Schematic diagram of substitutional Al^{3+} - interstitial Zn^{2+} ($\text{Al}_{\text{Zn}}\text{-Zn}_i$) in ZnO. (b) The KS effect evolution and the environment of $\text{Al}_{\text{Zn}}\text{-Zn}_i$ complex and Al_{Zn} , Zn_i for samples.....	144

List of Tables

Table 1.1	Basic properties of wurtzite ZnO.....	6
Table 1.2	Properties of metal resistor, carbon resistor and ZnO ceramic resistor..	25
Table 3.1	Atomic percentage of Ti in ZnO phase by EDS analysis.....	68
Table 3.2	Measured Raman modes in samples A, N and C and their assignment in doped ZnO based ceramics.....	72
Table 5.1	Initial composition of the investigated doped ZnO based ceramics.....	115